Phase-Field Modeling of Damage and Fracture in Fiber Reinforced Composites

Author: Aamir Dean
Supervisor: José Reinoso Cuevas

Mechanics of Continuous Media and Theory of Structures
School of Engineering
University of Seville

Seville, 2020

ÁMBITO- PREFIJO
GEISER
Nº registro
O00008744e2000024753

CSV
GEISER-aa34-5f08-a669-4b6e-9258-ed2f-d009-e7f3
DIRECCIÓN DE VALIDACIÓN

FECHA Y HORA DEL DOCUMENTO
19/06/2020 12:08:12 Horario peninsular

GEISER-aa34-5f08-a669-4b6e-9258-ed2f-d009-e7f3

PhD Thesis
Doctoral Program in Mechanical Engineering and Industrial Management

Phase-Field Modeling of Damage and Fracture in Fiber Reinforced Composites

Author:
Aamir Dean

Supervisor:
José Reinoso Cuevas
Assistant Professor

Mechanics of Continuous Media and Theory of Structures
School of Engineering
University of Seville

2020

ÁMBITO- PREFIJO
GEISER
Nº registro
O00008744e2000024753
CSV
GEISER-aa34-5f08-a669-4b6e-9258-ed2f-d009-e7f3
DIRECCIÓN DE VALIDACIÓN
FECHA Y HORA DEL DOCUMENTO
19/06/2020 12:08:12 Horario peninsular
GEISER-aa34-5f08-a669-4b6e-9258-ed2f-d009-e7f3

ÁMBITO- PREFIJO
GEISER
Nº registro
O00008744e2000024753
CSV
GEISER-aa34-5f08-a669-4b6e-9258-ed2f-d009-e7f3
DIRECCIÓN DE VALIDACIÓN
FECHA Y HORA DEL DOCUMENTO
19/06/2020 12:08:12 Horario peninsular
GEISER-aa34-5f08-a669-4b6e-9258-ed2f-d009-e7f3

To the martyrs of the glorious Sudanese revolution, the martyrs of the Darfur region, the martyrs of Kordofan, the martyrs of the South of the Sudan, the martyrs of the Manaseer region, martyrs of Gezira, and the martyrs of Port Sudan.

To the Sudanese refugee women and children who are still living in displacement camps.

To my beloved parents and family.

To my sister (with special needs) who dreams every night of one day getting into college.

To my unborn daughter, Maryam.

ÁMBITO- PREFIJO
GEISER
Nº registro
O00008744e2000024753
CSV
GEISER-aa34-5f08-a669-4b6e-9258-ed2f-d009-e7f3
DIRECCIÓN DE VALIDACIÓN
FECHA Y HORA DEL DOCUMENTO
19/06/2020 12:08:12 Horario peninsular
GEISER-aa34-5f08-a669-4b6e-9258-ed2f-d009-e7f3

Acknowledgements

A number of people have generously given time, advice, encouragement and valuable information during the course of this research.

I would like to express my gratitude to those who have made this thesis possible. Firstly, I would like to express my sincere and deepest gratitude to the thesis advisor José Reinoso for the continuous support of the Ph.D. study and related research, for his patience, motivation, and immense knowledge. His guidance helped me in all the time of research and writing of this thesis. I could not have imagined having a better adviser and mentor for this Ph.D. study. Thank you very much not only for the academic support but also on a personal level for helping me throughout one of the most difficult phases of my entire life.

My sincere thanks and gratitude also goes to Yaqin Nasreldin, Elsadig Mahdi, and Pavan Kumar. Without their precious support, it would not be possible to complete this thesis. Elsadig Mahdi and Pavan Kumar have always played a key role in encouraging and keeping me abreast of the scientific developments during the course of this Ph.D. study.

I would also like to thank my friends around the world for their ongoing support and enthusiasm. Thank you for your gentle inquiries as to progress, your encouragement, and your words of support as I made my way through the sometimes perilous territory of life.

Last but not least, I would like to give my special thanks to my family, especially to mom and dad, who have always stood by me like a pillar throughout my entire life and to whom I owe my life for their constant endless love, encouragement, moral support, and blessings; I could not have done anything without you.

Seville, June 18, 2020

Aamir Dean

ÁMBITO- PREFIJO
GEISER
Nº registro
O00008744e2000024753

CSV
GEISER-aa34-5f08-a669-4b6e-9258-ed2f-d009-e7f3
DIRECCIÓN DE VALIDACIÓN

FECHA Y HORA DEL DOCUMENTO
19/06/2020 12:08:12 Horario peninsular

GEISER-aa34-5f08-a669-4b6e-9258-ed2f-d009-e7f3

Resumen

Los procesos de fractura en materiales compuestos de matriz polimérica suelen ser significativamente diferentes con respecto a materiales tradicionalmente empleados en aplicaciones ingenieriles (metales y aleaciones metálicas, principalment) presentando características propias que los hacen notablemente complejos.

En este contexto, con referencia a las evidencias experimentales, existen varios tipos de mecanismos de fractura en estos materiales, los cuales pueden desarrollarse durante el tiempo de servicio de las estructuras correspondientes. Cada uno de estos mecanismos puede iniciarse y propagarse independientemente. Sin embargo, en la práctica, actúan sinérgicamente y pueden potencialmente aparecer de forma simultánea. Las dificultades para comprender y predecir cómo estos diferentes mecanismos de fractura pueden propagarse y coalescer, dando lugar al fallo estructural del componente, obligan el uso de factores de seguridad significativamente elevados, necesitando también un alto número de resultados experimentales para llevar a cabo las certificaciones requeridas por las autoridades competentes.

Teniendo en cuenta que las investigaciones experimentales relativas a los materiales compuestos de matriz de base polimérica pueden ser limitadas, muy costosas y dilatadas en el tiempo, el objetivo de esta investigación es desarrollar modelos fenomenológicos a nivel macroscópico para modelizar los procesos de fractura en estos materiales según la metodología denominada Phase-Field (PF). En primer lugar, se desarrolla un modelo de PF trasversalmente isótropo para la fractura dúctil de materiales compuestos poliméricos reforzados con fibras corta (SFRPs). Posteriormente, se propone un modelo de múltiples PF con el fin de capturar la fractura intra-laminar basado en la teoría de fallo de Puck para materiales compuestos poliméricos reforzados con fibra larga (LFRPs). En esta tesis se presentan la formulación teórica, el tratamiento algorítmico correspondiente y los detalles numéricos de implementación de los modelos propuestos. El rendimiento de los modelos se evalúa mediante un conjunto de simulaciones numéricas estándar que demuestran su aplicabilidad y robustez.

Además de los aspectos fundamentales de estos modelos propuestos, se analiza con especial profundidad el uso del modelo multi PF para la simulación numérica de la migración de delaminación en LFRP laminados. Para este propósito, se propone un procedimiento de modelado FE consistente que integra el modelo de campo de múltiples fases para fractura intra-laminar con un Modelo de Zona Cohesiva (CZM) para inter-laminar.

ÁMBITO- PREFIJO
GEISER
Nº registro
O00008744e2000024753
CSV
GEISER-aa34-5f08-a669-4b6e-9258-ed2f-d009-e7f3
DIRECCIÓN DE VALIDACIÓN
FECHA Y HORA DEL DOCUMENTO
19/06/2020 12:08:12 Horario peninsular
GEISER-aa34-5f08-a669-4b6e-9258-ed2f-d009-e7f3

ÁMBITO- PREFIJO
GEISER
Nº registro
O00008744e2000024753

CSV
GEISER-aa34-5f08-a669-4b6e-9258-ed2f-d009-e7f3
DIRECCIÓN DE VALIDACIÓN

FECHA Y HORA DEL DOCUMENTO
19/06/2020 12:08:12 Horario peninsular

GEISER-aa34-5f08-a669-4b6e-9258-ed2f-d009-e7f3

Abstract

The damage and fracture behavior of Fiber Reinforced Polymers (FRPs) is quite complex and is different than the failure behavior of the traditionally employed metals. There are various types of failure mechanisms that can develop during the service life of composite structures. Each of these mechanisms can initiate and propagate independently. However, in practice, they act synergistically and appear simultaneously. The difficulties that engineers face to understand and predict how these different failure mechanisms result in a structural failure enforce them to use high design safety factors and also increases the number of certification tests needed.

Considering that the experimental investigations of composites can be limited, very expensive, and time-consuming, it is the aim of this research to develop sophisticated phenomenological material models based on the Phase-Field (PF) approach to fracture for the virtual assessment of damage and fracture of FRPs. First, an anisotropic PF model for ductile fracture of Short Fiber Reinforced Polymers (SFRPs) is developed. Then, a multi PF model based on the Puck theory of failure is proposed for Long Fiber Reinforced Polymers (LFRPs). The theoretical formulation, corresponding algorithmic treatment, and numerical implementation details of the proposed models are presented. The performance of the models is assessed via a set of standard numerical simulations demonstrating their applicability and robustness.

Focusing on complex practical applications, the newly developed multi PF model is employed for the numerical simulation of delamination migration in laminated LFRPs. For this purpose, a consistent FE modeling procedure is proposed integrating the multi phase-field model for intra-laminar fracture with a Cohesive Zone Model (CZM) for inter-laminar.

ÁMBITO- PREFIJO
GEISER
Nº registro
O00008744e2000024753

CSV
GEISER-aa34-5f08-a669-4b6e-9258-ed2f-d009-e7f3
DIRECCIÓN DE VALIDACIÓN

FECHA Y HORA DEL DOCUMENTO
19/06/2020 12:08:12 Horario peninsular

GEISER-aa34-5f08-a669-4b6e-9258-ed2f-d009-e7f3

Declaration

I hereby declare that:

1. This work was done wholly or mainly while in candidature for a research degree at this University.
2. Where any part of this thesis has previously been submitted for a degree or any other qualification at this University or any other institution, this has been clearly stated.
3. Where I have consulted the published work of others, this is always clearly attributed.
4. Where I have quoted from the work of others, the source is always given. With the exception of such quotations, this thesis is entirely my own work.
5. I have acknowledged all main sources of help.
6. Where the thesis is based on work done by myself jointly with others, I have made clear exactly what was done by others and what I have contributed myself.

Seville, June 18, 2020

Aamir Dean

ÁMBITO- PREFIJO
GEISER
Nº registro
O00008744e2000024753
CSV
GEISER-aa34-5f08-a669-4b6e-9258-ed2f-d009-e7f3
DIRECCIÓN DE VALIDACIÓN
FECHA Y HORA DEL DOCUMENTO
19/06/2020 12:08:12 Horario peninsular
GEISER-aa34-5f08-a669-4b6e-9258-ed2f-d009-e7f3

Contents

Resumen V
Abstract VII

Declaration **IX**

1 Introduction **1**
- 1.1 Rationale and Motivation 1
- 1.2 Damage and Fracture of Fiber Reinforced Composites 2
  - 1.2.1 Short Fiber Reinforced Polymers 3
  - 1.2.2 Long Fiber Reinforced Polymers 4
- 1.3 Fundamentals of Continuum Solid Mechanics 4
  - 1.3.1 Kinematics 4
  - 1.3.2 Kinetics 5
  - 1.3.3 Boundary Conditions 5
  - 1.3.4 Constitutive Laws 6
  - 1.3.5 Boundary Value Problem 7
  - 1.3.6 Weak Form of the Boundary Value Problem 7
- 1.4 Computational Modeling of Damage and Fracture 8
  - 1.4.1 Discrete Modeling Approach 8
  - 1.4.2 Continuous Modeling Approach 9
- 1.5 Phase-Field Approach to Fracture 10
  - 1.5.1 Basic Principles of Fracture Mechanics 10
  - 1.5.2 Variational Formulation of the Phase-Field Approach 11
- 1.6 Objectives and Outlines 14

2 A Phase-Field Model for Ductile Fracture of Short Fiber Reinforced Polymers **18**
- 2.1 Introduction 19
- 2.2 Variational Formulation and Constitutive Modeling Approach for SFRPs 21
  - 2.2.1 Phase-Field Approach to Ductile Fracture: General Modeling Framework 21
  - 2.2.2 Constitutive Formulation for SFRPs: Invariant-Based Anisotropic Model 25
    - 2.2.2.1 Yield Function 26
    - 2.2.2.2 Plastic Potential Function 27

ÁMBITO- PREFIJO
GEISER
Nº registro
O00008744e2000024753

CSV
GEISER-aa34-5f08-a669-4b6e-9258-ed2f-d009-e7f3
DIRECCIÓN DE VALIDACIÓN

FECHA Y HORA DEL DOCUMENTO
19/06/2020 12:08:12 Horario peninsular

GEISER-aa34-5f08-a669-4b6e-9258-ed2f-d009-e7f3

2.2.2.3 Evolution Equations 27
2.2.2.4 Failure Criterion 27
2.2.2.5 Parameter Identification 28
2.3 Representative Applications 29
2.3.1 Material Parameters 29
2.3.2 Demonstrative Examples: Validation of Implementation 31
2.3.3 Dog-Bone Specimen 31
2.3.4 Single-Edge Notched Specimen 33
2.4 Concluding Remarks 34

3 A Multi Phase-Field Fracture Model for Long Fiber Reinforced Polymers 38
3.1 Introduction 39
3.2 Multi Phase-Field Formulation Based on the Puck Theory of Failure 40
3.2.1 Postulation of the Total Internal Energy Density 40
3.2.2 Phenomenological Failure Criterion: Fundamentals of the Puck Theory of Failure 44
3.2.3 Plasticity Formulation for Matrix-Dominated Response 46
3.3 Variational Formulation and Thermodynamics Aspects 48
3.4 Finite Element Implementation 50
3.5 Representative Applications 52
3.5.1 Material Parameters 52
3.5.2 Validation of Implementation 53
3.5.3 Demonstrative Examples 55
3.5.4 Open-Hole Tension Problem 56
3.6 Concluding Remarks 58

4 FE Modeling and Simulation of Delamination Migration in Multi-Layered Long Fiber Reinforced Polymers 62
4.1 Introduction 63
4.2 Multi Phase-Field-Cohesive Zone (MPF-CZ) Formulation Based on the Puck Theory of Failure 65
4.2.1 Bulk Energies 67
4.2.2 Interface Energies 68
4.2.3 Fundamentals of Puck Failure Criterion 69
4.3 Variational Formulation and Strong Forms 72
4.4 Finite Element Implementation 73
4.5 Representative Examples 75
4.5.1 Description of the Numerical Model: General Aspects 76
4.5.2 Numerical-Experimental Validation 77
4.5.3 Sensitivity Analysis: Role of Different Parameters 78
4.5.3.1 Effect of Position of Loading Application 78
4.5.3.2 Effect of the Variation of Ply Angle 78
4.5.3.3 Effect of the Variation of Initial Crack Length 80
4.6 Concluding Remarks 80

5 Summary and Outlook 83
5.1 Summary and conclusions 83

ÁMBITO- PREFIJO
GEISER
Nº registro
O00008744e2000024753

CSV
GEISER-aa34-5f08-a669-4b6e-9258-ed2f-d009-e7f3
DIRECCIÓN DE VALIDACIÓN

FECHA Y HORA DEL DOCUMENTO
19/06/2020 12:08:12 Horario peninsular

GEISER-aa34-5f08-a669-4b6e-9258-ed2f-d009-e7f3

5.2 Future developments 85

List of Figures 86
List of Tables 88
Bibliography 89

ÁMBITO- PREFIJO
GEISER
Nº registro
O00008744e2000024753

CSV
GEISER-aa34-5f08-a669-4b6e-9258-ed2f-d009-e7f3
DIRECCIÓN DE VALIDACIÓN

FECHA Y HORA DEL DOCUMENTO
19/06/2020 12:08:12 Horario peninsular

GEISER-aa34-5f08-a669-4b6e-9258-ed2f-d009-e7f3

1 Introduction

1.1 Rationale and Motivation

Modern industry demands the advent and development of materials and structures with improved environmentally-friendly capacities that allow reducing carbon footprint, and in conjunction with major safety performances with higher strengths and resistance to fatigue response, among many other attributes. The achievement of such conditions will contribute to the decrease in operational costs by virtue of the reduction of the required inspection and repair requirements during service conditions. Within this context, recent advances in composites materials, more specifically Fiber Reinforced Polymers (FRPs), are helping to replace traditional materials across a host of engineering applications because of their versatility, enhanced durability and resistance to fatigue and corrosion, high strength-to-weight ratio, and lower maintenance and life-cycle costs [1]. Nevertheless, the full load-bearing capacity ability of composites has not yet been completely exploited so far.

With the continuously evolving trend of shifting to composites materials, there exists a recurrent need for a better understanding of their complex anisotropic, inhomogeneous, and inelastic behavior. The extensive understanding of damage and fracture events in FRPs is a matter of significant importance in many practical applications, with a strong interest in the wind turbine, automotive, aerospace, and aeronautical industries. There are various types of damage and fracture mechanisms that can develop during the service life of loaded composites structures. Although each of these failure mechanisms can initiate and evolve independently, in practice they act synergistically and appear simultaneously. The complexity in understanding and predicting how the failure mechanisms lead to a structural failure enforces the use of high design safety factors and increases the number of required certification tests, see [2].

The fact that experimental investigations of composites can be limited, especially due to very high economical costs and time-consuming operations, has promoted the development of advanced and robust numerical modeling and simulation techniques to fully exploit the advantages of these materials under different loading conditions. The rapid growth of computational capacities motivates the development of a range of different sophisticated predictive models, which allow the simulation of a wide variety of complex engineering problems.

However, the conventional theories of local Continuum Mechanics (CM), which are extensively used to trigger stiffness deterioration in FRPs, suffer from notable pathologies in the corresponding numerical implementation schemes in conjunction with the fact that they present notable limitations for capturing well-known size effects. The alleviation of such drawbacks has been

ÁMBITO- PREFIJO
GEISER
Nº registro
O00008744e2000024753
CSV
GEISER-aa34-5f08-a669-4b6e-9258-ed2f-d009-e7f3
DIRECCIÓN DE VALIDACIÓN
FECHA Y HORA DEL DOCUMENTO
19/06/2020 12:08:12 Horario peninsular
GEISER-aa34-5f08-a669-4b6e-9258-ed2f-d009-e7f3

a matter of intensive research in the last two decades, as is the case of non-local Continuum Damage Mechanics (CDM) theories which inherently incorporate a characteristic length scale into the corresponding formulation, see [3–6].

Alternative routes for triggering fracture events are the strong discontinuity methodologies for fracture mechanics in solids, which incorporate an enriched kinematic description to model the material breakage upon loading, see [7–10]. Despite recent developments in these methodologies, the numerical modelling of complex fracture problems remains a challenging issue, particularly in three-dimensional applications [11].

In the last decades, a potential methodology that can overcome the fundamental limitations with respect to other methodologies aforementioned is the so-called Phase-Field (PF) method to fracture, see [12–15]. With strong roots in the energetic Griffith's vision of Fracture Mechanics (FM), PF methods endow the regularization of sharp crack discontinuities. However, this technique preserves the continuity of the displacement field, being especially suitable for triggering complex crack patterns.

Despite the relevant development of PF methods within the last decade, a careful revisitation of the State of the Art shreds of evidence that these numerical techniques have been developed for their application for a limited type of engineering materials, with major attention for brittle fracture. However, PF methods possess an enormous potential for the inclusion of phenomenological or physically-motivated failure criteria for brittle, quasi-brittle and ductile failure in a modular form, which can widen its range of application. Within this context, this research aims to develop sophisticated phenomenological material models based on the PF approach to fracture that can be employed into Finite Element Analysis (FEA) packages for virtual testing of damage and fracture in FRPs. A central aspect of this investigation is the development of a comprehensive theoretical and numerical study of PF methods for polymeric-based fiber reinforced composites, namely Short Fiber Reinforced Polymers (SFRPs) and Long Fiber Reinforced Polymers (LFRPs), within the infinitesimal deformation setting.

In the forthcoming sections, a brief overview of the damage and fracture morphology of SFRPs and LFRPs is presented. Furthermore, careful attention is devoted to the discussion of the different numerical techniques to model fracture events in such materials in conjunction with the overview of the fundamental concepts fracture mechanics and the phase-field approach to fracture.

1.2 Damage and Fracture of Fiber Reinforced Composites

Composites are made up of two or more materials (constituents) with different mechanical properties, which are combined to exhibit unique characteristics. Nowadays, in many practical applications in different engineering fields, composites are replacing materials that have been traditionally employed (namely metals and metal alloys) due to their enhanced properties such as low weight, high strength and stiffness, temperature, and corrosion resistance, etc. In most industrial applications, especially in aeronautical, automotive, and renewable energy sectors, Fiber Reinforced Polymers (FRPs) are being gradually incorporated [16]. Specifically, FRPs are composites made of fibers bound together by a polymer matrix and can be generally classified into two major categories: Short Fiber Reinforced Polymers (SFRPs) and Long (endless, continuous, or unidirectional) Fiber Reinforced Polymers (LFRPs) based on the length of the fibers used.

Numerous natural and engineered materials can be used as fibers to produce FRPs' parts and coupons. However, in most industrial applications, carbon, aramid (kevlar), or glass fibers are typically used. Based on the chemical structure and the degree of cross-linking between the macro-molecules, the matrix phase of FRPs is often divided into three main groups: thermosets, elastomers, and thermoplastics. Depending on the fiber/matrix combination, the specific material behavior is improved over the corresponding unreinforced matrix in terms of strength, hardness, stiffness, and thermal expansion. Generally, the resultant behavior is influenced by the individual materials and their adhesion, as well as by the employed manufacturing process. While the fibers principally withstand the external loading, the matrix plays many various roles in FRPs. For instance, it holds the fibers in the desired arrangement and keeps them at a distance. Thus, the matrix constituent also bonds the fibers one to another, and so transmits the forces to the individual fibers and between them. Furthermore, the matrix primarily withstands the loading actions when composites are loaded transversely with respect to the preferential fiber direction [17].

The comprehensive understanding of fracture events in FRPs is a matter of significant importance in many applications, with a strong interest in industries whereby the optimization of carrying loading capacity with significant weight savings is of central interest. However, under in-service conditions, cracking events generally lead to a drastic reduction of the load-bearing capacity of structural components and the posterior achievement of the corresponding collapsing point. In the following, the damage and fracture mechanisms of both, SFRPs and LFRPs, are briefly outlined.

1.2.1 Short Fiber Reinforced Polymers

In industrial applications, SFRPs parts are mostly manufactured employing the injection-molding process that allow high production rates to be achieved. Furthermore, this manufacturing technique permits the generation and fabrication of complex geometries with minimal post-molding operations [18]. However, such production processes usually result in a very complex fiber arrangement (orientation) over finished parts, which leads to a high degree of anisotropy and inhomogeneity.

In addition to the previous aspects, such anisotropic character has direct consequences on the corresponding mechanical performance. Thus, when SFRPs parts are subjected to static and cyclic loads, vibrations, and temperature variations according to their application, different damage and fracture mechanisms (modes) can develop. Generally, damage and fracture can be assessed in different scales i.e. micro-, meso-, and macro-scale [19]. However, in SFRPs, the corresponding failure mechanisms are usually studied in the micro-scale where the material constituents (fiber, matrix, and fiber/matrix interface) are considered as different phases, accounting for the combined interaction between such phases [20]. At this scale, four main mechanisms are primarily observed, which correspond to: (i) matrix fracture, (ii) fiber breakage, (iii) fiber pullout, and (iv) fiber/matrix interface debonding, see Figure 1.1a. Due to the difference of the micro-structure, each failure mechanism tends to initiate and propagate for a particular state of loading [20].

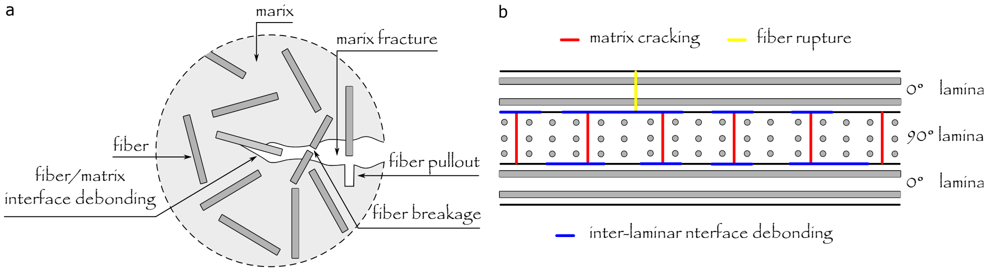

Figure 1.1 Damage and fracture mechanisms in loaded FRPs: (a) failure mechanisms in SFRPs at micro-scale and (b) failure mechanisms in LFRPs meso-scale.

ÁMBITO- PREFIJO
GEISER
Nº registro
O00008744e2000024753
CSV
GEISER-aa34-5f08-a669-4b6e-9258-ed2f-d009-e7f3
DIRECCIÓN DE VALIDACIÓN
FECHA Y HORA DEL DOCUMENTO
19/06/2020 12:08:12 Horario peninsular
GEISER-aa34-5f08-a669-4b6e-9258-ed2f-d009-e7f3

1.2.2 Long Fiber Reinforced Polymers

The second family of fiber reinforced composites under consideration in the present research corresponds to LFRPs. In these materials, the length-to-diameter ratio is very high in comparison to that corresponding to SFRPs. The basic structural element of parts made from LFRPs is denominated as lamina (ply), whereby one geometric dimension (out-of-plane, i.e the lamina thickness) is significantly smaller in comparison to the in-plane dimensions. The lamina may consist of unidirectional fiber alignment which has the highest strength and stiffness parallel to the fiber direction. Hence, the fiber orientation plays a crucial role in the mechanical response of LFRPs. The so-called lamination process is usually employed to produce LFRPs parts (laminates) in the desired stacking sequence. Nevertheless, this process results in inter-laminar (between the laminas) regions known as interfaces that correspond to the weaker areas in the resulting laminates, especially in bending-dominated applications. Hence, the failure of LFRPs laminates can take place either in the inter-laminar or intra-laminar (within the laminas) region, leading to the differentiation between the corresponding failure mechanisms.

From a modeling perspective, the assessment of damage and fracture in LFRPs can also be carried out at different scales. However, failure mechanisms in LFRPs are generally studied in the meso-scale, with the specific differentiation between the laminas disposals and accounting for the laminate constituents (lamina and interface) and the corresponding interaction [21]. At the meso-cale, relying on experimental evidence, four main mechanisms are identified: (i) matrix cracking, (ii) fiber rupture, (ii) fiber kinking, and (iv) inter-laminar interface debonding, see Figure 1.1b. Similarly, crack initiation and propagation associated with each of the failure mechanism depends strongly on the loading condition [19, 21]. In practice, the failure mechanisms act synergistically and appear simultaneously at different locations of the loaded structures.

1.3 Fundamentals of Continuum Solid Mechanics

This section brifely regards the fundamental aspects of Continuum Solid Mechanics (CSM) that set the foundation of the computational problem under consideration based on the lecture notes by Meschke [22]. Note that, for the sake of brevity, the formulation presented subsequently is restricted to infinitesimal deformation, quasi-static, elasto-mechanics analysis, though the consistent extension to the omitted applications can be conducted.

1.3.1 Kinematics

Consider an arbitrary body whose domain is denoted by $\mathscr{B} \in \mathbb{R}^{n_{\text{dim}}}$ ($n_{\text{dim}} = 1,2,3$ is the number of spatial dimensions). The delimiting boundary of $\mathscr{B}$ is identified by $\partial\mathscr{B} \in \mathbb{R}^{n_{\text{dim}}-1}$. Continuum kinematics describes the motion of the body $\mathscr{B}$ and its deformation during the motion. The reference placement of the arbitrary body $\mathscr{B}$ is completely defined by the position vector of material points $\mathbf{X}$ and its change of position at deformation under arbitrary internal or external influence. This motion of the material points from the undeformed to the deformed state is described by means of the displacement vector $\mathbf{u}$ as a function of the position of the material point. The current position of the material point under consideration at time t is given by the position vector:

$$\mathbf{x}(\mathbf{X},t) = \mathbf{X} + \mathbf{u}(\mathbf{X},t)\,. \tag{1.1}$$

The Lagrangian approach is to be observed clearly here in the context of the dependence of the current position on the initial position and on time t. Note that, in the quasi-static case, time is transformed into pseudo-time, which only serves to characterize the state of deformation.

The infinitesimal strain measure $\boldsymbol{\varepsilon}$ is defined by the symmetric part of the displacement gradient $\nabla^{\mathrm{sym}}\mathbf{u}$ as follows:

$$\boldsymbol{\varepsilon} := \nabla^{\mathrm{sym}}\mathbf{u} = \frac{1}{2}\left[\nabla\mathbf{u} + \nabla^{T}\mathbf{u}\right]. \tag{1.2}$$

1.3.2 Kinetics

Kinetics describes the relation between external and internal forces acting on a material body. According to the stress principle of Cauchy, in the current configuration, a symmetric second-order tensor $\boldsymbol{\sigma}$ of stresses exists in any material point as a consequence of the external forces. Together with the static loads acting throughout the volume, these stresses form the local balance of momentum or the equilibrium of forces. The balance of momentum must be satisfied throughout the deformed configuration.

Cauchy's theorem is based upon the postulate of a stress vector $\mathbf{t}$ on an arbitrary cross-section of a material body. The Cauchy's stress theorem postulates the linear dependency between Cauchy traction vector $\mathbf{t}$ and the normal of the surface $\mathbf{n}$ (which the traction vector acting on) through the symmetric Cauchy (true) stress tensor:

$$\mathbf{t} = \boldsymbol{\sigma} \cdot \mathbf{n}. \tag{1.3}$$

The balance equation of the linear momentum describes the equilibrium of the internal forces and the stresses. The local balance of momentum can be derived in accordance with continuum mechanics, based on the integral balance of momentum and under consideration of Cauchy's theorem, quasi-static analysis assumption (by neglecting transient effects), and some mathematical simplifications as follows:

$$\mathrm{div}\boldsymbol{\sigma} + \mathbf{f}_v = \mathbf{0}, \tag{1.4}$$

where $\mathrm{div}[\bullet]$ is the divergence operator and $\mathbf{f}_v$ denotes the deformation-independent, volume-specific loads.

1.3.3 Boundary Conditions

The basic equations of kinematics and kinetics derived in the previous sections are valid inside $\mathscr{B}$ at an arbitrary point in time t. This system of equations has to be supplemented with boundary conditions concerning the characteristic kinematic and kinetic size of the body's surface or the domain boundary $\partial\mathscr{B}$.

The domain's boundary $\partial\mathscr{B}$ is divided into the non-overlapping Dirichlet boundary $\partial\mathscr{B}_u$ and Neumann boundary $\partial\mathscr{B}_t$:

$$\overline{\partial\mathscr{B}_t \cup \partial\mathscr{B}_u} = \partial\mathscr{B} \text{ and } \partial\mathscr{B}_u \cap \partial\mathscr{B}_t = \emptyset. \tag{1.5}$$

Here, as a rule, the primary variable is prescribed on the Dirichlet boundary and dependent quantities are prescribed on the Neumann boundary. In the context of elasto-mechanics, these are the displacements $\mathbf{u}$ and the stress vector $\mathbf{t}$, respectively.

Continuum kinematics is supplemented by the essential, geometrical or Dirichlet boundary conditions. Dirichlet boundary conditions are prescribed displacements at a given time

$$\mathbf{u}(\mathbf{X},t) = \bar{\mathbf{u}}(\mathbf{X},t)\ \forall\mathbf{X} \in \partial\mathscr{B}_u. \tag{1.6}$$

ÁMBITO- PREFIJO
GEISER
Nº registro
O00008744e2000024753
CSV
GEISER-aa34-5f08-a669-4b6e-9258-ed2f-d009-e7f3
DIRECCIÓN DE VALIDACIÓN
FECHA Y HORA DEL DOCUMENTO
19/06/2020 12:08:12 Horario peninsular
GEISER-aa34-5f08-a669-4b6e-9258-ed2f-d009-e7f3

The static, natural or Neumann boundary conditions can be written in a compact form in tensorial notation in the form of the Cauchy equation:

$$\boldsymbol{\sigma}(\mathbf{X},t)\cdot\mathbf{n}=\bar{\mathbf{t}}(\mathbf{X},t)\ \forall\mathbf{X}\in\partial\mathscr{B}_t. \tag{1.7}$$

1.3.4 Constitutive Laws

In the previous sections, stresses and strains were defined based on the momentum balance and the displacement field, respectively. Hence, both the stress tensor and the displacement vector are variables which are needed for the unambiguous description of the continuum's state of motion. This number of variables can be reduced by the postulate of a constitutive relationship which relates the stresses on the one hand, and the strains on the other. As a consequence of this postulate, the stresses become dependent on the displacement vector.

A generalized material law contains a number of material models for the description of nonlinear material behavior, taking into account micro-structural damage, residual plastic strains, and time-dependent effects. If, however, the attention is focused on the modeling of reversible, time-independent, elastic processes, the stress state can be defined only based on the strain state, with the stress tensor turning into a null tensor in the undeformed configuration:

$$\boldsymbol{\sigma}=\boldsymbol{\sigma}(\boldsymbol{\varepsilon}). \tag{1.8}$$

the fundamental concept of the Theory of Elasticity means that the stress state only depends on the instantaneous strain state and not on the stress path. The desired path-independence is only guaranteed, if the stress tensor can be derived by differentiation of an elastic scalar-valued potential function $W(\boldsymbol{\varepsilon})$ with respect to the strain tensor:

$$\boldsymbol{\sigma}:=\frac{\partial W(\boldsymbol{\varepsilon})}{\partial\boldsymbol{\varepsilon}}. \tag{1.9}$$

Consequently, if the deformation is independent of the path, the corresponding material laws can be denominated as hyper-elastic (where the so-called Kirchhoff-Saint-Venant material model that is characterized by the linear relation $\boldsymbol{\sigma}-\boldsymbol{\varepsilon}$ is a particular case). The consistent derivation of the stress tensor with respect to the strain tensor yields the tangential modulus of elasticity, constitutive tensor or material tensor $\mathbb{C}$. On the other hand, the material tensor represents the linear mapping of the strain tensor onto the stress tensor:

$$\mathbb{C}:=\frac{\partial\boldsymbol{\sigma}(\boldsymbol{\varepsilon})}{\partial\boldsymbol{\varepsilon}}=\frac{\partial W(\boldsymbol{\varepsilon})}{\partial\boldsymbol{\varepsilon}\otimes\partial\boldsymbol{\varepsilon}}\text{ and }\boldsymbol{\sigma}=\mathbb{C}:\boldsymbol{\varepsilon}. \tag{1.10}$$

As a consequence of the symmetry of the stress and strain tensors, the fourth-order constitutive tensor is symmetric.

Recalling the previous discussion, a material model relying on the assumption stating that the material tensor $\mathbb{C}$ is independent of the strains, a linear relationship can be postulated between stresses and strains and leading to a standard linear elastic constitutive law. All other material models are characterized correspondingly by the attributes physically or material non-linear.

Note that, in order to establish physically acceptable constitutive models, there exist several universal principles (based on physical observation) to be satisfied. Some of the most important principles are the principle of determinism, material frame indifference (objectivity), consistency (thermodynamics considerations), material symmetry, and causality. These principles enforce restrictions on constitutive models and therefore simplify and specify general constitutive relations. There exist in literature numerous inequalities for constitutive models been proposed in order to assure physically reasonable material behavior, e.g. Becker-Erickson inequality, Coleman-Noll inequality, among many others [23].

1.3.5 Boundary Value Problem

The summary of the fundamental equations of continuum, presented in the previous sections, forms the Boundary Value Problem (BVP) of quasi-static elasto-mechanics. In detail, these are the description of deformation in the context of kinematics, the formulation of the force equilibrium based on kinetic considerations, the constitutive equation as well as the boundary conditions.

The essential components of the description of small, linear elastic deformations make for the formulation of the relationship between displacement and strain field, the equilibrium of forces and the constitutive equation relating the stresses and strains. All three components together form the second-order partial differential equation of linear elasto-mechanics with the displacement field as the solution variable:

$$\boldsymbol{\varepsilon} = \nabla^{\text{sym}}\mathbf{u},\ \mathbf{0} = \text{div}\boldsymbol{\sigma} + \mathbf{f}_v,\ \text{and}\ \boldsymbol{\sigma} = \mathbb{C} : \boldsymbol{\varepsilon}. \tag{1.11}$$

Hence, the resulting differential equation is given by:

$$\mathbf{0} = \text{div}\left(\mathbb{C} : \nabla^{\text{sym}}\mathbf{u}\right) + \mathbf{f}_v. \tag{1.12}$$

For the solution of the above governing differential equation, the Dirichlet and Neumann boundary conditions should to be added.

1.3.6 Weak Form of the Boundary Value Problem

The local behavior of the elastic body $\mathscr{B}$ was fully described in the previous sections by means of the boundary value problem. In most cases, the solution of this governing differential equation is not possible to be determined analytically. Therefore, approximation methods, in particular, the Finite Element Method (FEM), are used in order to find an approximate solution (that can be plausible from an engineering standpoint due to the corresponding accuracy with well-known benchmark problems). This method actually does not solve the so-called strong form of the partial differential equation. It merely solves its integral over the domain, the so-called weak (relaxed) form of the governing differential equation. This weak formulation forms the basic prerequisite for the application of FEM.

Integral principles of mechanics are; the principle of virtual displacements or principle of virtual work, the principle of virtual forces, and the principle of the minimum of total potential or its generalization for transient considerations, the Hamilton's principle of a continuum.

For the generation of the principle of the minimum of total potential, an energy functional $\Pi(\mathbf{u})$ governing the conservation of linear momentum is formulated:

$$\Pi(\mathbf{u}) = \Pi_{\text{int}}(\mathbf{u}) + \Pi_{\text{ext}}(\mathbf{u}), \tag{1.13}$$

where $\Pi_{\text{int}}(\mathbf{u})$ and $\Pi_{\text{ext}}(\mathbf{u})$ denote the internal and external contributions to the total energy which are defined respectively as:

$$\Pi_{\text{int}}(\mathbf{u}) = \int_{\mathscr{B}} W(\boldsymbol{\varepsilon}(\mathbf{u}))\text{d}\Omega, \tag{1.14}$$

$$\Pi_{\text{ext}}(\mathbf{u}) = -\int_{\mathscr{B}} \mathbf{u} \cdot \mathbf{f}_v \text{d}\Omega - \int_{\partial\mathscr{B}_t} \mathbf{u} \cdot \bar{\mathbf{t}}\partial\text{d}\Omega. \tag{1.15}$$

ÁMBITO- PREFIJO
GEISER
Nº registro
O00008744e2000024753

CSV
GEISER-aa34-5f08-a669-4b6e-9258-ed2f-d009-e7f3
DIRECCIÓN DE VALIDACIÓN

FECHA Y HORA DEL DOCUMENTO
19/06/2020 12:08:12 Horario peninsular

GEISER-aa34-5f08-a669-4b6e-9258-ed2f-d009-e7f3

Following the standard Bubnov-Galerkin method of weighted residual, the trial solution of the unknown filed **u** with $\mathscr{U}_u = \left\{ \mathbf{u} \in H^1(\mathscr{B}) | \nabla \mathbf{u} \in L^2(\mathscr{B});\ \mathbf{u} = \bar{\mathbf{u}} \text{ on } \partial\mathscr{B}_u \right\}$, is introduced with the corresponding test functions $\delta\mathbf{u}$ with $\mathscr{V}_u = \left\{ \delta\mathbf{u} \in H^1(\mathscr{B}) | \nabla \delta\mathbf{u} \in L^2(\mathscr{B});\ \delta\mathbf{u} = \mathbf{0} \text{ on } \partial\mathscr{B}_u \right\}$, where H^1 denotes the Sobolev space. There accordingly:

$$\delta\Pi(\mathbf{u},\delta\mathbf{u}) = \delta\Pi_{\text{int}}(\mathbf{u},\delta\mathbf{u}) + \delta\Pi_{\text{ext}}(\mathbf{u},\delta\mathbf{u}), \tag{1.16}$$

with:

$$\delta\Pi_{\text{int}}(\mathbf{u},\delta\mathbf{u}) = \int_{\mathscr{B}} \frac{\partial W(\boldsymbol{\varepsilon}(\mathbf{u}))}{\partial \boldsymbol{\varepsilon}} : \boldsymbol{\varepsilon}(\delta\mathbf{u})\mathrm{d}\Omega = \int_{\mathscr{B}} \boldsymbol{\sigma} : \boldsymbol{\varepsilon}(\delta\mathbf{u})\mathrm{d}\Omega, \tag{1.17}$$

$$\delta\Pi_{\text{ext}}(\mathbf{u},\delta\mathbf{u}) = -\int_{\mathscr{B}} \delta\mathbf{u} \cdot \mathbf{f}_v \mathrm{d}\Omega - \int_{\partial\mathscr{B}_t} \delta\mathbf{u} \cdot \bar{\mathbf{t}} \mathrm{d}\partial\Omega, \tag{1.18}$$

The weak form of the quasi-static elasto-mechanics problem regarding the conservation of linear momentum consists of finding the displacement field $\mathbf{u} \in \mathscr{U}_u$ at each time (pseudo-time) t such that for all $\delta\mathbf{u} \in \mathscr{V}$:

$$\delta\Pi(\mathbf{u},\delta\mathbf{u}) = 0, \tag{1.19}$$

subjected to the prescribed traction $\bar{\mathbf{t}}$ on $\partial\mathscr{B}_t$.

The weak form of the aforementioned equations can be subsequently discretized using FEM in which the infinite-dimensional function spaces $\mathscr{U}_u$ and $\mathscr{V}_u$ are approximated by finite-dimensional subspaces $\mathscr{U}_u^h$ and $\mathscr{V}_u^h$, respectively, imposing the same conditions on the boundaries.

1.4 Computational Modeling of Damage and Fracture

The complexity of potential failure mechanisms from different signatures in fiber reinforced composites has promoted the development of a range of different numerical predictive models, especially within the context of FEM due to its versatility and potential for its application at different scales of observation. In the subsequent section, a brief outline of the most popular methods for tracking failure and fracture events in solids is presented.

It is worth mentioning that despite the wide variety of computational methods to fracture, in the current investigation, these models are arranged into two major groups based on the qualitative modeling of the cracking processes, i.e. discrete and continuous models.

1.4.1 Discrete Modeling Approach

The first group of computational models for triggering fracture herewith discussed is the so-called discrete modeling approach to fracture. This computational methodology has a direct connection with the evidence in the sense that it accounts for a discontinuous displacement field as a representation of the fracture process. Following this vision, the displacement field (and also the strain field) is discontinuous across the fracture surfaces causing a displacement jump [11].

The most notable theories behind the discrete approach recall the Linear Elastic Fracture Mechanics (LEFM) and Cohesive Zone Model (CZM) [11,24–26]. However, both methodologies present notable limitations. On the one hand, LEFM-based methods require the existence of an initial crack due to its inability for capturing crack nucleations processes and the need for additional criteria to provide information about crack initiation, propagation, and path. Moreover, LEFM presents a notable inaccuracy for very short cracks, which requires the use of alternative

ÁMBITO- PREFIJO
GEISER
Nº registro
O00008744e2000024753
CSV
GEISER-aa34-5f08-a669-4b6e-9258-ed2f-d009-e7f3
DIRECCIÓN DE VALIDACIÓN
FECHA Y HORA DEL DOCUMENTO
19/06/2020 12:08:12 Horario peninsular
GEISER-aa34-5f08-a669-4b6e-9258-ed2f-d009-e7f3

methods such that denominated Coupled Criteria (CC) or Finite Fracture Mechanics (FFM), see [27, 28].

With respect to CZMs, which implicitly accounts for the so-called fracture process zone (FPZ) concept, these methods allow the accurate modeling of very short and large cracks evolutions due to the inherent account for the energetic and stress-based criteria. Nevertheless, cohesive methods usually need either remeshing techniques for the insertion of interface-like elements or the introduction of such elements prior to running the simulation, limiting the corresponding crack paths to the edges of the elements. Examples of both techniques are Interface Element Methods (IEM), and eXtended Finite Element Method (XFEM), among many others. The last methodology resolves the discontinuities at the intra-element level while the first two act at the inter-element level, see [7, 11, 29].

1.4.2 Continuous Modeling Approach

An alternative modeling approach to fracture events in solids is the co-called Continuous Modeling Approach (CDM) where the discontinuous character of the displacement field is smeared over a certain region within the domain. Hence, the stresses are gradually degraded in order to model the fracture process. The most well-known theory behind the continuous approach is the so-called Continuum Damage Mechanics (CDM) [30]. Classical fracture mechanics is inappropriate to predict crack-initiation while crack-propagation can only be described when the crack-path is known beforehand. Continuum damage mechanics offers principally more extended possibilities for crack analyses.

In CDM, nucleation and propagation of cracks are modeled phenomenologically by making assumptions about their morphology and how it influences the material properties. For example, the understanding of the progressive degradation of the material before rupture as the loss of active area due to the nucleation of micro-cracks across the Fracture Process Zone (FPZ). According to CDM, the material deterioration process (damage) is governed by the thermodynamics state of the material through a set of internal state variables, the so-called damage variables, see [31]. This allows modeling fracture through the stress-strain law, and as mentioned above, leading to a smeared representation of cracks.

The employment of the classical CDM theory to model strain-softening in its local version (i.e. at the integration point level within the corresponding Fe formulation) suffers from pathological mesh dependence due to the lack of internal length scale in the formulation. For example, the energy dissipated when employing a numerical model based on the classical CDM theory decreases after mesh refinement and tends to extremely low values [11]. Mathematically, the mesh dependency is attributed to the loss of positive definiteness of the so-called material acoustic tensor. Hence, the governing differential equations lose ellipticity and become ill-posed at the onset of strain localization, as a consequence of material instability. This fact motivated the development of regularisation theories (based on generalized continuum theories) that incorporate a characteristic length scale to enforce a certain minimum width of the numerically resolved Process Zone (PZ) and prevent localization of strain into an arbitrarily small volume. An example of such regularisation theories is the non-local continuum damage theory. In a broad sense, most of the non-local damage models are classified into groups of differential and integral types. In contrast to the classical CDM theory, in the non-local formulations, the material damage process is not only governed by the thermodynamics state of the associated material point but also the state of the surrounding points [32]. The differential type incorporates spatial gradients of the internal state variables to consider the interaction between the material points of the body, while the integral type regards the interaction through weighted spatial averages of the state variables [33].

ÁMBITO- PREFIJO
GEISER
Nº registro
O00008744e2000024753
CSV
GEISER-aa34-5f08-a669-4b6e-9258-ed2f-d009-e7f3
DIRECCIÓN DE VALIDACIÓN
FECHA Y HORA DEL DOCUMENTO
19/06/2020 12:08:12 Horario peninsular
GEISER-aa34-5f08-a669-4b6e-9258-ed2f-d009-e7f3

As was previously introduced in the present document, in the last years, a new class of non-local continuum damage models has been established in literature known as a phase-field approach to fracture. The phase-field approach is mightily associated with the variational approach to fracture in which the sharp crack topology is regularized by a diffusive crack representation within a region band [13, 34]. Similarly, the phase-field formulation incorporates a length scale parameter associated with the width of the localization band. In contrast to the discrete crack modeling approaches, in the phase-field approach, the crack paths are automatically determined as part of the solution due to the account for the evolution equation of the phase-field crack variable as the primary unknown of the corresponding system. Since the PF method is the central numerical method to fracture developed in this thesis, in Section 1.5, the fundamental aspects of the variational formulation of this numerical methodology are briefly revisited.

1.5 Phase-Field Approach to Fracture

This section concerns the fundamental aspects of the phase-field approach to fracture. At first, the fundamentals of fracture mechanics are briefly introduced, then the variational formalism of the phase-field approach to fracture is presented. Note that, for conciseness reasons and in line with previous derivations, the formulation presented subsequently is restricted to infinitesimal deformation analysis, quasi-static, brittle fracture, though the consistent extension to the omitted applications can be conducted following the variational forms proposed in [35–40].

1.5.1 Basic Principles of Fracture Mechanics

Fracture Mechanics (FM) basically deals with the mechanics of solids that involve cracks and their initiation and propagation. Consider an arbitrary body whose domain is denoted by $\mathscr{B} \in \mathbb{R}^{n_{\text{dim}}}$ ($n_{\text{dim}} = 1,2,3$ is the number of spatial dimensions). From the macroscopic perspective, a crack in a three-dimensional body $\mathscr{B} \in \mathbb{R}^3$ is viewed as a cut through the body yielding two opposite surfaces, called crack surfaces that intersect in the crack front. However, in a two-dimensional body $\mathscr{B} \in \mathbb{R}^2$, a crack results in two opposite crack edges that meet in the so-called crack tip.

Depending on the relative displacement between the crack surfaces, the crack opening can be classified as: (i) Mode-I, (ii) Mode-II, and (iii) Mode-III fracture, see Figure 1.2. In general, each crack in the body can be described as the superposition of the three different fracture modes.

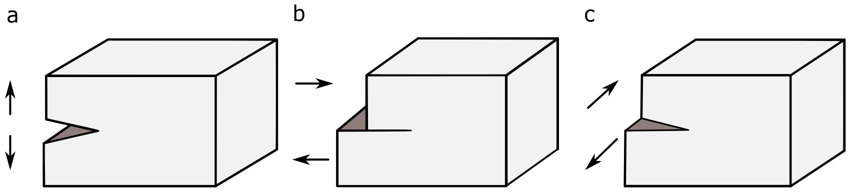

Figure 1.2 Fracture modes: (a) Mode-I (opening mode), (b) Mode-II (shearing mode), and Mode-III (tearing mode).

In linear elastic fracture mechanics (LEFM), the crack mechanism is determined by the singular stress field with intensity K_I in the vicinity of the crack front. Hence, the crack starts to propagate when the stress intensity factor K_I induced by corresponding external loading, reaches the material resistance against crack evolution which is characterized by the so-called fracture toughness K_{Ic}, see [15, 25].

Recalling alternative concepts, Griffith proposed the concept of the energy release rate for brittle fracture [24]. Following the first principle of the thermodynamics and considering an

ÁMBITO- PREFIJO
GEISER
Nº registro
O00008744e2000024753
CSV
GEISER-aa34-5f08-a669-4b6e-9258-ed2f-d009-e7f3
DIRECCIÓN DE VALIDACIÓN
FECHA Y HORA DEL DOCUMENTO
19/06/2020 12:08:12 Horario peninsular
GEISER-aa34-5f08-a669-4b6e-9258-ed2f-d009-e7f3

isothermal, quasi-static problem of a body subjected to external mechanical loading, the rate of change of total energy is equal to the mechanical power $\mathscr{P}$:

$$\dot{\mathscr{E}} + \dot{\mathscr{D}} = \mathscr{P}, \tag{1.20}$$

where $\mathscr{E}$ denotes the internal energy and $\mathscr{D}$ is the energy dissipated in the crack formation which is related to the crack surface $\mathfrak{A}$ and the material parameter ς as:

$$\mathscr{D} = 2\varsigma\mathfrak{A}. \tag{1.21}$$

Assuming a body with elastic material behavior subjected to external mechanical conservative loads, Eq.(1.20) can be written as:

$$\dot{\Pi}_{\text{int}} + \dot{\mathscr{D}} = -\dot{\Pi}_{\text{ext}}, \tag{1.22}$$

where Π_{int} and Π_{ext} denote the internal and external potential, respectively.

For a crack growth $\Delta\mathfrak{A}$ between an initial crack $\mathfrak{A}_i$ at t_i and the propagated crack $\mathfrak{A}_{i+1}$ at t_{i+1} Eq.(1.22) yields:

$$-\frac{\Delta\Pi}{\Delta\mathfrak{A}} = 2\varsigma, \tag{1.23}$$

where the left-hand side of the equation represents the so-called energy release rate $\mathscr{G}$ which describes the availability of energy for crack formation and the right-hand side refers to the energy required for the crack growth $\Delta\mathfrak{A}$ which is known as the critical energy release rate $\mathscr{G}_c$. There accordingly, in a conservative system, the crack propagates when the energy release rate $\mathscr{G}$ reaches the critical value $\mathscr{G}_c$. The critical rate is considered to be a material property and in contrast to the aforementioned stress intensity factor, it is independent of the body geometry.

1.5.2 Variational Formulation of the Phase-Field Approach

This section concerns the fundamental aspects of the variational formalism of the phase-field approach to fracture.

For the application of the PF method within a multi-dimensional framework, let to consider an arbitrary body whose domain is denoted by $\mathscr{B} \in \mathbb{R}^{n_{\text{dim}}}$ ($n_{\text{dim}} = 1,2,3$ is the number of spatial dimensions). The delimiting boundary of $\mathscr{B}$ is identified by $\partial\mathscr{B} \in \mathbb{R}^{n_{\text{dim}}-1}$.

In line with previous concepts, throughout the deformation process, the body is kinematically identified by the displacement field vector $\mathbf{u} : \mathscr{B} \to \mathbb{R}^{n_{\text{dim}}}$ and the infinitesimal strain field tensor defined as $\boldsymbol{\varepsilon} := \nabla^{\text{sym}}\mathbf{u}$ with $\boldsymbol{\varepsilon} : \mathscr{B} \to \mathbb{R}^{n_{\text{dim}} \times n_{\text{dim}}}$. Prescribed displacement conditions are given by $\mathbf{u} = \bar{\mathbf{u}}$ on $\partial\mathscr{B}_u$, whereas prescribed tractions conditions on the corresponding portion of the boundary are denoted as $\bar{\mathbf{t}} = \boldsymbol{\sigma} \cdot \mathbf{n}$ on $\partial\mathscr{B}_t$ with $\boldsymbol{\sigma}$ identifying the Cauchy stress tensor and $\mathbf{n}$ the external outer normal vector to the body. Kinematic and static boundary conditions satisfy the standard requirements: $\overline{\partial\mathscr{B}_t \cup \partial\mathscr{B}_u} = \partial\mathscr{B}$ and $\partial\mathscr{B}_t \cap \partial\mathscr{B}_u = \emptyset$.

The key concept for the phase-field approach to fracture comprises the regularization of a sharp crack topology Γ_c by a diffusive crack within a diffusive crack zone of width l, Figure 1.3. This approximation is based on the definition of the so-called crack phase-field variable $\mathfrak{d} : \mathscr{B} \times [0,t] \to [0,1]$, which is a smooth function within the domain, characterizing for $\mathfrak{d} = 0$ and $\mathfrak{d} = 1$ the intact and the cracked states, respectively. This variable is defined within the body under consideration $\mathscr{B}$ and its evolution is ruled by a suitable temporal expression within the time

ÁMBITO- PREFIJO
GEISER
Nº registro
O00008744e2000024753
CSV
GEISER-aa34-5f08-a669-4b6e-9258-ed2f-d009-e7f3
DIRECCIÓN DE VALIDACIÓN
FECHA Y HORA DEL DOCUMENTO
19/06/2020 12:08:12 Horario peninsular
GEISER-aa34-5f08-a669-4b6e-9258-ed2f-d009-e7f3

interval $[0,t]$ along the deformation process. Based on this and recalling mathematical arguments in the spirit of the Γ-convergence concept [41], the fracture energy can be approximated by:

$$\int_{\Gamma_c} \mathscr{G}_c \mathrm{d}\Gamma_c \approx \int_{\mathscr{B}} \mathscr{G}_c \gamma(\mathfrak{d}, \nabla\mathfrak{d}) \mathrm{d}\Omega, \tag{1.24}$$

where $\mathscr{G}_c$ is the bulk critical energy release rate and $\gamma(\mathfrak{d}, \nabla\mathfrak{d})$ is the so-called crack surface density functional.

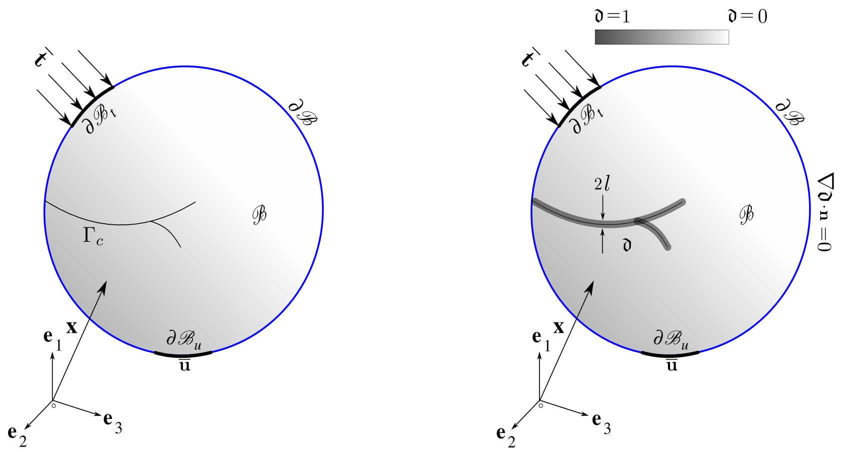

Figure 1.3 Phase-field method for diffusive crack modelling in solids: (a) sharp crack representation and (b) regularized crack topology.

Different authors assumed the quadratic form of the crack surface density functional, which has been successfully applied to isotropic materials [41–43]:

$$\gamma(\mathfrak{d}, \nabla\mathfrak{d}) = \frac{1}{2l}\mathfrak{d}^2 + \frac{l}{2}|\nabla\mathfrak{d}|^2. \tag{1.25}$$

Note, that the expression above is also governed by the length scale parameter l which can be related to the apparent material strength [44]:

$$l = \frac{27}{256}\frac{E\mathscr{G}_c}{\sigma_s^2}, \tag{1.26}$$

where E denotes the Young modulus and σ_s is the material strength.

In a general form, according to [45,46], the phase-field method of fracture can resemble a class of gradient-damage approach. This allows the postulation of the *total pseudo-energy density* W per unit volume for solids:

$$W(\boldsymbol{\varepsilon}, \mathfrak{d}, \nabla\mathfrak{d}) = \Psi(\boldsymbol{\varepsilon}, \mathfrak{d}) + W_{\text{frac}}(\mathfrak{d}, \nabla\mathfrak{d}), \tag{1.27}$$

where $\Psi(\boldsymbol{\varepsilon}, \mathfrak{d})$ is the bulk free-energy per unit volume and $W_{\text{frac}}(\mathfrak{d}, \nabla\mathfrak{d})$ corresponds to the fracture counterpart.

The free-energy is assumed to comply with the simple form:

$$\Psi(\boldsymbol{\varepsilon}, \mathfrak{d}) = g(\mathfrak{d})\Psi^e(\boldsymbol{\varepsilon}), \tag{1.28}$$

ÁMBITO- PREFIJO
GEISER
Nº registro
O00008744e2000024753
CSV
GEISER-aa34-5f08-a669-4b6e-9258-ed2f-d009-e7f3
DIRECCIÓN DE VALIDACIÓN
FECHA Y HORA DEL DOCUMENTO
19/06/2020 12:08:12 Horario peninsular
GEISER-aa34-5f08-a669-4b6e-9258-ed2f-d009-e7f3

where $\Psi^e(\boldsymbol{\varepsilon})$ is the effective elastic strain energy for undamaged material. The degradation function can be expressed by the simple form $g(\mathfrak{d}) = (1-\mathfrak{d})^2$, satisfying $\Psi(\boldsymbol{\varepsilon}, 0) = \Psi^e(\boldsymbol{\varepsilon})$, $\Psi(\boldsymbol{\varepsilon}, 1) = 0$, and $\partial_{\mathfrak{d}}\Psi(\boldsymbol{\varepsilon}, \mathfrak{d}) < 0$ in order to ensure the thermodynamics consistency.

With respect to the fracture term in Eq.(1.27), in [45, 46], it is stated that a simple criterion for brittle fracture without threshold (for damage activation) can be expressed via the exploitation of the crack density functional in the spirit of Griffith's theory as follows:

$$W_{\text{frac}}(\mathfrak{d}, \nabla\mathfrak{d}) = \mathscr{G}_c\, \gamma(\mathfrak{d}, \nabla\mathfrak{d}) = \mathscr{G}_c\, \left[\frac{1}{2l}\mathfrak{d}^2 + \frac{l}{2}|\nabla\mathfrak{d}|^2\right]. \tag{1.29}$$

Through the insertion of Eq.(1.29) into Eq(1.27), and the assessment of the loading criterion via the computation $-\partial_{\mathfrak{d}} W(\boldsymbol{\varepsilon}, \mathfrak{d}, \nabla\mathfrak{d})$, it is possible to observe that the corresponding driving force of fracture accounts for the ratio of the total effective elastic work with respect to $\mathscr{G}_c$, but it predicts damage progression even at low levels of elastic and plastic deformation (i.e. right from the beginning of the computations). In this regard, an alternative expression for the crack driving force $\mathscr{H}$ is proposed in [47], which has been subsequently exploited in [44]. Following a similar approach to that given in [44, 47] but including a phenomenological failure criterion, the following form of the crack driving force can be postulated:

$$\mathscr{H} = \xi \left[\langle \frac{\max\limits_{\tau\in[0,t]} \Psi^e(\tau)}{\Psi^e_{\text{init}}} - 1 \rangle_+ \right]. \tag{1.30}$$

Note that $\mathscr{H}$ ensures the positive evolution of the phase-field variable, i.e. $\dot{\mathfrak{d}} \geq 0$, Ψ^e is the maximum ever reached effective elastic energy, Ψ^e_{init} is the effective elastic energy for damage initiation, and ξ is a dimensionless parameter that triggers the activation of damage due to the elastic contribution but also governs the post-peak behavior. Eq.(1.30) represents a generic form of a crack driving force. Notwithstanding that the current formulation allows the incorporation of phenomenologically-based failure criteria to control the activation and evolution of the phase-field. It is worth noting that it also allows accommodating any other definition of a crack driving force or initiation criteria.

Correspondingly, the phase-field problem can be solved using the following expression:

$$2(1-\mathfrak{d})\mathfrak{P}\mathscr{H} = \mathscr{G}_c\delta_{\mathfrak{d}}\gamma(\mathfrak{d}, \nabla\mathfrak{d}) \text{ in } \mathscr{B} \text{ and } \nabla\mathfrak{d}\cdot\mathbf{n} = 0 \text{ on } \partial\mathscr{B}. \tag{1.31}$$

Here, $\mathfrak{P}$ is an activation flag for the crack driving force which is activated if and only if its respective failure criterion is met.

Based on the previous definitions, the functional that postulates the phase-field method to fracture is given by:

$$\Pi(\mathbf{u}, \mathfrak{d}) = \Pi_{\text{int}}(\mathbf{u}, \mathfrak{d}) + \Pi_{\text{ext}}(\mathbf{u}), \tag{1.32}$$

where $\Pi_{\text{int}}(\mathbf{u}, \mathfrak{d})$ and $\Pi_{\text{ext}}(\mathbf{u})$ are the internal and external contribution to the energy functional, respectively:

$$\Pi_{\text{int}}(\mathbf{u}, \mathfrak{d}) = \int_{\mathscr{B}} W(\boldsymbol{\varepsilon}, \mathfrak{d}, \nabla\mathfrak{d})\mathrm{d}\Omega = \int_{\mathscr{B}} \Psi(\boldsymbol{\varepsilon}(\mathbf{u}), \mathfrak{d})\mathrm{d}\Omega + \int_{\mathscr{B}} \mathscr{G}_c\gamma(\mathfrak{d}, \nabla\mathfrak{d})\mathrm{d}\Omega, \tag{1.33}$$

$$\Pi_{\text{ext}}(\mathbf{u}) = -\int_{\mathscr{B}} \mathbf{f}_v \mathrm{d}\Omega - \int_{\partial\mathscr{B}_t} \bar{\mathbf{t}}\mathrm{d}\partial\Omega, \tag{1.34}$$

where $\mathbf{f}_v$ is the prescribed body actions.

ÁMBITO- PREFIJO
GEISER
Nº registro
O00008744e2000024753
CSV
GEISER-aa34-5f08-a669-4b6e-9258-ed2f-d009-e7f3
DIRECCIÓN DE VALIDACIÓN
FECHA Y HORA DEL DOCUMENTO
19/06/2020 12:08:12 Horario peninsular
GEISER-aa34-5f08-a669-4b6e-9258-ed2f-d009-e7f3

Following the standard Bubnov-Galerkin method, the trial solutions of the two primary fields with:

$$\mathbf{u} \in \mathscr{U}_u := \left\{ \mathbf{u} \in H^1(\mathscr{B}) | \nabla \mathbf{u} \in L^2(\mathscr{B});\ \mathbf{u} = \bar{\mathbf{u}} \text{ on } \partial \mathscr{B}_u \right\},$$

$$\mathfrak{d} \in \mathscr{U}_{\mathfrak{d}} := \left\{ \mathfrak{d} \in H^1(\mathscr{B}) | \mathfrak{d}(\mathbf{x}) \in [0,1],\ \dot{\mathfrak{d}} \geq 0,\ \forall \mathbf{x} \in \mathscr{B} \right\},$$

are extended by the corresponding test functions:

$$\delta \mathbf{u} \in \mathscr{V}_u := \left\{ \delta \mathbf{u} \in H^1(\mathscr{B}) | \nabla \delta \mathbf{u} \in L^2(\mathscr{B});\ \delta \mathbf{u} = \mathbf{0} \text{ on } \partial \mathscr{B}_u \right\},$$

$$\delta \mathfrak{d} \in \mathscr{V}_{\mathfrak{d}} := \left\{ \delta \mathfrak{d} \in H^1(\mathscr{B}) | \delta \mathfrak{d} \geq 0,\ \forall \mathbf{x} \in \mathscr{B} \right\},$$

where H^1 denotes the Sobolev space. There accordingly, the weak form of the fracture problem is constructed as follows:

$$\delta \Pi(\mathbf{u},\mathfrak{d},\delta \mathbf{u},\delta \mathfrak{d}) = \delta \Pi_{\text{int}}(\mathbf{u},\mathfrak{d},\delta \mathbf{u},\delta \mathfrak{d}) + \delta \Pi_{\text{ext}}(\mathbf{u},\delta \mathbf{u}) = 0. \tag{1.35}$$

After simple algebraic manipulations, the strong form of the field equations is reached:

$$\text{div}\boldsymbol{\sigma} + \mathbf{f}_v = \mathbf{0} \text{ in } \mathscr{B} \text{ and } \boldsymbol{\sigma} \cdot \mathbf{n} = \bar{\mathbf{t}} \text{ on } \partial \mathscr{B}_t, \tag{1.36}$$

$$2(1-\mathfrak{d})\mathfrak{P}\mathscr{H} = \mathscr{G}_c \delta_{\mathfrak{d}} \gamma(\mathfrak{d}, \nabla \mathfrak{d}) \text{ in } \mathscr{B} \text{ and } \nabla \mathfrak{d} \cdot \mathbf{n} = 0 \text{ on } \partial \mathscr{B}. \tag{1.37}$$

Owing to the regularity of the energetic functions, first-order optimality condition is sufficient to ensure stability and energy balance leading to the following Karush-Kuhn-Tucker (KKT) conditions:

$$\dot{\mathfrak{d}} \geq 0, \tag{1.38}$$

$$2(1-\mathfrak{d})\mathfrak{P}\mathscr{H} - \mathscr{G}_c \delta_{\mathfrak{d}} \gamma(\mathfrak{d}, \nabla \mathfrak{d}) \leq 0, \tag{1.39}$$

$$\left(2(1-\mathfrak{d})\mathfrak{P}\mathscr{H} - \mathscr{G}_c \delta_{\mathfrak{d}} \gamma(\mathfrak{d}, \nabla \mathfrak{d})\right) \dot{\mathfrak{d}} = 0. \tag{1.40}$$

The solution of the aforementioned coupled displacement-crack phase-field is obtained after discretizing the space using the finite element method. This means, the continuous domain of the body $\mathscr{B}$ is approximated by a discrete domain $\mathscr{B}^h$ that is formed by a finite number of disjoints elements $\mathscr{B}^e$. There accordingly, the infinite-dimensional function spaces $\mathscr{U}$ and $\mathscr{V}$ are approximated by the corresponding finite-dimensional subspaces $\mathscr{U}^h$ and $\mathscr{V}^h$, imposing the same conditions on the boundaries.

1.6 Objectives and Outlines

In view of the State of the Art, this work represents a novel contribution to the computational modeling of anisotropic fracture of fiber reinforced polymers. In particular, the comprehensive extension of the phase-field approach to fracture for its application to such materials is conducted in a comprehensive and detailed scheme.

ÁMBITO- PREFIJO
GEISER
Nº registro
O00008744e2000024753
CSV
GEISER-aa34-5f08-a669-4b6e-9258-ed2f-d009-e7f3
DIRECCIÓN DE VALIDACIÓN
FECHA Y HORA DEL DOCUMENTO
19/06/2020 12:08:12 Horario peninsular
GEISER-aa34-5f08-a669-4b6e-9258-ed2f-d009-e7f3

The general objective of the present thesis concerns the achievement of a new modeling vision for triggering fracture events in SFRPs and LFRPs within the spirit of the phase-field methods using non-linear FEM methodologies. The particular target of the present work is threefold:

- The development of an anisotropic phase-field model for ductile fracture of short fiber reinforced polymers.
- The development of a multi phase-field model based on Puck theory of failure for anisotropic fracture of long fiber reinforced polymers.
- The employment of the newly developed multi phase-field model together with a cohesive zone model into the modeling and simulation of delamination migration in multi-layered long fiber reinforced polymers.

This thesis is divided into five chapters. The arrangement of the remaining Chapters of the present document is as follows:

- Subsequent to this introductory chapter, a novel phenomenological phase-field model to predict the anisotropic ductile fracture of SFRPs is presented in Chapter 2. In particular, an invariant-based elasto-plastic model is consistently coupled with the phase-field approach to model the anisotropic ductile fracture response of SFRPs. The employed elasto-plastic model adopts a pressure-dependent yield surface and non-associative plastic evolution. The constructed energy-consistent variational formulation exploits a modular format with a consistent generalization of the crack driving function in which the elastic and plastic contribution of the energy are concomitantly considered. A phenomenological asymmetric failure criterion is employed to control the activation and evolution of the phase-field. However, the proposed generic form of the crack driving function allows the incorporation of any failure criterion. The presented formulation is implemented into the Finite Element (FE) code `ABAQUS` adopting a staggered solution scheme. Hence, for this purpose, the user-defined capabilities `UMAT` and `UEL` are utilized. The model is calibrated on the basis of experiments conducted on injection-molded SFRPs sheets. Different numerical examples are presented to demonstrate the predictive capabilities of the proposed formulation.
- In Chapter 3, a new multi phase-field model is proposed for predicting intra-laminar fracture of FRPs. The formulation incorporates two independent phase-field variables and length scales to differentiate between fiber and inter-fiber (matrix-dominated) failure mechanisms. For matrix-dominated loading states, the proposed formulation considers the plastic effects via an invariant-based pressure-dependent plasticity model. The physically motivated failure criterion of Puck is employed to control the activation and evolution of the fiber and inter-fiber phase-field. The corresponding governing equations in terms of variational formulation is implemented into the FE code `ABAQUS` utilizing the user-defined subroutines `UMAT` and `UEL`. Several representative applications are presented and discussed to pinpoint the applicability of the proposed computational tool.
- Focusing on complex practical applications, in Chapter 4, the numerical simulation of delamination migration in FRPs is presented. For this purpose, a FE modeling procedure is employed in `ABAQUS` (via the user-defined capabilities `UMAT` and `UEL`) integrating the newly developed multi phase-field model for intra-laminar fracture with a cohesive zone model for inter-laminar decohesion failure. The employed cohesive zone model endowing a bi-linear traction separation law in the interface. Special emphasis is made on thermodynamics consistency and variational formalism of the coupled fracture fields. The built model is applied to predict delamination migration in fiber reinforced laminates and the numerical results are compared against experimental data to assess the competence of the model.

- Chapter 5 summarizes the main results and draws the conclusions of this thesis. Finally, some propositions for future research are provided.

ÁMBITO- PREFIJO
GEISER
Nº registro
O00008744e2000024753
CSV
GEISER-aa34-5f08-a669-4b6e-9258-ed2f-d009-e7f3
DIRECCIÓN DE VALIDACIÓN
FECHA Y HORA DEL DOCUMENTO
19/06/2020 12:08:12 Horario peninsular
GEISER-aa34-5f08-a669-4b6e-9258-ed2f-d009-e7f3

2 A Phase-Field Model for Ductile Fracture of Short Fiber Reinforced Polymers

This chapter presents a paper which proposes a novel phase-field model that accounts for the anisotropic ductile fracture response of short fiber reinforced polymers. The paper is published in Theoretical and Applied Fracture Mechanics, Volume 106, April 2020, Paper 102495.

ÁMBITO- PREFIJO
GEISER
Nº registro
O00008744e2000024753

CSV
GEISER-aa34-5f08-a669-4b6e-9258-ed2f-d009-e7f3
DIRECCIÓN DE VALIDACIÓN

FECHA Y HORA DEL DOCUMENTO
19/06/2020 12:08:12 Horario peninsular

GEISER-aa34-5f08-a669-4b6e-9258-ed2f-d009-e7f3

Abstract. Fracture events in Short Fiber Reinforced polymers (SFRPs) are one of the most limiting phenomena for their widespread use in many engineering applications, especially involving lightweight structures. In this investigation, a novel Phase-Field (PF) model that accounts for the anisotropic response of SFRPs is outlined from the theoretical and numerical standpoints. The regularized crack surface functional, which characterizes PF methods, allows overcoming operative difficulties for complex crack topologies in engineering structures. In particular, we exploit an invariant-based phenomenological elasto-plastic material model for the macroscopic response of SFRPs with pressure-dependent behavior that is consistently coupled with the PF approach for ductile fracture. The anisotropic character of SFRPs is incorporated into the elasto-plastic and the fracture response. In contrast to previous investigations on the matter, one novel ingredient of the proposed formulation is the use of a non-associative anisotropic plastic evolution. The current variational formulation also exploits a modular format with a consistent generalization of the crack driving function for SFRPs. The performance of the current modeling approach is examined by means of representative applications, showing its robustness and reliability.

2.1 Introduction

Fracture events notably condition the integrity and durability of many engineering products in practical applications. The achievement of a profound understanding with regard to the different aspects affecting the initiation and propagation of fracture in engineering materials and structures has been a recurrent topic of research in the last decades. Concepts addressing this issue can be traced back to the seminal developments within the context of Linear Elastic Fracture Mechanics (LEFM), and cohesive-like crack methods.

In this setting, recent advances in computational capabilities have promoted the active development of different modeling strategies, mostly based on the Finite Element Method (FEM). Cohesive-like methods [48–52], the eXtended FEM (XFEM) [53] and the Strong Discontinuity Approach (SDA) [54] can be categorized as numerical techniques that encompass a strong discontinuous displacement jump across the crack flanks, leading to a sharp crack representation. Despite the intensive development of such sharp crack approaches over the last two decades, these strategies generally encounter notable difficulties in situations with intricate crack topologies including crack branching, coalescence, among other scenarios. These difficulties have stimulated a renovated interest in diffusive crack models as is the case of the Phase-Field (PF) approach to fracture as was originally proposed in [13], and its numerical treatment was addressed in [14, 15]. Posterior studies on PF methods regarded the evaluation of its thermodynamics consistency, which was thoroughly developed [43,55] following an engineering perspective. These investigations are based on the Griffith-approach to brittle fracture in elastic bodies [24], encompassing a non-local treatment of damage, but rooted in fracture mechanics concepts and devising a robust multi-field variational formalism via the exploitation of the Γ-convergence concept [12]. Accordingly, PF methods are characterized by accounting for the corresponding stiffness degradation at the material point level, which is triggered through the definition of the PF crack variable.

In the last years, PF methods have attracted a great deal of research extending this approach towards the treatment of quasi-brittle fracture [56, 57], failure in heterogeneous media via its coupling with interface-crack models [58, 59], ductile fracture [60], to quote a few of them. Formulations for ductile fracture have been rigorously treated in [45,46], whereby a generalization of the so-called crack driving force was carried out. Thus, owing to its canonical format, PF strategies have been proven to be a competitive modeling tool, for the prediction of failure events in many engineering materials. Recent applications comprise soft materials [38], hydrogen assisted cracking [61], hydraulic fracturing [62], frictional materials [63], among many others.

ÁMBITO- PREFIJO
GEISER
Nº registro
O00008744e2000024753

CSV
GEISER-aa34-5f08-a669-4b6e-9258-ed2f-d009-e7f3
DIRECCIÓN DE VALIDACIÓN

FECHA Y HORA DEL DOCUMENTO
19/06/2020 12:08:12 Horario peninsular

GEISER-aa34-5f08-a669-4b6e-9258-ed2f-d009-e7f3

Within the context of anisotropic materials, recent works embedded the anisotropic effects into the corresponding variational formalism of fracture through the use of a structural tensor, **A** (generally a second-order material tensor for low-order PF models), characterizing the internal material direction. For bio-materials in soft issues applications, an extension of the PF approach to fracture has been proposed in [38,64], in which the dissipative term is equipped with a directional-based tensor for large deformations. A similar structure but also including second gradients of the PF track variable has been addressed in [39]. Further developments have accounted for the treatment of fracture events using PF formulation in Long Fiber Reinforced Polymers (LFRPs), which are characterized by an anisotropic material response. Particularly, in [65] a PF model has been outlined via the definition of several PF crack variables in the canonical formulation aiming at distinguishing between different failure mechanisms. An alternative simplified PF model has been formulated in [66], in which the existence of a predominant failure mechanism at the material point is assumed, and therefore leading to the consideration of a single PF variable for the material degradation but affecting different entries of the corresponding stiffness (elasticity) tensor.

Alternative composite materials with a strong impact on many engineering products are those denominated as Short Fiber Reinforced Polymers (SFRPs), which allow the achievement of high production rates with intricate geometrical definitions. These materials have been extensively used in car constructions in the last years, among many other lightweight applications. As a consequence of this increasing interest, SFRPs have been comprehensively characterized by different authors, see [67–72], among many others. Further investigations on the topic were more focused on addressing the fracture response of SFRPs, see [73–76], and the references therein. From a modeling standpoint, as fiber orientation play a fundamental role in the macroscopic response of SFRPs, several numerical methods relying on FEM haven been proposed so far [77–79]. Complying with multi-scale models for SFRPs, several studies have conducted rigorous numerical treatments in order to capture such anisotropic material response [80, 81], see the review conducted in [82]. Differing from this computationally demanding multi-scale perspective, phenomenological approaches followed a completely different methodology, which can be efficiently used at the structural component level. In this concern, recalling the invariant-based approach, see [83, 84], the authors in [85–89] have intensively enhanced such formulation for the treatment of SFRPs for mechanical and thermo-mechanical scenarios following an invariant-based elasto-plastic framework. However, up to now, especially using the variational-based computational methods, the fracture treatment of SFRPs has received scarce attention within the scientific community. Consequently, the principal aim of this contribution is the development of a ductile fracture modeling framework within the context of the PF method for SFRPs undergoing infinitesimal deformations. In particular, the integration of an invariant-based pressure-dependent elasto-plastic material model for SFRPs into the PF method using a general variational formalism is outlined, in which the corresponding numerical discretization can be implemented in most of the standard Finite Element (FE) codes.

This chapter is organized as follows. Section 2.2 outlines the variational formulation and the constitutive approach at the material point level for SFRPs. Therein, careful attention is devoted to the definition of a new type of crack driving force. Once the variational formalism and the elasto-plastic model are presented, Section 2.3 examines the performance of the proposed formulation through different representative applications. For this purpose, the presented formulation is implemented in the commercial FE code `ABAQUS`. Finally, the main contributions of this study are resumed in Section 2.4.

2.2 Variational Formulation and Constitutive Modeling Approach for SFRPs

This section concerns the fundamental aspects regarding the variational formalism of the phase-field approach for ductile fracture and the constitutive formulation for SFRPs. Note that the formulation presented subsequently is restricted to infinitesimal deformation analysis, though the consistent extension to finite deformation applications can be conducted following the variational forms proposed in [45, 46, 90–92] and the constitutive models developed in [85–87, 89].

2.2.1 Phase-Field Approach to Ductile Fracture: General Modeling Framework

The key concept for the phase-field approach to fracture comprises the regularization of a sharp crack topology Γ_c by a diffusive crack within a diffusive crack zone of width l, Figure 2.1. This approximation is based on the definition of the so-called phase-field crack variable $\mathfrak{d} : \mathscr{B} \times [0,t] \rightarrow [0,1]$, which is a smooth function within the domain characterizing for $\mathfrak{d} = 0$ and $\mathfrak{d} = 1$ the intact and the cracked states, respectively, see [15]. This variable is defined within the body under consideration $\mathscr{B}$ and its evolution is ruled by a suitable temporal expression within the time interval $[0,t]$ along the deformation process (t denotes the deformed state).

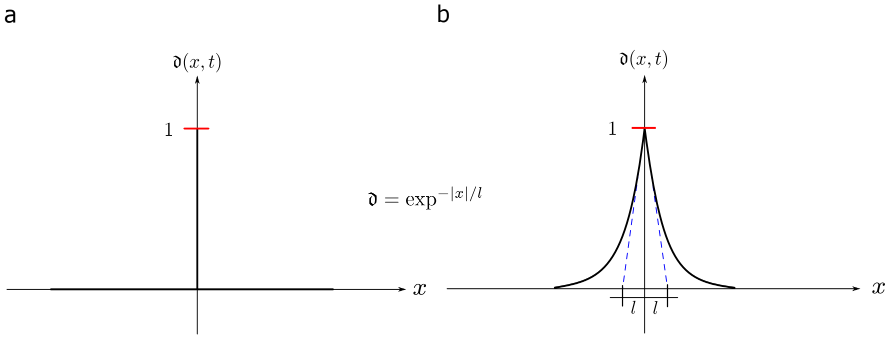

Figure 2.1 One-dimensional problem: (a) sharp crack representation at $x = 0$ and (b) regularized crack topology at $x = 0$, depending on the length scale l.

For the application of the PF method within a multi-dimensional framework, let us consider an arbitrary body whose domain is denoted by $\mathscr{B} \in \mathbb{R}^{n_{\text{dim}}}$ (n_{dim} is the dimension of the analysis), whilst its delimiting boundary is identified by $\partial\mathscr{B} \in \mathbb{R}^{n_{dim}-1}$. The displacement field is denoted by $\mathbf{u} : \mathscr{B} \rightarrow \mathbb{R}^{n_{\text{dim}}}$ and the strain tensor is defined by $\boldsymbol{\varepsilon} := \nabla^{\text{sym}}\mathbf{u}$ with $\boldsymbol{\varepsilon} : \mathscr{B} \rightarrow \mathbb{R}^{n_{\text{dim}} \times n_{\text{dim}}}$. The Cauchy stress tensor is denoted as $\boldsymbol{\sigma} : \mathscr{B} \rightarrow \mathbb{R}^{n_{\text{dim}} \times n_{\text{dim}}}$. Prescribed displacement conditions are given by $\mathbf{u} = \bar{\mathbf{u}}$ on $\partial\mathscr{B}_u$, whereas prescribed tractions conditions on the corresponding portion of the boundary are denoted as $\bar{\mathbf{t}} = \boldsymbol{\sigma} \cdot \mathbf{n}$ on $\partial\mathscr{B}_t$. These boundary conditions comply with the requirements: $\overline{\partial\mathscr{B}_t \cup \partial\mathscr{B}_u} = \partial\mathscr{B}$ and $\partial\mathscr{B}_t \cap \partial\mathscr{B}_u = \emptyset$, where $\mathbf{n}$ is the external outer normal vector to the body (Figure 2.2). Based on the key concept of PF [13, 15], for multi-dimensional analysis the fracture energy is approximated by:

$$\int_{\Gamma_c} \mathscr{G}_c \mathrm{d}\Gamma_c \approx \int_{\mathscr{B}} \mathscr{G}_c \gamma(\mathfrak{d}, \nabla\mathfrak{d}) \Omega, \tag{2.1}$$

where $\mathscr{G}_c$ is the bulk critical energy release rate and $\gamma(\mathfrak{d}, \nabla\mathfrak{d})$ is the so-called crack surface density functional.

ÁMBITO- PREFIJO
GEISER
Nº registro
O00008744e2000024753
CSV
GEISER-aa34-5f08-a669-4b6e-9258-ed2f-d009-e7f3
DIRECCIÓN DE VALIDACIÓN
FECHA Y HORA DEL DOCUMENTO
19/06/2020 12:08:12 Horario peninsular
GEISER-aa34-5f08-a669-4b6e-9258-ed2f-d009-e7f3

Different authors assumed the quadratic form of the crack surface density functional and which was successfully applied to isotropic materials [55]:

$$\gamma(\mathfrak{d},\nabla\mathfrak{d}) = \frac{1}{2l}\mathfrak{d}^2 + \frac{l}{2}\left|\nabla\mathfrak{d}\right|^2. \tag{2.2}$$

Note, that the expression above is also governed by the length scale parameter l which can be related to the apparent material strength [93]:

$$l = \frac{27}{256}\frac{E\mathscr{G}_c}{\sigma_s^2}, \tag{2.3}$$

where E denotes the Young modulus and σ_s is the material strength.

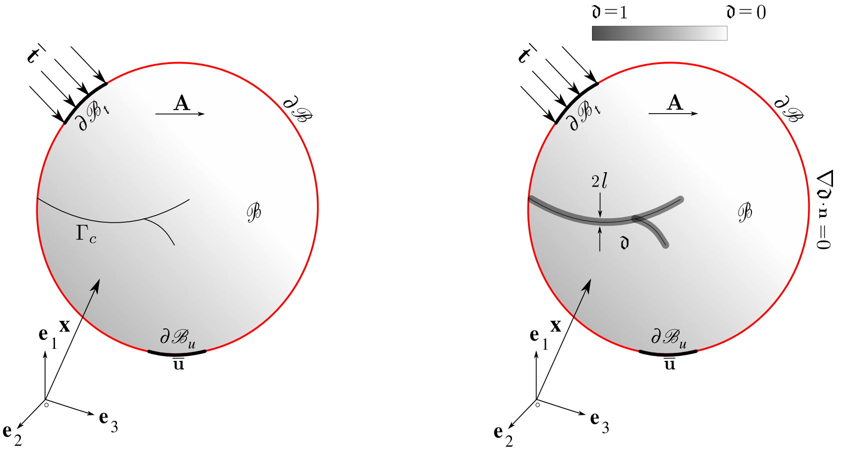

Figure 2.2 Phase-field method for diffusive crack modelling for anisotropic materials: (a) sharp crack representation and (b) regularized crack topology.

For the case of anisotropic solids, the previous form of $\gamma(\mathfrak{d},\nabla\mathfrak{d})$ can be accordingly modified for the consideration of anisotropic crack density. Recalling [39, 65, 66], a simple anisotropic crack functional that introduces the directional response into such functional is given by:

$$\gamma(\mathfrak{d},\nabla\mathfrak{d},\mathbf{A}) = \frac{1}{2l}\mathfrak{d}^2 + \frac{l}{2}\nabla\mathfrak{d}\cdot\hat{\mathbf{A}}\cdot\nabla\mathfrak{d}, \tag{2.4}$$

where $\hat{\mathbf{A}} = \mathbf{1} + \hat{\alpha}\mathbf{A}$ is a second-order tensor reflecting the material anisotropy, $\mathbf{1}$ denotes the second-order identity, $\hat{\alpha}$ stands for a parameter that weights the material direction $\mathbf{a}$, and the so-called structural tensor defined as $\mathbf{A} = \mathbf{a}\otimes\mathbf{a}$. Note that setting $\hat{\alpha} = 0$, the isotropic formulation is fully recovered.

In a general form, according to [45, 46], the phase-field method to fracture can resemble a class of gradient damage approach. This allows the postulation of the *total pseudo-energy density* W per unit volume for anisotropic elasto-plastic solids:

$$W(\boldsymbol{\varepsilon},\boldsymbol{\varepsilon}^p,\hat{w}^p,\mathfrak{d},\nabla\mathfrak{d},\mathbf{A}) = \Psi^e(\boldsymbol{\varepsilon}-\boldsymbol{\varepsilon}^p,\mathfrak{d},\mathbf{A}) + \Psi^p(\hat{w}^p,\mathfrak{d},\mathbf{A}) + W_{\text{frac}}(\mathfrak{d},\nabla\mathfrak{d},\mathbf{A}), \tag{2.5}$$

where $\Psi^e(\boldsymbol{\varepsilon}-\boldsymbol{\varepsilon}^p,\mathfrak{d},\mathbf{A})$ is the elastic bulk energy per unit volume, $\Psi^p(\hat{w}^p,\mathfrak{d},\mathbf{A})$ is the energy contribution associated with the plastic deformation and $W_{\text{frac}}(\mathfrak{d},\nabla\mathfrak{d},\mathbf{A})$ corresponds to the fracture counterpart. The particular forms of the elastic and plastic terms are outlined in Subsection 2.2.2 for SFRPs. Moreover, it is worth noting that in the previous expression the additive decomposition

ÁMBITO- PREFIJO
GEISER
Nº registro
O00008744e2000024753
CSV
GEISER-aa34-5f08-a669-4b6e-9258-ed2f-d009-e7f3
DIRECCIÓN DE VALIDACIÓN
FECHA Y HORA DEL DOCUMENTO
19/06/2020 12:08:12 Horario peninsular
GEISER-aa34-5f08-a669-4b6e-9258-ed2f-d009-e7f3

of the total strain tensor into elastic $\boldsymbol{\varepsilon}^e$ and plastic $\boldsymbol{\varepsilon}^p$ counterparts was assumed: $\boldsymbol{\varepsilon} = \boldsymbol{\varepsilon}^e + \boldsymbol{\varepsilon}^p$. Finally, $\hat{w}^p$ is the accumulated effective plastic dissipation.

The elastic contribution is assumed to comply with the simple form:

$$\Psi^e(\boldsymbol{\varepsilon} - \boldsymbol{\varepsilon}^p, \mathfrak{d}, \mathbf{A}) = (1-\mathfrak{d})^2 \hat{\Psi}^e(\boldsymbol{\varepsilon}^e, \mathbf{A}), \tag{2.6}$$

where $\hat{\Psi}^e(\boldsymbol{\varepsilon}^e, \mathbf{A})$ is the effective elastic strain energy for undamaged material. The degradation function is given by $g(\mathfrak{d}) = (1-\mathfrak{d})^2$, satisfying $\Psi^e(\boldsymbol{\varepsilon} - \boldsymbol{\varepsilon}^p, 0, \mathbf{A}) = \hat{\Psi}^e(\boldsymbol{\varepsilon}^e, \mathbf{A})$, $\Psi^e(\boldsymbol{\varepsilon} - \boldsymbol{\varepsilon}^p, 1, \mathbf{A}) = 0$, and $\partial_{\mathfrak{d}} \Psi^e(\boldsymbol{\varepsilon} - \boldsymbol{\varepsilon}^p, \mathfrak{d}, \mathbf{A}) < 0$ in order to ensure the thermodynamics consistency.

Similarly, the plastic contribution renders:

$$\Psi^p(\hat{w}^p, \mathfrak{d}, \mathbf{A}) = g(\mathfrak{d}) \hat{w}^p(\boldsymbol{\varepsilon}^p, \mathbf{A}). \tag{2.7}$$

Note that the adoption of the same degradation function for the elastic and plastic contributions via $g(\mathfrak{d})$ is a particular choice that can be modified in a straightforward manner.

With respect to the fracture term in Eq.(2.5), in [45, 46], it is stated that a simple criterion for brittle fracture without threshold (for damage activation) can be expressed via the exploitation of the crack density functional in the spirit of Griffith's theory as follows:

$$W_{\text{frac}}(\mathfrak{d}, \nabla\mathfrak{d}, \mathbf{A}) = \mathscr{G}_c \, \gamma(\mathfrak{d}, \nabla\mathfrak{d}, \mathbf{A}) = \mathscr{G}_c \left[\frac{1}{2l}\mathfrak{d}^2 + \frac{l}{2} \nabla\mathfrak{d} \cdot \hat{\mathbf{A}} \cdot \nabla\mathfrak{d} \right]. \tag{2.8}$$

Through the insertion of Eq.(2.8) into Eq.(2.5), and the assessment of the loading criterion via the computation $-\partial_{\mathfrak{d}} W(\boldsymbol{\varepsilon}, \boldsymbol{\varepsilon}^p, \hat{w}^p, \mathfrak{d}, \nabla\mathfrak{d}, \mathbf{A})$, it is possible to observe that the corresponding driving force of fracture accounts for the ratio of the total effective elastic-plastic work with respect to $\mathscr{G}_c$, but it predicts damage progression even at low levels of elastic and plastic deformation (i.e. right from the beginning of the computations). In this regard, in [90] an alternative expression for the crack driving force $\mathscr{H}$ has been proposed which was subsequently exploited in [91, 92]. Following a similar approach to that given in [90–92] but including a phenomenological failure criterion (Section 2.2.2.4), the following form of the crack driving force is postulated:

$$\mathscr{H} = \xi^e \left[\left\langle \frac{\max\limits_{\tau\in[0,t]} \hat{\Psi}^e(\tau)}{\hat{\Psi}^e_{\text{init}}} - 1 \right\rangle_+ \right] + \xi^p \left[\left\langle \frac{\hat{\Psi}^p}{\hat{\Psi}^p_{\text{init}}} - 1 \right\rangle_+ \right]. \tag{2.9}$$

Note that $\mathscr{H}$ ensures the positive evolution of the PF variable, i.e. $\dot{\mathfrak{d}} \geq 0$; $\hat{\Psi}^e$ is the maximum ever reached effective elastic energy, $\hat{\Psi}^e_{\text{init}}$ is the effective elastic energy for damage initiation (in connection with Section 2.2.2.4), and ξ^e is a dimensionless parameter that triggers the activation of damage due to the elastic contribution but also governs the post-peak behavior. Similarly, in Eq.(2.9), $\hat{\Psi}^p$ is the effective plastic energy, $\hat{\Psi}^p_{\text{init}}$ is the effective plastic energy for damage initiation, and ξ^p is a parameter that tracking the activation plastic-induced fracture. Eq.(2.9) represents a generic form of a crack driving force in which the elastic and plastic contribution of the energy are concomitantly considered. In particular, as stated above, the invariant-based and pressure-dependent failure criterion described in Section 2.2.2.4 is adopted. Notwithstanding that the current formulation allows the incorporation of phenomenologically-based failure criteria to control the activation and evolution of the phase-field. It is worth noting that it also allows accommodating any other definition of a crack driving force or initiation criteria.

The particular meaning of the previous effective energy contributions is detailed in Section 2.2.2. Moreover, it is worth mentioning that the effective plastic work complies with a monotonically increasing function and therefore no further constraints are required in order to enforce the crack growth due to plastic deformation.

ÁMBITO- PREFIJO
GEISER
Nº registro
O00008744e2000024753

CSV
GEISER-aa34-5f08-a669-4b6e-9258-ed2f-d009-e7f3
DIRECCIÓN DE VALIDACIÓN

FECHA Y HORA DEL DOCUMENTO
19/06/2020 12:08:12 Horario peninsular

GEISER-aa34-5f08-a669-4b6e-9258-ed2f-d009-e7f3

Correspondingly, the phase-field problem can be solved using the following expression:

$$2(1-\mathfrak{d})\mathfrak{P}\mathscr{H} = \mathscr{G}_c \delta_{\mathfrak{d}} \gamma(\mathfrak{d},\nabla) \text{ in } \mathscr{B} \text{ and } \nabla\mathfrak{d}\cdot\mathbf{n} = 0 \text{ in } \partial\mathscr{B}, \tag{2.10}$$

where $\mathfrak{P}$ is an activation flag for the crack driving force which is activated if and only if its respective failure criterion is met.

Based on the previous definitions, the functional that postulates the phase-field method to ductile fracture is given by:

$$\Pi(\mathbf{u},\mathfrak{d}) = \Pi_{\text{int}}(\mathbf{u},\mathfrak{d}) + \Pi_{\text{ext}}(\mathbf{u}), \tag{2.11}$$

where $\Pi_{\text{int}}(\mathbf{u},\mathfrak{d})$ and $\Pi_{\text{ext}}(\mathbf{u})$ are the internal and external contribution to the energy functional, respectively:

$$\begin{aligned}\Pi_{\text{int}}(\mathbf{u},\mathfrak{d}) = \int_{\mathscr{B}} W(\boldsymbol{\varepsilon},\boldsymbol{\varepsilon}^p,\hat{w}^p,\mathfrak{d},\nabla\mathfrak{d},\mathbf{A})\mathrm{d}\Omega &= \int_{\mathscr{B}} \Psi^e(\boldsymbol{\varepsilon}-\boldsymbol{\varepsilon}^p,\mathfrak{d},\mathbf{A}) + \Psi^p(\hat{w}^p,\mathfrak{d},\mathbf{A})\mathrm{d}\Omega \\ &+ \int_{\mathscr{B}} \mathscr{G}_c \gamma(\mathfrak{d},\nabla\mathfrak{d},\mathbf{A})\mathrm{d}\Omega,\end{aligned} \tag{2.12}$$

$$\Pi_{\text{ext}}(\mathbf{u}) = -\int_{\mathscr{B}} \mathbf{f}_v \mathrm{d}\Omega - \int_{\partial\mathscr{B}_t} \bar{\mathbf{t}}\mathrm{d}\partial\Omega, \tag{2.13}$$

where $\mathbf{f}_v$ is the deformation-independent volume-specific loads.

Recalling the standard Bubnov-Galerkin method, the trial solutions of the two primary fields with:

$$\mathbf{u} \in \mathscr{U}_u := \left\{\mathbf{u} \in H^1(\mathscr{B}) | \nabla\mathbf{u} \in L^2(\mathscr{B});\ \mathbf{u} = \bar{\mathbf{u}} \text{ on } \partial\mathscr{B}_u\right\},$$

$$\mathfrak{d} \in \mathscr{U}_{\mathfrak{d}} := \left\{\mathfrak{d} \in H^1(\mathscr{B}) | \mathfrak{d}(\mathbf{x}) \in [0,1],\ \dot{\mathfrak{d}} \geq 0,\ \forall \mathbf{x} \in \mathscr{B}\right\},$$

are extended by the corresponding test functions:

$$\delta\mathbf{u} \in \mathscr{V}_u := \left\{\delta\mathbf{u} \in H^1(\mathscr{B}) | \nabla\delta\mathbf{u} \in L^2(\mathscr{B});\ \delta\mathbf{u} = \mathbf{0} \text{ on } \partial\mathscr{B}_u\right\},$$

$$\delta\mathfrak{d} \in \mathscr{V}_{\mathfrak{d}} := \left\{\delta\mathfrak{d} \in H^1(\mathscr{B}) | \delta\mathfrak{d} \geq 0,\ \forall \mathbf{x} \in \mathscr{B}\right\},$$

where H^1 denotes the Sobolev space. There accordingly, the weak form of the fracture problem is constructed as follows:

$$\delta\Pi(\mathbf{u},\mathfrak{d},\delta\mathbf{u},\delta\mathfrak{d}) = \delta\Pi_{\text{int}}(\mathbf{u},\mathfrak{d},\delta\mathbf{u},\delta\mathfrak{d}) + \delta\Pi_{\text{ext}}(\mathbf{u},\delta\mathbf{u}) = 0. \tag{2.14}$$

The strong form of the field equations is obtained after simple algebraic manipulations:

$$\operatorname{div}\boldsymbol{\sigma} + \mathbf{f}_v = \mathbf{0} \text{ in } \mathscr{B} \text{ and } \boldsymbol{\sigma}\cdot\mathbf{n} = \bar{\mathbf{t}} \text{ on } \partial\mathscr{B}_t, \tag{2.15}$$

$$2(1-\mathfrak{d})\mathfrak{P}\mathscr{H} = \mathscr{G}_c \delta_{\mathfrak{d}} \gamma(\mathfrak{d},\nabla\mathfrak{d}) \text{ in } \mathscr{B} \text{ and } \nabla\mathfrak{d}\cdot\mathbf{n} = 0 \text{ on } \partial\mathscr{B}. \tag{2.16}$$

ÁMBITO- PREFIJO
GEISER
Nº registro
O00008744e2000024753
CSV
GEISER-aa34-5f08-a669-4b6e-9258-ed2f-d009-e7f3
DIRECCIÓN DE VALIDACIÓN
FECHA Y HORA DEL DOCUMENTO
19/06/2020 12:08:12 Horario peninsular
GEISER-aa34-5f08-a669-4b6e-9258-ed2f-d009-e7f3

Due to the regularity of the energetic functions, first-order optimal condition is sufficient to ensure stability and energy balance resulting in the following Karush-Kuhn-Tucker (KKT) conditions:

$$\dot{\mathfrak{d}} \geq 0, \tag{2.17}$$

$$2(1-\mathfrak{d})\mathfrak{P}\mathscr{H} - \mathscr{G}_c \delta_{\mathfrak{d}} \gamma(\mathfrak{d}, \nabla\mathfrak{d}) \leq 0, \tag{2.18}$$

$$\left[2(1-\mathfrak{d})\mathfrak{P}\mathscr{H} - \mathscr{G}_c \delta_{\mathfrak{d}} \gamma(\mathfrak{d}, \nabla\mathfrak{d})\right] \dot{\mathfrak{d}} = 0. \tag{2.19}$$

The weak form of the aforementioned coupled displacement-crack phase-field problem resulting from Eq.(2.14) can be subsequently discretized using FEM and linearized within the context of the incremental-iterative Newton-Raphson solution scheme.

Concerning the numerical implementation, a staggered solution scheme is adopted, see [43]. In particular the numerical implementation of the phase-field method given in [91,92] into the FE code `ABAQUS` is exploited, which combined the implementation of the user-defined capabilities `UEL` and `UMAT` for this purpose. This particular implementation endowed the separated solution of the displacement and phase-field variables, offering an amenable and robust implementation algorithm that is especially suitable for elasto-plastic fracture. Note that a detailed description of FE implementation is omitted in the sequel for the sake of brevity.

2.2.2 Constitutive Formulation for SFRPs: Invariant-Based Anisotropic Model

This section presents the elasto-plastic constitutive formulations for the analysis of SFRP composites. Note that the following derivations are constructed in the space of the effective stresses $\hat{\boldsymbol{\sigma}}$, which can be related to the Cauchy stress tensor $\boldsymbol{\sigma}$ by means of the standard relationship: $\boldsymbol{\sigma} = g(\mathfrak{d})\hat{\boldsymbol{\sigma}} = (1-\mathfrak{d})^2\hat{\boldsymbol{\sigma}}$. Inline with the investigations in [85–87, 89] assuming transversely isotropic material response, the invariant representation theory is advocated [94]. This yields to the development of the constitutive formulation through the introduction of the so-called (second-order) structural tensor $\mathbf{A}$ as above:

$$\mathbf{A} = \mathbf{a} \otimes \mathbf{a}, \tag{2.20}$$

where $\mathbf{a}$ stands for the preferential fiber orientation vector. As was described above, within the infinitesimal deformation setting, the total strain tensor $\boldsymbol{\varepsilon}$ can be additively decomposed into elastic $\boldsymbol{\varepsilon}^e$ and plastic $\boldsymbol{\varepsilon}^p$ counterparts:

$$\boldsymbol{\varepsilon} = \boldsymbol{\varepsilon}^e + \boldsymbol{\varepsilon}^p. \tag{2.21}$$

The effective Helmholtz free-energy function $\hat{\Psi}$ is expressed as:

$$\hat{\Psi}(\boldsymbol{\varepsilon}^e, \mathbf{A}) = \hat{\Psi}^e(\boldsymbol{\varepsilon}^e, \mathbf{A}) = \frac{1}{2}\boldsymbol{\varepsilon}^e : \mathbb{C}^e : \boldsymbol{\varepsilon}^e, \tag{2.22}$$

where $\mathbb{C}^e$ stands for the constitutive elastic tensor:

$$\mathbb{C}^e := \partial_{\boldsymbol{\varepsilon}^e \boldsymbol{\varepsilon}^e}\hat{\Psi} = \lambda \mathbf{1} \otimes \mathbf{1} + 2\mu_T \mathbb{I} + \alpha(\mathbf{1} \otimes \mathbf{A} + \mathbf{A} \otimes \mathbf{1}) + 2(\mu_L - \mu_T)\mathbb{I}_A + \beta \mathbf{A} \otimes \mathbf{A}, \tag{2.23}$$

Herein, $\mathbb{I}$ is the fourth-order identity matrix, $\mathbb{I}_{A,ijkl} = A_{im}\mathbb{I}_{jmkl} + A_{jm}\mathbb{I}_{mikl}$, and λ, α, β, μ_T, and μ_L correspond to the elastic constants, which are defined as follows:

$$\lambda = E_{22}\left(\nu_{23} + \nu_{31}\nu_{13}\right)/\mathfrak{D}, \tag{2.24}$$

ÁMBITO- PREFIJO
GEISER
Nº registro
O00008744e2000024753

CSV
GEISER-aa34-5f08-a669-4b6e-9258-ed2f-d009-e7f3
DIRECCIÓN DE VALIDACIÓN

FECHA Y HORA DEL DOCUMENTO
19/06/2020 12:08:12 Horario peninsular

GEISER-aa34-5f08-a669-4b6e-9258-ed2f-d009-e7f3

$$\alpha = E_{22}\left[\nu_{31}\left(1+\nu_{32}-\nu_{13}\right)-\nu_{32}\right]/\mathfrak{D}, \tag{2.25}$$

$$\beta = E_{11}\left(1-\nu_{32}\nu_{23}\right)/\mathfrak{D} - E_{22}\left[1-\nu_{21}\left(\nu_{12}+2(1+\nu_{23})\right)\right]/\mathfrak{D} - 4G_{12}, \tag{2.26}$$

$$\mu_L = G_{12} \text{ and } \mu_T = G_{23}, \tag{2.27}$$

with:

$$\mathfrak{D} = 1-\nu_{32}^2 - 2\nu_{13}\nu_{31} - 2\nu_{32}\nu_{13}\nu_{31}. \tag{2.28}$$

Note, that usually, the 1-direction corresponds to the fiber orientation, the 2-direction is the transverse in-plane orientation with respect to the fiber direction, and 3-direction stands for transverse out-of-plane orientation.

Complying with Truesdell and Noll procedure [23], the following constitutive equation is constructed:

$$\hat{\boldsymbol{\sigma}} := \partial_{\boldsymbol{\varepsilon}^e}\hat{\Psi} = \mathbb{C}^e : \boldsymbol{\varepsilon}^e, \tag{2.29}$$

and the restriction over the internal dissipation due to plasticity $\hat{\mathscr{D}}^p_{\text{int}}$ reads:

$$\hat{\mathscr{D}}^p_{\text{int}} = \hat{\boldsymbol{\sigma}} : \dot{\boldsymbol{\varepsilon}}^p \geq 0. \tag{2.30}$$

2.2.2.1 Yield Function

Advocating [85, 86], the elastic domain $\mathbb{E}$ is given by:

$$\mathbb{E} = \{(\bar{\varepsilon}^p) \mid f(\hat{\boldsymbol{\sigma}},\mathbf{A},\bar{\varepsilon}^p) \leq 0\}, \tag{2.31}$$

where $\bar{\varepsilon}^p$ corresponds to the equivalent plastic strain $\bar{\varepsilon}^p = \sqrt{\frac{2}{3}}\|\boldsymbol{\varepsilon}^p\|$.

The current pressure-dependent elasto-plastic model is equipped with a quadratic form of the yield function $\mathscr{F}(\hat{\boldsymbol{\sigma}},\mathbf{A},\bar{\varepsilon}^p)$ renders:

$$\mathscr{F}(\hat{\boldsymbol{\sigma}},\mathbf{A},\bar{\varepsilon}^p) = \zeta_1 I_1 + \zeta_2 I_2 + \zeta_3 I_3 + \zeta_4 I_3^2 + \zeta_5 I_4 + \zeta_6 I_4^2 - 1 \leq 0, \tag{2.32}$$

where I_i $(i = 1,4)$ correspond to the family of the stress invariants representing the integrity basis. These invariants are defined as:

$$I_1 = \frac{1}{2}(\mathrm{tr}[\hat{\boldsymbol{\sigma}}^{\text{pind}}])^2 - \mathrm{tr}[\mathbf{A}(\hat{\boldsymbol{\sigma}}^{\text{pind}})^2],\ I_2 = \mathrm{tr}[\mathbf{A}(\hat{\boldsymbol{\sigma}}^{\text{pind}})^2],\ I_3 = \mathrm{tr}[\hat{\boldsymbol{\sigma}}] - \mathrm{tr}[\mathbf{A}\hat{\boldsymbol{\sigma}}], \text{ and } I_4 = \frac{3}{2}\mathrm{tr}[\mathbf{A}\hat{\boldsymbol{\sigma}}^{\text{dev}}], \tag{2.33}$$

where $\hat{\boldsymbol{\sigma}}^{\text{dev}}$ is the deviatoric part of the effective stress tensor and $\hat{\boldsymbol{\sigma}}^{\text{pind}}$ is the effective-plasticity inducing stress tensor which is given by:

$$\hat{\boldsymbol{\sigma}}^{\text{pind}} = \hat{\boldsymbol{\sigma}} - \frac{1}{2}(\mathrm{tr}[\hat{\boldsymbol{\sigma}}] - \mathbf{A}\hat{\boldsymbol{\sigma}})\mathbf{1} + \frac{1}{2}(\mathrm{tr}[\hat{\boldsymbol{\sigma}}] - 3\mathbf{A}\hat{\boldsymbol{\sigma}})\mathbf{A}. \tag{2.34}$$

In Eq.(2.32), $\zeta_i(\bar{\varepsilon}^p)$ $(i = 1,6)$ stands for the corresponding yield parameters, that can represent the different loading states. Figure 2.3-left depicts an schematic 3D representation of the yield surface in the stress invariant space setting.

ÁMBITO- PREFIJO
GEISER
Nº registro
O00008744e2000024753

CSV
GEISER-aa34-5f08-a669-4b6e-9258-ed2f-d009-e7f3
DIRECCIÓN DE VALIDACIÓN

FECHA Y HORA DEL DOCUMENTO
19/06/2020 12:08:12 Horario peninsular

GEISER-aa34-5f08-a669-4b6e-9258-ed2f-d009-e7f3

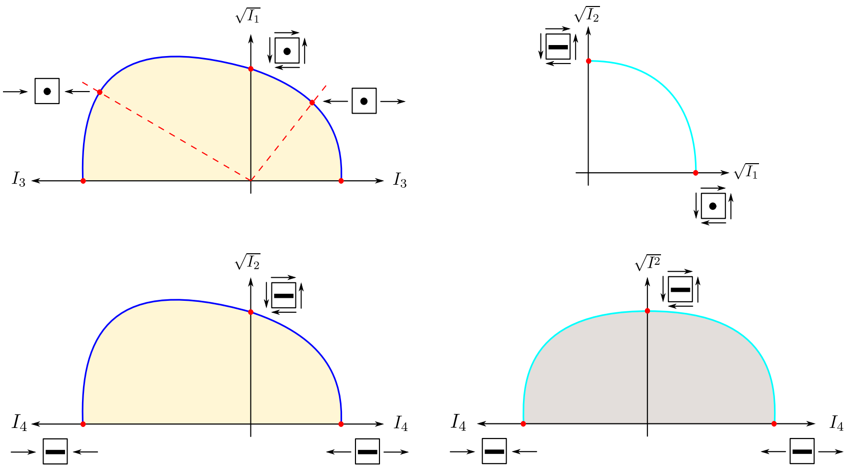

Figure 2.3 Schematic representation of the transversely isotropic yield function (left) and plastic potential (right) in the stress invariant space..

2.2.2.2 Plastic Potential Function

The current model adopts a non-associative flow rule in line with [85–87, 89], which is characterized by an invariant-based pressure-dependent quadratic transversely isotropic plastic potential function $\mathscr{M} = \mathscr{M}(\hat{\boldsymbol{\sigma}}, \mathbf{A})$, see Figure 2.3-right. This function is defined as:

$$\mathscr{M}(\hat{\boldsymbol{\sigma}}, \mathbf{A}) = \varsigma_1 I_1 + \varsigma_2 I_2 + \varsigma_3 I_3^2 + \varsigma_4 I_4^2 - 1, \tag{2.35}$$

where ς_i $(i = 1{,}4)$ denotes the plastic potential parameters.

2.2.2.3 Evolution Equations

Following standard concepts for elasto-plastic modeling, the maximum energy dissipation principle is herewith recalled in conjunction with the previous non-associative flow rule for the introduction of evolution equations for the plastic rate of deformation. These are expressed in terms of the internal variables of the model, i.e. the plastic strains $\boldsymbol{\varepsilon}^p$:

$$\dot{\boldsymbol{\varepsilon}}^p = \gamma^p \frac{\partial \mathscr{M}(\hat{\boldsymbol{\sigma}}, \mathbf{A}, \bar{\varepsilon}^p)}{\partial \hat{\boldsymbol{\sigma}}}, \tag{2.36}$$

where γ^p is the so-called plastic multiplier.

The Kuhn-Tucker (KT) loading/unloading conditions render:

$$\gamma^p \geq 0, \; \mathscr{F}(\hat{\boldsymbol{\sigma}}, \mathbf{A}, \bar{\varepsilon}^p) \leq 0, \text{ and } \gamma^p \mathscr{F}(\hat{\boldsymbol{\sigma}}, \mathbf{A}, \bar{\varepsilon}^p) = 0, \tag{2.37}$$

whilst the consistency condition is given by:

$$\gamma^p \dot{\mathscr{F}}(\hat{\boldsymbol{\sigma}}, \mathbf{A}, \bar{\varepsilon}^p) = 0. \tag{2.38}$$

The algorithmic treatment of the model is thoroughly outlined in [85–87, 95] within the context of the FEM, including a detailed description of its numerical implementation.

2.2.2.4 Failure Criterion

The last ingredient of the current model is a point-wise failure criterion at the material point level which serves as an initiation criterion for the evolution of the phase-field variable. The initiation

ÁMBITO- PREFIJO
GEISER
Nº registro
O00008744e2000024753
CSV
GEISER-aa34-5f08-a669-4b6e-9258-ed2f-d009-e7f3
DIRECCIÓN DE VALIDACIÓN
FECHA Y HORA DEL DOCUMENTO
19/06/2020 12:08:12 Horario peninsular
GEISER-aa34-5f08-a669-4b6e-9258-ed2f-d009-e7f3

criterion establishes a threshold for the activation of the phase-field cracking which is ruled by the satisfaction of Eq.(2.39). In line with the previous description, note that Eq.(2.39) implicitly defines the energy thresholds in Eq.(2.9). Herein, following [89, 96–99], an invariant-based pressure-dependent quadratic failure surface for SFRPs is adopted. The particular form of the failure criterion, $\mathscr{S}(\hat{\boldsymbol{\sigma}}, \mathbf{A})$, is given by:

$$\mathscr{S}(\hat{\boldsymbol{\sigma}}, \mathbf{A}) = \xi_1 I_1 + \xi_2 I_2 + \xi_3 I_3 + \xi_4 I_3^2 + \xi_5 I_4 + \xi_6 I_4^2 - 1 \leq 0, \tag{2.39}$$

where ξ_i, $(i = 1{,}6)$ denotes six strength parameters.

2.2.2.5 Parameter Identification

In addition to the elastic material constants, the yield function parameters ζ_i $(i = 1{,}6)$, the plastic potential parameters ς_i $(i = 1{,}4)$ and the failure surface parameters ξ_i $(i = 1{,}6)$ are to be determined in terms of experimental characterization data.

The coefficients ζ_i $(i = 1{,}6)$ are explicitly expressed as follows:

$$\zeta_1 = \frac{1}{\sigma_y^{ts2}}, \tag{2.40}$$

$$\zeta_2 = \frac{1}{\sigma_y^{is2}}, \tag{2.41}$$

$$\zeta_3 = -\frac{1}{2\sigma_y^{fc}} - \frac{1}{\sigma_y^{tc}} + \frac{1}{2\sigma_y^{ft}} + \frac{1}{\sigma_y^{tt}}, \tag{2.42}$$

$$\zeta_4 = -\frac{1}{4\sigma_y^{fc}\sigma_y^{ft}} - \frac{1}{4\sigma_y^{ts2}} + \frac{1}{\sigma_y^{tc}\sigma_y^{tt}}, \tag{2.43}$$

$$\zeta_5 = -\frac{1}{\sigma_y^{fc}} + \frac{1}{\sigma_y^{ft}}, \tag{2.44}$$

$$\zeta_6 = \frac{1}{\sigma_y^{fc}\sigma_y^{ft}}. \tag{2.45}$$

σ_y^{is}, σ_y^{ts}, σ_y^{ft}, σ_y^{fc}, σ_y^{tt}, and σ_y^{tc} denote the yield stress states obtained from in-plane shear test, transverse shear test, uniaxial longitudinal tension test, uniaxial longitudinal compression test, uniaxial transverse tension, and uniaxial transverse compression test, respectively.

To comply with the maximum dissipation principle, the convexity of the yield surface should be ensured. This imposes the following restrictions to the relations $\zeta_i(\bar{\varepsilon}^p)$ $(i = 1{,}6)$ which should hold for any $\bar{\varepsilon}^p$:

$$\sigma_y^{ft}\sigma_y^{fc}\left[4\sigma_y^{ts2} - \sigma_y^{tt}\sigma_y^{tc}\right] \geq \sigma_y^{tc}\sigma_y^{ts2}\sigma_y^{tt}. \tag{2.46}$$

The coefficients ς_i $(i = 1{,}4)$ are explicitly determined as follows:

$$\varsigma_1 = 1, \tag{2.47}$$

$$\varsigma_2 = \mu_{12}^p, \tag{2.48}$$

$$\varsigma_3 = -\frac{-1 + \nu_{12}^p + \nu_{23}^p}{4(1 + \nu_{23}^p)}, \tag{2.49}$$

ÁMBITO- PREFIJO
GEISER
Nº registro
O00008744e2000024753

CSV
GEISER-aa34-5f08-a669-4b6e-9258-ed2f-d009-e7f3
DIRECCIÓN DE VALIDACIÓN

FECHA Y HORA DEL DOCUMENTO
19/06/2020 12:08:12 Horario peninsular

GEISER-aa34-5f08-a669-4b6e-9258-ed2f-d009-e7f3

$$\varsigma_4 = \frac{\nu_{12}^p}{1+\nu_{23}^p}. \tag{2.50}$$

As can be seen from above, herein ς_1 is arbitrarily set to unity (since the size of the plastic potential has no inherent physical meaning) and ς_i $(i = 2{,}4)$ are used to enforce certain plastic Poisson's ratios $\nu_{23}^p = \varepsilon_{22}^p/\varepsilon_{33}^p$ and $\nu_{12}^p = \varepsilon_{11}^p/\varepsilon_{22}^p$, and also certain plastic distortion behavior through the relation $\mu_{12}^p = \varepsilon_{12}^p/\varepsilon_{23}^p$.

Similar to the yield function, for the plastic potential function, the following inequality in terms of the plastic Poisson's ratios must hold:

$$\mu_{12}^p \geq 0 \wedge \frac{\nu_{12}^p}{1+\nu_{23}^p} \geq 0 \wedge -\frac{-1+\nu_{12}^p+\nu_{23}^p}{4(1+\nu_{23}^p)} \geq 0. \tag{2.51}$$

The failure coefficients ξ_i $(i = 1{,}6)$ are expressed similarly to the yield function parameters ζ_i $(i = 1{,}6)$. However, the yield stresses $\sigma_y^j(\bar{\varepsilon}^p)$ are replaced by the corresponding strength values σ_s^j:

$$\xi_1 = \frac{1}{\sigma_s^{ts2}}, \tag{2.52}$$

$$\xi_2 = \frac{1}{\sigma_s^{is2}}, \tag{2.53}$$

$$\xi_3 = -\frac{1}{2\sigma_s^{fc}} - \frac{1}{\sigma_s^{tc}} + \frac{1}{2\sigma_s^{ft}} + \frac{1}{\sigma_s^{tt}}, \tag{2.54}$$

$$\xi_4 = -\frac{1}{4\sigma_s^{fc}\sigma_y^{ft}} - \frac{1}{4\sigma_s^{ts2}} + \frac{1}{\sigma_s^{tc}\sigma_s^{tt}}, \tag{2.55}$$

$$\xi_5 = -\frac{1}{\sigma_s^{fc}} + \frac{1}{\sigma_s^{ft}}, \tag{2.56}$$

$$\xi_6 = \frac{1}{\sigma_s^{fc}\sigma_s^{ft}}. \tag{2.57}$$

A detailed description of the procedure used to calibrate the model to experimental data is described in [85, 86, 89, 100] which is beyond the scope of the current investigation.

2.3 Representative Applications

The above-described formulation is implemented into the commercial FE code `ABAQUS` adopting the staggered solution scheme proposed in [43]. In this section, different numerical examples are presented showing the predictive capabilities of the proposed formulation.

2.3.1 Material Parameters

Herein, two different SFRPs sheets are considered, (1mm in thickness) PA6GF30 (Polymide 6 with 30% Glass Fiber) and (1mm in thickness) PA6GF60 (Polyamide 6 with 60% Glass Fiber), and the constitutive model is calibrated on the experimental results provided in [85–87, 89] and the references therein given. The elastic material constants of the PA6GF30 and PA6GF60 are listed in Table 2.1 and Table 2.2, respectively.

ÁMBITO- PREFIJO
GEISER
Nº registro
O00008744e2000024753
CSV
GEISER-aa34-5f08-a669-4b6e-9258-ed2f-d009-e7f3
DIRECCIÓN DE VALIDACIÓN
FECHA Y HORA DEL DOCUMENTO
19/06/2020 12:08:12 Horario peninsular
GEISER-aa34-5f08-a669-4b6e-9258-ed2f-d009-e7f3

Table 2.1 PA6GF30 (1mm in thickness): elastic properties.

E_{11} (MPa)	E_{22} (MPa)	G_{12} (MPa)	ν_{12} (minor)	ν_{23}
7893	3348	1601	0.175	0.4

Table 2.2 PA6GF60 (1mm in thickness): elastic properties.

E_{11} (MPa)	E_{22} (MPa)	G_{12} (MPa)	ν_{12} (minor)	ν_{23}
13467	5570	2520	0.12	0.4

Following the procedure presented in Section 2.2.2.5, the yield function parameters ζ_i $(i = 1,6)$ that characterize the onset of yielding are listed in Table 2.3 and Table 2.4 for PA6GF30 and PA6GF60, respectively.

Table 2.3 PA6GF30 (1mm in thickness): yielding parameters ζ_i at the onset of yielding.

ζ_1	ζ_2	ζ_3	ζ_4	ζ_5	ζ_6
0.00262532	0.00179157	−0.0097352	0.00411623	−0.0125167	0.00121853

Table 2.4 PA6GF60 (1mm in thickness): yielding parameters ζ_i at the onset of yielding.

ζ_1	ζ_2	ζ_3	ζ_4	ζ_5	ζ_6
0.00338351	0.00230897	−0.0110519	0.00530498	−0.0142096	0.00157043

The plastic potential function parameters ς_i $(i = 2,4)$ are obtained for PA6GF30 and PA6GF60 from the plastic Poisson's ratios given in Table 2.5 and Table 2.6, respectively.

Table 2.5 PA6GF30 (1mm in thickness): Plastic Poisson's ratios.

μ_{12}^p	ν_{12}^p (minor)	ν_{23}^p
1.0	0.167	0.4

Table 2.6 PA6GF60 (1mm in thickness): plastic Poisson's ratios.

μ_{12}^p	ν_{12}^p (minor)	ν_{23}^p
1.0	0.089	0.4

Furthermore, the failure criterion coefficients ξ_i $(i = 1,6)$ that define the onset of failure are listed in Table 2.7 and Table 2.8 for PA6GF30 and PA6GF60, respectively.

Table 2.7 PA6GF30 (1mm in thickness): failure parameters ξ_i at the onset of failure.

ξ_1	ξ_2	ξ_3	ξ_4	ξ_5	ξ_6
0.000232295	0.000158522	−0.00289583	0.000364213	−0.00372321	0.000107818

In addition, the fracture properties [101] and crack driving force parameters are reported in Table 2.9 and Table 2.10 for PA6GF30 and PA6GF60, respectively.

ÁMBITO- PREFIJO
GEISER
Nº registro
O00008744e2000024753

CSV
GEISER-aa34-5f08-a669-4b6e-9258-ed2f-d009-e7f3
DIRECCIÓN DE VALIDACIÓN

FECHA Y HORA DEL DOCUMENTO
19/06/2020 12:08:12 Horario peninsular

GEISER-aa34-5f08-a669-4b6e-9258-ed2f-d009-e7f3

Table 2.8 PA6GF60 (1mm in thickness): failure parameters ξ_i at the onset of failure.

ξ_1	ξ_2	ξ_3	ξ_4	ξ_5	ξ_6
0.000165166	0.000112713	-0.00244182	0.000258963	-0.00313949	0.0000766607

Table 2.9 PA6GF30 (1mm in thickness): fracture properties and phase filed parameters.

$\mathscr{G}^c$ (N/mm)	ξ^e (-)	ξ^p (-)
3.25	3.5 (assumed)	3.5 (assumed)

Table 2.10 PA6GF60 (1mm in thickness): fracture properties and phase filed parameters.

$\mathscr{G}_c$ (N/mm)	ξ^e (-)	ξ^p (-)
5.1	4.5 (assumed)	4.5 (assumed)

2.3.2 Demonstrative Examples: Validation of Implementation

Herein, a single element example is used to demonstrate the proposed formulation and to show its potential to predict the anisotropic behavior observed in SFRPs. The PA6GF30 3D brick (cube) element's side length is set to be 1mm. Four load cases are considered for which the fiber direction is taken as reference: (i) longitudinal uniaxial tension, (ii) transverse uniaxial tension, (iii) longitudinal uniaxial compression, and (iv) transverse uniaxial compression as depicted Figure 2.4. The phase-field parameter l is set to 0.215mm according to Eq.(2.3) with $\sigma_s = 112.0$ MPa. With respect to the loading, in all the four cases, the element is loaded under displacement control with constant increment $\Delta u = 0.001$mm in order to ensure the stability of the solution process.

The numerical results are depicted in Figure 2.4. In this plot, it can be observed that, throughout the first part of the evolution, i.e. before the material strength is reached, the pre-failure non-linearities are modeled assuming elasto-plastic behavior. Once the failure onset criterion is satisfied, the crack phase-field parameter starts to evolve simultaneously with the plastic deformation. The ability of the model to predict the anisotropic asymmetric behavior observed in SFRPs can clearly be seen. The simultaneous evolution of the plastic deformations and the cracking process for the case of longitudinal uniaxial tension is shown in Figure 2.5. Furthermore, a very satisfactory agreement between the experimental data (up to failure [89]) and the numerical predictions can be noticed.

The present results validate the numerical implementation proposed, capturing the non-linear material response during the different phases of the evolution and for several material directions.

2.3.3 Dog-Bone Specimen

Extending the assessment of the reliability of the current PF model, in the sequel, the 0° uniaxial quasi-static tension test along the fiber direction on a 1mm thick dog-bone specimen made of PA6GF60 is investigated. The test specimen definition in terms of geometry, FE discretization, and boundary conditions are depicted in Figure 2.6.

In total, 5000 8-node 3D linear brick elements are utilized with 4 elements across the thickness. The boundary conditions imposed are: (i) restrained displacements and rotations at the clamped edge, and (ii) constrained displacements and rotations at the mobile edge except for the displacement along the loading direction x (which is identified with the axis 1 in the corresponding graph). In order to localize the fracture, the fracture toughness value of the elements in the middle of the specimen is reduced by 5% with respect to the baseline fracture properties detailed above, see

ÁMBITO- PREFIJO
GEISER
Nº registro
O00008744e2000024753
CSV
GEISER-aa34-5f08-a669-4b6e-9258-ed2f-d009-e7f3
DIRECCIÓN DE VALIDACIÓN
FECHA Y HORA DEL DOCUMENTO
19/06/2020 12:08:12 Horario peninsular
GEISER-aa34-5f08-a669-4b6e-9258-ed2f-d009-e7f3

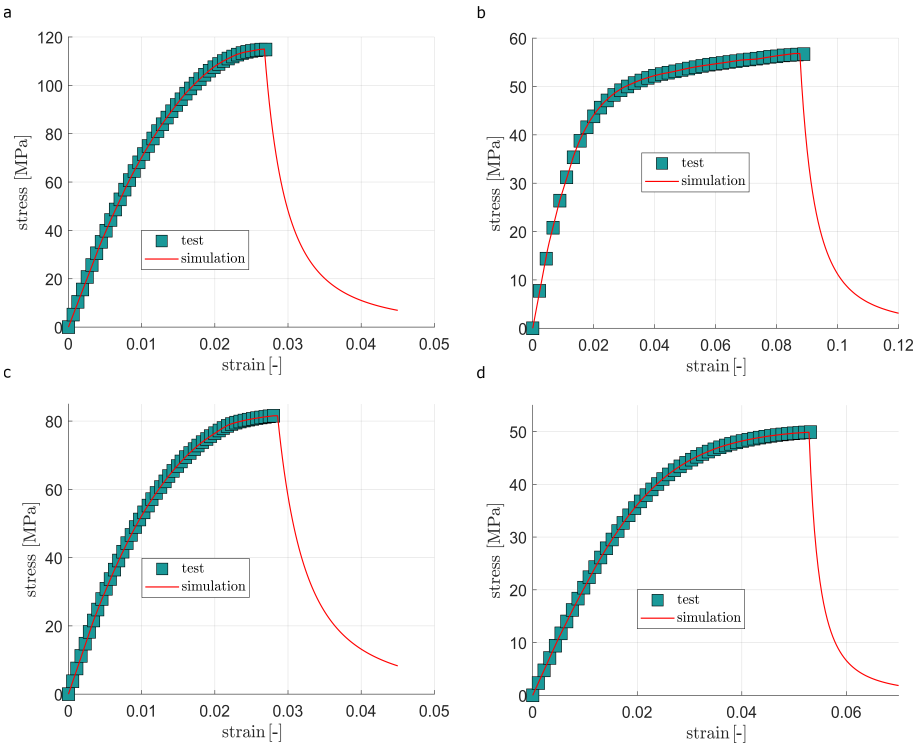

Figure 2.4 Numerical simulations vs experimental results: (a) longitudinal uniaxial tension, (b) transverse uniaxial tension, (c) longitudinal uniaxial compression, and (d) transverse uniaxial compression.

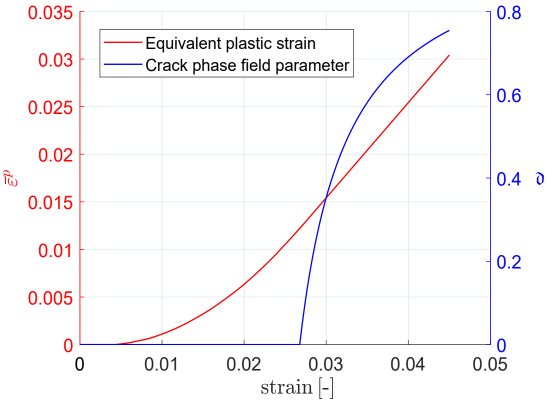

Figure 2.5 Simultaneous evolution of the plastic deformations and the cracking process: the case of longitudinal uniaxial tension.

the elements in blue in Figure 2.6. The FE discretization is refined in the middle region of the specimen where the crack is expected to grow. The phase-field parameter l is set to 0.291mm according to Eq.(2.3) with $\sigma_s = 158.0$ MPa. The specimen is loaded under displacement control

ÁMBITO- PREFIJO
GEISER
Nº registro
O00008744e2000024753
CSV
GEISER-aa34-5f08-a669-4b6e-9258-ed2f-d009-e7f3
DIRECCIÓN DE VALIDACIÓN
FECHA Y HORA DEL DOCUMENTO
19/06/2020 12:08:12 Horario peninsular
GEISER-aa34-5f08-a669-4b6e-9258-ed2f-d009-e7f3

with constant increment $\Delta u = 0.0001$mm until $u = 1.25$mm.

In Figures 2.7.a-2.7.c, the fracture process is depicted. As expected, the crack initiates and propagates in the middle of the specimen in perpendicularly to the loading direction. Figure 2.7.d shows the experimental-numerical correlation of the load-displacement response up to the failure initiation. In this graph, a good agreement between the experimental data and the numerical predictions can be observed with minor deviations in the elasto-plastic evolution prior to the damage. It is worth noting that the post-peak evolution triggering the stiffness loss was unavailable for validation purposes, but the current simulations exhibit an excellent accuracy in terms of the maximum strength value with respect to the experimental data in [89]. It is also mentionable that no remarkable difficulties in achieving equilibrium configurations were experienced noted, even when the fracture energy reduction was not considered.

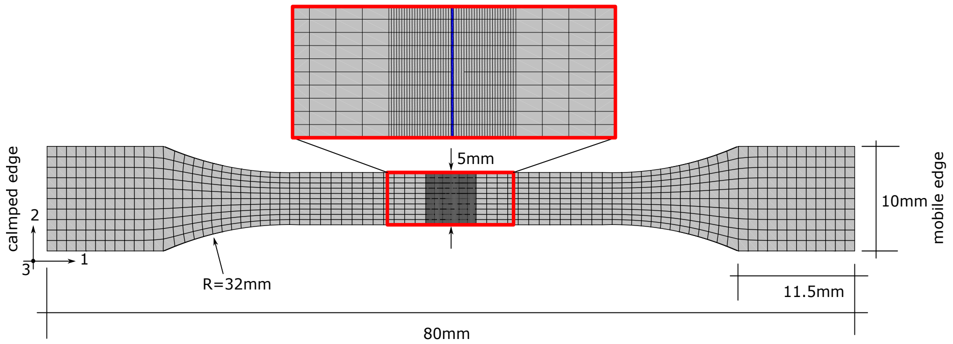

Figure 2.6 Dog-bone specimen of PA6GF60: specimen definition, FE discretization, and boundary conditions.

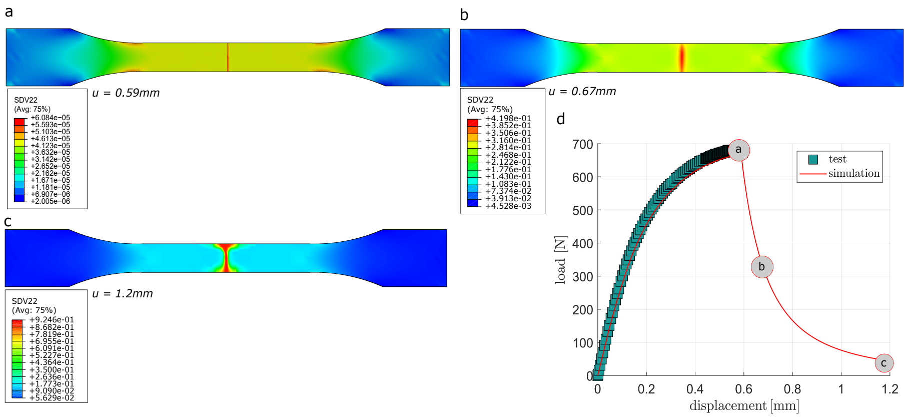

Figure 2.7 Dog-bone specimen of PA6GF60 under uniaxial tension: (a), (b), and (c) phase-field parameter (SDV22) evolution at different loading stages and (d) experimental-numerical correlation.

2.3.4 Single-Edge Notched Specimen

Herein, the failure of a 90° single-edge notched specimen made of PA6GF30 is investigated under pure tension, i.e. the loading direction is perpendicular to the internal material direction.

ÁMBITO- PREFIJO
GEISER
Nº registro
O00008744e2000024753
CSV
GEISER-aa34-5f08-a669-4b6e-9258-ed2f-d009-e7f3
DIRECCIÓN DE VALIDACIÓN
FECHA Y HORA DEL DOCUMENTO
19/06/2020 12:08:12 Horario peninsular
GEISER-aa34-5f08-a669-4b6e-9258-ed2f-d009-e7f3

Figure 2.8 details the test specimen definition in conjunction with its FE discretization details and the corresponding boundary conditions. The FE discretization is refined in the region of the specimen where the crack is expected to propagate. The phase-field length scale parameter l is set to 0.215mm according to Eq.(2.3) with $\sigma_s = 112.0$ MPa. The specimen is loaded under displacement control with maximum increment $\Delta u = 0.00005$mm.

To show the simultaneous evolution of plastic deformations and crack phase-field parameter, the crack phase-field parameter is allowed to propagate since the beginning of loading, being an interesting attribute of the current formulation. In Figures 2.9 and 2.10, the crack phase-field parameter is represented at different loading stages together with the plastic deformations which are represented by the equivalent plastic strain, respectively. As expected, the crack propagates horizontally in 90° with respect to the loading direction throughout the simulation, starting at the notch tip and propagating horizontally.

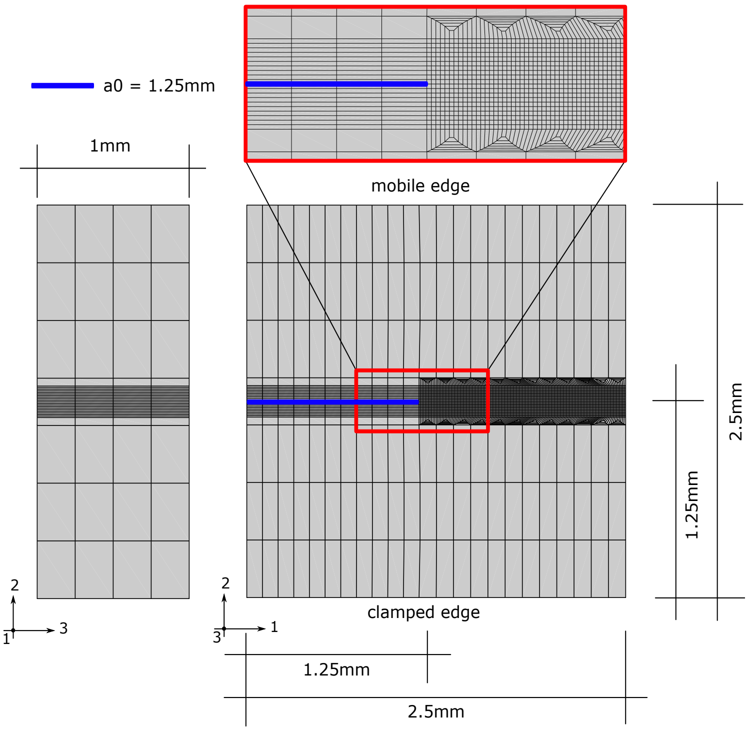

Figure 2.8 Single-edge notched specimen of PA6GF30: specimen definition, FE discretization, and boundary conditions.

2.4 Concluding Remarks

In this study, a Phase-Field (PF) model of ductile fracture for anisotropic Short Fiber Reinforced Polymers (SFRPs) within the infinitesimal deformation setting was outlined. The present formulation encompassed two main ingredients. The first salient aspect is the exploitation of the anisotropic elasto-plastic material response of SFRPs utilizing an invariant-based macroscopic approach. The second central feature is concerned with the proposed canonical formulation with an anisotropic non-associative plastic evolution model which was also equipped with a

ÁMBITO- PREFIJO
GEISER
Nº registro
O00008744e2000024753
CSV
GEISER-aa34-5f08-a669-4b6e-9258-ed2f-d009-e7f3
DIRECCIÓN DE VALIDACIÓN
FECHA Y HORA DEL DOCUMENTO
19/06/2020 12:08:12 Horario peninsular
GEISER-aa34-5f08-a669-4b6e-9258-ed2f-d009-e7f3

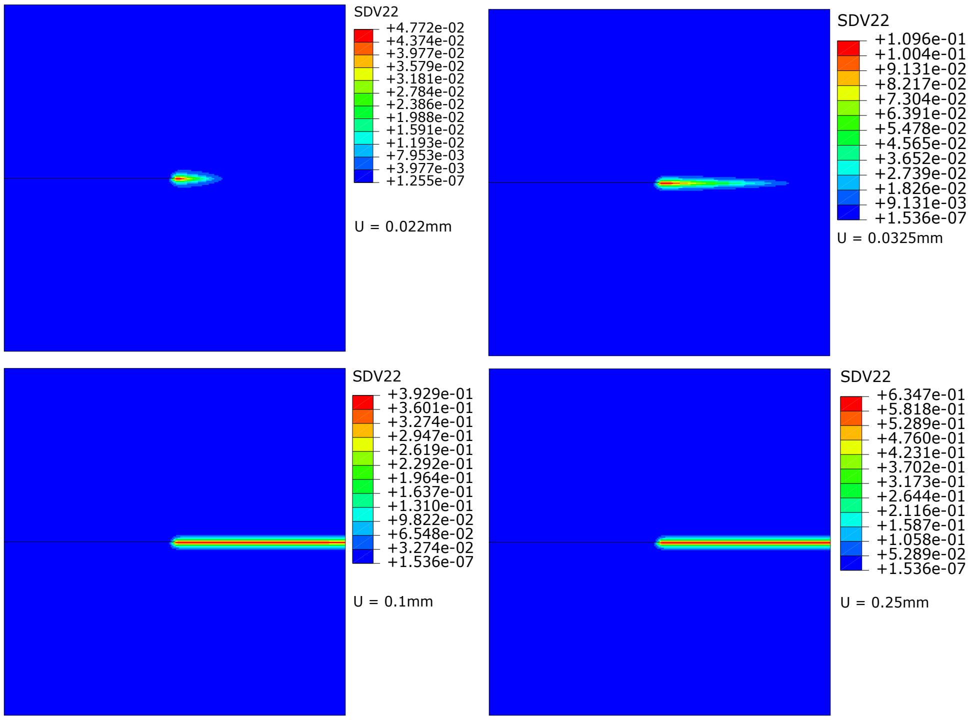

Figure 2.9 Ductile fracture of the single-edge notched specimen of PA6GF30: phase-field parameter (SDV22) evolution at different loading stages.

phenomenological damage activation criterion. This formulation fulfilled thermodynamics restrictions where two dissipative mechanisms were introduced: (i) plastic evolution and (ii) fracture phenomena.

The numerical implementation of the proposed model was carried out in the FE code `ABAQUS` following a staggered solution scheme. The performance of the model was examined through several numerical demonstrative examples and structural applications, exhibiting promising results.

ÁMBITO- PREFIJO
GEISER
Nº registro
O00008744e2000024753
CSV
GEISER-aa34-5f08-a669-4b6e-9258-ed2f-d009-e7f3
DIRECCIÓN DE VALIDACIÓN
FECHA Y HORA DEL DOCUMENTO
19/06/2020 12:08:12 Horario peninsular
GEISER-aa34-5f08-a669-4b6e-9258-ed2f-d009-e7f3

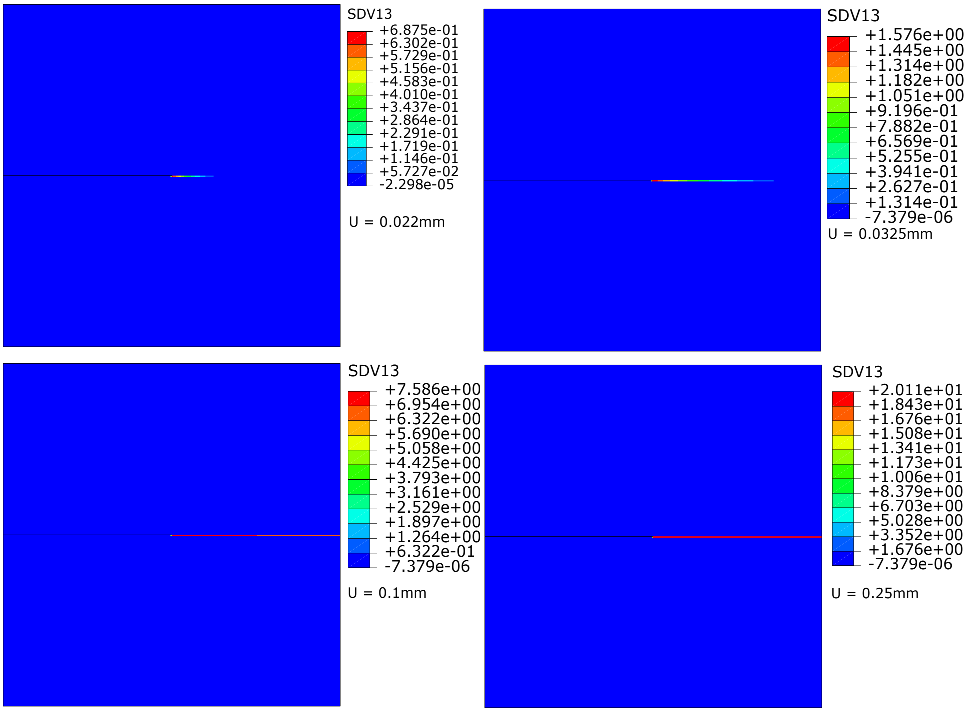

Figure 2.10 Ductile fracture of the single-edge notched specimen of PA6GF30: equivalent plastic strain (SDV13).

ÁMBITO- PREFIJO
GEISER
Nº registro
O00008744e2000024753
CSV
GEISER-aa34-5f08-a669-4b6e-9258-ed2f-d009-e7f3
DIRECCIÓN DE VALIDACIÓN
FECHA Y HORA DEL DOCUMENTO
19/06/2020 12:08:12 Horario peninsular
GEISER-aa34-5f08-a669-4b6e-9258-ed2f-d009-e7f3

ÁMBITO- PREFIJO
GEISER
Nº registro
O00008744e2000024753
CSV
GEISER-aa34-5f08-a669-4b6e-9258-ed2f-d009-e7f3
DIRECCIÓN DE VALIDACIÓN
FECHA Y HORA DEL DOCUMENTO
19/06/2020 12:08:12 Horario peninsular
GEISER-aa34-5f08-a669-4b6e-9258-ed2f-d009-e7f3

3 A Multi Phase-Field Fracture Model for Long Fiber Reinforced Polymers

This chapter presents a paper concerns with the development of a multi phase-field model based on Puck theory of failure for anisotropic fracture of long fiber reinforced polymers. The paper is published in Composite Structures, May 2020, Paper 112446.

ÁMBITO- PREFIJO
GEISER
Nº registro
O00008744e2000024753
CSV
GEISER-aa34-5f08-a669-4b6e-9258-ed2f-d009-e7f3
DIRECCIÓN DE VALIDACIÓN
FECHA Y HORA DEL DOCUMENTO
19/06/2020 12:08:12 Horario peninsular
GEISER-aa34-5f08-a669-4b6e-9258-ed2f-d009-e7f3

Abstract. Phase-Field (PF) methods of fracture have emerged as powerful modeling tools for triggering fracture events in solids. These numerical techniques efficiently alleviate mesh dependent pathologies and are very suitable for characterizing brittle as well as quasi-brittle fracture in a wide range of engineering materials including Fiber Reinforced Polymers (FRPs). In this study, a multi phase-field model relying on Puck theory of failure is proposed for triggering intra-laminar cracking in Long Fiber Reinforced Polymers (LFRPs). The current formulation encompasses the differentiation of fiber and inter-fiber (matrix-dominated) failure phenomena via the consideration of two independent phase-field crack-like variables, corresponding evolution equations, and length scales. Moreover, for matrix-dominated deformation states, the present formulations endow the incorporation of plastic effects via an invariant-based plasticity model. Special attention is also devoted to its finite element implementation, which is conducted utilizing the user-defined capabilities `UMAT` and `UEL` of the Finite Element (FE) code `ABAQUS`, in conjunction with the thorough assessment of its thermodynamics consistency. Several representative applications are presented, pinpointing the applicability and showing its robustness and reliability of the proposed computational tool.

3.1 Introduction

The comprehensive understanding of fracture events in Fiber Reinforced Polymers (FRPs) (generally encompassing carbon and glass reinforced polymeric composites, CFRP and GFRP, respectively) is a matter of significant importance in many practical applications, with a strong interest in aerospace and aeronautical industries, widening their applicability to other production sectors. However, under in-service conditions, cracking events generally lead to a drastic reduction of the load-bearing capacity of structural components and the posterior achievement of the corresponding collapsing point.

The complexity of potential failure mechanisms from different signatures in long LFRPs, i.e. inter-laminar (delamination and decohesion) and intra-laminar (fiber/matrix breakage, fiber kinking, etc.), has promoted the development of a range of different predictive models, especially within the context of the Finite Element Method (FEM). In this setting, cohesive-like models have been proven to be an efficient modeling tool for the reliable prediction of delamination events in FRPs and structures at different scales [50, 52, 102–105]. Focusing on intra-laminar failure, many of the previous works have exploited the adoption of Continuum Damage Mechanics (CDM)-based formulations in order to account for the distinction between fiber- and matrix-dominated failures relying on the consideration of different internal damage-like variables [31, 106–111], which can be also applicable to non-local formulations.

In the last decade, the landmark investigation presented in [13] and its subsequent developments in [14, 15], which is denominated as the Phase-Field (PF) approach to fracture, has emerged as a powerful strategy for modeling fracture phenomena in solids and structures via the exploitation and revitalization of Griffith's fracture approach [43, 45, 46]. PF methods are characterized by a diffusive crack representation with the prevention of any ad-hoc crack propagation criterion and precluding the implementation of complex crack tracking algorithms [112]. Many models based on the PF method have been validated against theoretical and experimental results [93, 113]. Moreover, the exploitation of these appealing attributes has led to the successful application of the PF approach to ductile fracture [37, 45, 114], fatigue, hydrogen-assisted crack failure [61], functionally graded materials, in combination with interface-like crack methods [59, 115], among many other applications.

Within the context of cracking in anisotropic solids, several attempts have been developed so far, see the use of tensor-based anisotropic formulations in anisotropic solids proposed in [39]. Further developments have also concerned the inclusion of anisotropic surface energy which enables capturing complex crack kinking phenomena [40]. One of the most prominent aspects of the intensive development of the PF method in the last decade regarded its modular format which can be applied to non-standard solids regardless of their inherent mechanical response [116, 117], which can also encompass other anisotropic inelastic effects [85–88, 118].

Focusing on modeling failure events in composite materials via PF methods, several approaches have been proposed so far. In this concern, in [64–66, 119–121] the applicability of PF crack methods to predict damage and failure of FRPs has been pinpointed. Particularly, in [65] a multi-field PF formulation that endowed the separate effect of fiber and matrix failure using two independent damage-like variables has been derived. This pioneering contribution has been subsequently revised in [66] via the introduction of a simple PF variable with the identification of the most prominent failure mechanism at the material point, which is also combined with cohesive-like crack methods in [122, 123]. Notwithstanding, there exists an increasing interest in the development of numerical predictive tools based on the PF method which allows the efficient use of phenomenological failure theories for FRPs [111]. Recalling these arguments, the present study concerns with the development of a new PF model for LFRPs via the exploitation of Puck theory of failure [124]. Following the developments presented in [66] and [65], the current investigation introduces the consideration of two independent phase-field crack variables for the distinction between fiber- and matrix-dominated failure mechanisms. Moreover, the formulation herein proposed endows the definition of two independent length scales for each phase-field variable which can be related to Puck initiation strengths. Finally, the non-linear behavior in shear-dominated response is accounted through elastic-plastic relationships between stress and strain at ply level using an anisotropic invariant-based formulation [83, 87, 125–127].

This chapter is organized as follows. The modeling framework is presented in Section 3.2, and the corresponding variational formulations are outlined in Section 3.3. Section 3.4 presents the main aspects for the FE implementation. Subsequently, the model is examined via different representative applications in Section 3.5. Conclusions of the present investigation are drawn in Section 3.6.

3.2 Multi Phase-Field Formulation Based on the Puck Theory of Failure

In this section, the fundamental aspects of the current multi phase-field formulation for modeling fracture events in long fiber reinforced composite materials are introduced. As stated above, the principal aim is the construction of a numerical formulation encompassing crack propagation in continuum anisotropic media originated from different physical failure mechanisms.

The current formulation can be derived directly from thermodynamic considerations as proposed in [43], which can be consistently equipped with the variational formalism in the spirit of the phase-field approach of fracture. In this regard, we first formulate the particular form of *total pseudo-energy density* W per unit volume for anisotropic solids accounting for different failure mechanisms (Section 3.2.1). Subsequently, the constitutive choices are addressed in sections 3.2.2 and 3.2.3.

3.2.1 Postulation of the Total Internal Energy Density

Restricting the analysis to infinitesimal strains, the point of departure of the current formulation relies on the consideration of an arbitrary body with $\mathscr{B} \in \mathbb{R}^{n_{\text{dim}}}$ (n_{dim} is the dimension of the analysis). The delimiting boundary of $\mathscr{B}$ is denoted by $\partial\mathscr{B} \in \mathbb{R}^{n_{\text{dim}}-1}$. Throughout the deformation process, the body experiences a displacement field identified by the vector field $\mathbf{u} : \mathscr{B} \to \mathbb{R}^{n_{\text{dim}}}$ at the material point level The infinitesimal strain tensor is defined as follows: $\boldsymbol{\varepsilon} := \nabla^{\text{sym}}\mathbf{u}$ with $\boldsymbol{\varepsilon} : \mathscr{B} \to \mathbb{R}^{n_{\text{dim}} \times n_{\text{dim}}}$. Prescribed displacement conditions are given by $\mathbf{u} = \overline{\mathbf{u}}$ on

$\partial\mathscr{B}_u$, whereas prescribed tractions conditions on the corresponding portion of the boundary are denoted as $\bar{\mathbf{t}} = \boldsymbol{\sigma}\cdot\mathbf{n}$ on $\partial\mathscr{B}_t$ with $\boldsymbol{\sigma}$ identifying the Cauchy stress tensor. Kinematic and static boundary conditions satisfy the standard requirements: $\overline{\partial\mathscr{B}_t \cup \partial\mathscr{B}_u} = \partial\mathscr{B}$ and $\partial\mathscr{B}_t \cap \partial\mathscr{B}_u = \emptyset$, where $\mathbf{n}$ is the external outer normal vector to the body.

In classical continuum damage mechanics (CDM), the total internal energy density is a state function of the deformation tensor $\boldsymbol{\varepsilon}$ and the internal damage-like variable $\mathfrak{d}$ [128]. This basic formulation can be extended to account for non-local effects via the incorporation of the material gradient of $\mathfrak{d}$, i.e. $\nabla\mathfrak{d}$ which allows the circumvention of the ill-posed character of the corresponding Initial Boundary Value Problem (IBVP) upon softening behavior. The consistent generalization of this isotropic damage formulation to account for different failure mechanisms can be postulated by means of recalling an additive decomposition scheme of the *total pseudo-energy density* W per unit volume, so that it becomes a state function of: (i) the strain field, (ii) the n scalar damage variables $\mathfrak{d}_i$ (with $i = 1, \ldots, n$), and (iii) their respective gradients $\nabla\mathfrak{d}_i$. Based on this decomposition scheme, each individual damage variable is associated with a particular physical failure mechanism and whose evolution is assumed to be confined between 0 (intact state) and 1 (fully broken state). Moreover, as an additional argument of the current formulation, we postulate the evolution of plastic deformation in order to accurately predict the material non-linear behavior under a matrix-dominated response.

With the previous ingredients at hand and advocating the decomposition of the Helmholtz free-energy function proposed in [129], which was successfully exploited in [111] for Puck-based damage model, it is assumed that the *total pseudo-energy density* W per unit volume for anisotropic materials can be expressed as follows:

$$W(\boldsymbol{\varepsilon},\boldsymbol{\varepsilon}^p,\hat{w}^p,\mathfrak{d}_i,\nabla\mathfrak{d}_i,\mathbf{A}) = W_{FF}(\boldsymbol{\varepsilon},\mathfrak{d}_{FF},\nabla\mathfrak{d}_{FF},\mathbf{A}) + W_{IFF}(\boldsymbol{\varepsilon},\boldsymbol{\varepsilon}^p,\hat{w}^p,\mathfrak{d}_{IFF},\nabla\mathfrak{d}_{IFF},\mathbf{A}), \quad (3.1)$$

where $W_{FF}(\boldsymbol{\varepsilon},\mathfrak{d}_{FF},\nabla\mathfrak{d}_{FF},\mathbf{A})$ and $W_{IFF}(\boldsymbol{\varepsilon},\boldsymbol{\varepsilon}^p,\hat{w}^p,\mathfrak{d}_{IFF},\nabla\mathfrak{d}_{IFF},\mathbf{A})$ correspond to the counterparts associated with the fiber and the inter-fiber failure, respectively, as addressed in Section 3.2.2. In the previous expression, $\mathbf{A} = \mathbf{a}\otimes\mathbf{a}$ identifies the so-called structural tensor with $\mathbf{a}$ refers to the material direction.

Note that in the scheme herein proposed, the dissipated energy results from the contribution of each individual failure mechanism which only affects their corresponding counterparts of the elasticity tensor. Therefore, in contrast to Bleyer and Alessi [65], the current constitutive formulation completely precludes the coupling between the different damage variables.

In the forthcoming developments, the effective Helmholtz free-energy function $\hat{\Psi}$ renders:

$$\hat{\Psi}(\boldsymbol{\varepsilon}^e,\mathbf{A}) = \frac{1}{2}\boldsymbol{\varepsilon}^e : \mathbb{C}^e : \boldsymbol{\varepsilon}^e, \quad (3.2)$$

where $\mathbb{C}^e$ is the elastic constitutive tensor:

$$\mathbb{C}^e := \partial_{\boldsymbol{\varepsilon}^e\boldsymbol{\varepsilon}^e}\hat{\Psi} = \lambda\mathbf{1}\otimes\mathbf{1} + 2\mu_T\mathbb{I} + \alpha(\mathbf{1}\otimes\mathbf{A} + \mathbf{A}\otimes\mathbf{1}) + 2(\mu_L - \mu_T)\mathbb{I}_A + \beta\mathbf{A}\otimes\mathbf{A}, \quad (3.3)$$

In the previous expression, $\mathbb{I}$ stands for the fourth-order identity matrix, $\mathbb{I}_{A,ijkl} = A_{im}\mathbb{I}_{jmkl} + A_{jm}\mathbb{I}_{mikl}$, and λ, α, β, μ_T, and μ_L are to the elastic constants:

$$\lambda = E_{22}\left(\nu_{23} + \nu_{31}\nu_{13}\right)/\mathfrak{D}, \quad (3.4)$$

$$\alpha = E_{22}\left[\nu_{31}\left(1 + \nu_{32} - \nu_{13}\right) - \nu_{32}\right]/\mathfrak{D}, \quad (3.5)$$

ÁMBITO- PREFIJO
GEISER
Nº registro
O00008744e2000024753
CSV
GEISER-aa34-5f08-a669-4b6e-9258-ed2f-d009-e7f3
DIRECCIÓN DE VALIDACIÓN
FECHA Y HORA DEL DOCUMENTO
19/06/2020 12:08:12 Horario peninsular
GEISER-aa34-5f08-a669-4b6e-9258-ed2f-d009-e7f3

$$\beta = E_{11}\left(1-\nu_{32}\nu_{23}\right)/\mathfrak{D} - E_{22}\left[1-\nu_{21}\left(\nu_{12}+2(1+\nu_{23})\right)\right]/\mathfrak{D} - 4G_{12}, \tag{3.6}$$

$$\mu_L = G_{12} \text{ and } \mu_T = G_{23}, \tag{3.7}$$

with:

$$\mathfrak{D} = 1-\nu_{32}^2 - 2\nu_{13}\nu_{31} - 2\nu_{32}\nu_{13}\nu_{31}. \tag{3.8}$$

Note that usually, 1-direction corresponds to the fiber orientation, 2-direction is transverse in-plane orientation with respect to the fiber direction, and 3-direction stands for transverse out-of-plane orientation.

The specialization of the composing terms of $W(\boldsymbol{\varepsilon},\boldsymbol{\varepsilon}^p,\hat{w}^p,\mathfrak{d}_i,\nabla\mathfrak{d}_i,\mathbf{A})$ can be established as follows. Starting the derivation with the fiber failure contribution, the corresponding counterpart is given by:

$$W_{FF}(\boldsymbol{\varepsilon},\mathfrak{d}_{FF},\nabla\mathfrak{d}_{FF},\mathbf{A}) = (1-\mathfrak{d}_{FF})^2\hat{\Psi}^e_{FF}(\boldsymbol{\varepsilon},\mathbf{A}) + W_{\text{frac},FF}(\mathfrak{d}_{FF},\nabla\mathfrak{d}_{FF}), \tag{3.9}$$

with $\hat{\Psi}^e_{FF} = \frac{1}{2}\boldsymbol{\varepsilon} : \mathbb{C}^e_{FF} : \boldsymbol{\varepsilon}$ identifying the elastic contribution associated with the fiber contribution, where:

$$\mathbb{C}^e_{FF} = \begin{bmatrix} \mathbb{C}^e_{11} & 0 & 0 & 0 & 0 & 0 \\ 0 & 0 & 0 & 0 & 0 & 0 \\ 0 & 0 & 0 & 0 & 0 & 0 \\ 0 & 0 & 0 & 0 & 0 & 0 \\ 0 & 0 & 0 & 0 & 0 & 0 \\ 0 & 0 & 0 & 0 & 0 & 0 \end{bmatrix}, \tag{3.10}$$

and $W_{\text{frac},FF}(\mathfrak{d}_{FF},\nabla\mathfrak{d}_{FF})$ stands for the inelastic fracture energy due to the fiber breakage, which adopts the form:

$$W_{\text{frac},FF}(\mathfrak{d}_{FF},\nabla\mathfrak{d}_{FF}) = \mathscr{G}_{c,FF}\left[\gamma(\mathfrak{d}_{FF},\nabla\mathfrak{d}_{FF})\right] = \mathscr{G}_{c,FF}\left[\frac{1}{2l_{FF}}\mathfrak{d}^2_{FF} + \frac{l_{FF}}{2}|\nabla\mathfrak{d}_{FF}|^2\right]. \tag{3.11}$$

In the previous expression, $\mathscr{G}_{c,FF}$ identifies as the fracture energy associated with the fiber failure, $\gamma(\mathfrak{d}_{FF},\nabla\mathfrak{d}_{FF})$ is the crack density functional of this failure mechanism, and l_{FF} is the characteristic length scale in the phase-field approach of fracture associated with fiber failure. According to [93], the length scale parameter can be related to the apparent material strength as follows:

$$l_{FF} = \frac{27}{256}\frac{E_{11}\mathscr{G}_{c,FF}}{\sigma^2_{s,FF}}, \tag{3.12}$$

where $\sigma_{s,FF}$ is the material strength associated with fiber failure.

Similarly, the inter-fiber failure contribution (also accounting for the plastic deformation) can be expressed as:

$$\begin{aligned} W_{IFF}(\boldsymbol{\varepsilon},\boldsymbol{\varepsilon}^p,\hat{w}^p,\mathfrak{d}_{IFF},\nabla\mathfrak{d}_{IFF},\mathbf{A}) = (1-\mathfrak{d}_{IFF})^2\hat{\Psi}^e_{IFF}(\boldsymbol{\varepsilon}-\boldsymbol{\varepsilon}^p,\mathbf{A}) + \Psi^p(\hat{w}^p,\mathfrak{d}_{IFF},\mathbf{A}) \\ + W_{\text{frac},IFF}(\mathfrak{d}_{IFF},\nabla\mathfrak{d}_{IFF}), \end{aligned} \tag{3.13}$$

ÁMBITO- PREFIJO
GEISER
Nº registro
O00008744e2000024753
CSV
GEISER-aa34-5f08-a669-4b6e-9258-ed2f-d009-e7f3
DIRECCIÓN DE VALIDACIÓN
FECHA Y HORA DEL DOCUMENTO
19/06/2020 12:08:12 Horario peninsular
GEISER-aa34-5f08-a669-4b6e-9258-ed2f-d009-e7f3

with $\hat{\Psi}^e_{IFF} = \frac{1}{2}\boldsymbol{\varepsilon}^e : \mathbb{C}^e_{IFF} : \boldsymbol{\varepsilon}^e$ is the elastic contribution associated with the matrix response, where:

$$\mathbb{C}^e_{IFF} = \begin{bmatrix} 0 & \mathbb{C}^e_{12} & \mathbb{C}^e_{13} & 0 & 0 & 0 \\ \mathbb{C}^e_{21} & \mathbb{C}^e_{22} & \mathbb{C}^e_{23} & 0 & 0 & 0 \\ \mathbb{C}^e_{31} & \mathbb{C}^e_{32} & \mathbb{C}^e_{33} & 0 & 0 & 0 \\ 0 & 0 & 0 & \mathbb{C}^e_{44} & 0 & 0 \\ 0 & 0 & 0 & 0 & \mathbb{C}^e_{55} & 0 \\ 0 & 0 & 0 & 0 & 0 & \mathbb{C}^e_{66} \end{bmatrix}. \tag{3.14}$$

$\Psi^p(\hat{w}^p, \mathfrak{d}_{IFF}, \mathbf{A})$ stands for energy contribution associated with plastic deformation, whose particular expression is given by:

$$\Psi^p(\hat{w}^p, \mathfrak{d}_{IFF}, \mathbf{A}) = (1 - \mathfrak{d}_{IFF})^2 \hat{w}^p(\boldsymbol{\varepsilon}^p, \mathbf{A}) \text{ with } \hat{w}^p = \int_0^t \hat{\phi}(\dot{\boldsymbol{\varepsilon}}^p, \mathbf{A})\mathrm{d}t', \tag{3.15}$$

with $\hat{\phi}(\dot{\boldsymbol{\varepsilon}}^p, \mathbf{A})$ denotes the effective plastic dissipation potential as a function of the temporal derivative of the plastic deformation for the elapsed time t throughout the deformation process. Moreover, note that without any loss of generality, we adopt the same degradation function for the elastic and plastic contributions in the part of the energy associated with inter-fiber failure.

Finally, $W_{\text{frac},IFF}(\mathfrak{d}_{IFF}, \nabla\mathfrak{d}_{IFF})$ is the dissipated energy due to matrix failure, and whose particular form is given by:

$$W_{\text{frac},IFF}(\mathfrak{d}_{IFF}, \nabla\mathfrak{d}_{IFF}) = \mathscr{G}_{c,IFF}\left[\gamma(\mathfrak{d}_{IFF}, \nabla\mathfrak{d}_{IFF})\right] = \mathscr{G}_{c,IFF}\left[\frac{1}{2l_{IFF}}\mathfrak{d}^2_{IFF} + \frac{l_{IFF}}{2}|\nabla\mathfrak{d}_{IFF}|^2\right]. \tag{3.16}$$

where $\mathscr{G}_{c,IFF}$ is the fracture energy corresponding to matrix failure, and l_{IFF} is the corresponding length scale. Similarly, the length scale parameter is estimated as:

$$l_{IFF} = \frac{27}{256}\frac{E_{22}\mathscr{G}_{c,IFF}}{\sigma^2_{s,IFF}}, \tag{3.17}$$

where $\sigma_{s,IFF}$ is the material strength associated with inter-fiber failure, i.e. matrix cracking.

Note that with the previous definitions at hand, the damaged constitutive stiffness reads:

$$\mathbb{C}(\mathfrak{d}_{FF}, \mathfrak{d}_{IFF}) = (1 - \mathfrak{d}_{FF})^2\mathbb{C}^e_{FF} + (1 - \mathfrak{d}_{IFF})^2\mathbb{C}^e_{IFF}, \tag{3.18}$$

$$\mathbb{C}(\mathfrak{d}_{FF}, \mathfrak{d}_{IFF}) = \begin{bmatrix} \mathscr{P}_1\mathbb{C}^e_{11} & \mathscr{P}_2\mathbb{C}^e_{12} & \mathscr{P}_2\mathbb{C}^e_{13} & 0 & 0 & 0 \\ \mathscr{P}_2\mathbb{C}^e_{21} & \mathscr{P}_2\mathbb{C}^e_{22} & \mathscr{P}_2\mathbb{C}^e_{23} & 0 & 0 & 0 \\ \mathscr{P}_2\mathbb{C}^e_{31} & \mathscr{P}_2\mathbb{C}^e_{32} & \mathscr{P}_2\mathbb{C}^e_{33} & 0 & 0 & 0 \\ 0 & 0 & 0 & \mathscr{P}_{12}\mathbb{C}^e_{44} & 0 & 0 \\ 0 & 0 & 0 & 0 & \mathscr{P}_{12}\mathbb{C}^e_{55} & 0 \\ 0 & 0 & 0 & 0 & 0 & \mathscr{P}_2\mathbb{C}^e_{66} \end{bmatrix}, \tag{3.19}$$

where $\mathscr{P}_1 = (1 - \mathfrak{d}_{FF})^2$, $\mathscr{P}_2 = (1 - \mathfrak{d}_{IFF})^2$, and $\mathscr{P}_{12} = \min(\mathscr{P}_1, \mathscr{P}_2)$.

As final comments, it is worth to remark that the current damage-based evolutions for fiber and inter-fiber failures recall the quadratic dissipation function within the context of the phase-field approach of fracture. Further extensions of the proposed formulation can be made using the so-called PF-CZM for homogeneous media proposed in [130], which is a matter beyond the scope of the present investigation. Also, the current formulation is equipped with two different

ÁMBITO- PREFIJO
GEISER
Nº registro
O00008744e2000024753
CSV
GEISER-aa34-5f08-a669-4b6e-9258-ed2f-d009-e7f3
DIRECCIÓN DE VALIDACIÓN
FECHA Y HORA DEL DOCUMENTO
19/06/2020 12:08:12 Horario peninsular
GEISER-aa34-5f08-a669-4b6e-9258-ed2f-d009-e7f3

length scales, l_{FF} and l_{IFF}, which are associated with different intra-laminar failure mechanisms and are linked with the respective fracture energies $\mathscr{G}_{c,FF}$ and $\mathscr{G}_{c,IFF}$. Add to that, the length scales are recalled as numerical regularizing parameters since the damage initiation is triggered upon the evaluation of the Puck failure criteria, see Section 3.2.2.

3.2.2 Phenomenological Failure Criterion: Fundamentals of the Puck Theory of Failure

The condition of damage evolution at the material point level relies on the assessment of the Puck failure criteria [124, 131], which distinguish between two main failure mechanisms: (i) fiber failure and (ii) inter-fiber failure (matrix-dominated cracking). The ply coordinates are expressed in the local setting $0-\mathbf{e}_1-\mathbf{e}_2-\mathbf{e}_3$, see Figure 3.1.a. As customary, the fiber direction corresponds to the symbol $\parallel$ (subscript 1), whilst the directions transverse to the fiber direction in-plane (subscript 2) and out-of-plane (subscript 3) are denoted by the symbol $\perp$.

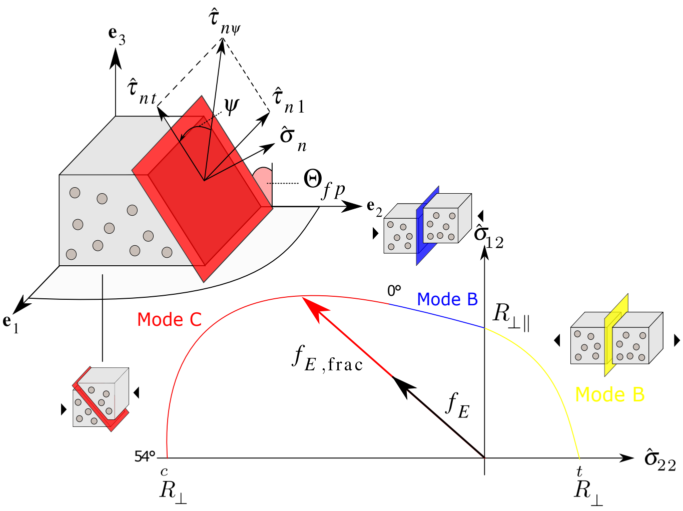

Figure 3.1 Puck failure theory: Illustration of the different inter-fiber failure (IFF) modes according to the 3D Puck criterion [131].

According to Puck theory, fiber failure is attained through the violation of the corresponding failure criterion in tension and compressions.

In this setting, for each of the identified failure mechanisms, fracture can be triggered by the evaluation of the corresponding failure exposure factors (material efforts) that relate the length of a pseudo vector $\boldsymbol{\varpi}$ and that corresponding to the fracture vector $\boldsymbol{\varpi}_{\mathrm{frac}}$, i.e. $f_E = |\boldsymbol{\varpi}|/|\boldsymbol{\varpi}_{\mathrm{frac}}|$, see [131]. Therefore, failure is initiated when the exposure factor f_E reaches 1, whereas subsequent failure progression relies on energetic considerations inline with standard PF methods of fracture.

The exposure factor for fiber failure under tensile stress conditions, which is denoted by the subscript $FF+$, is given by:

$$f_{E,FF+} = \frac{1}{R^t_{\parallel}}\left[\hat{\sigma}_{11} - \left(\nu_{\perp\parallel} - \frac{E_{\parallel}}{E_{\parallel f}}\nu_{\perp\parallel f}\right)(\hat{\sigma}_{22}+\hat{\sigma}_{33})\,\mathscr{P}_2\right], \tag{3.20}$$

where $R^t_{\parallel}$ stands for the tensile longitudinal strength in fiber direction. $\nu_{\perp\parallel}$ and $\nu_{\perp\parallel f}$ identify the major Poisson's ratios of the ply and the fibers, respectively, and $E_{\parallel f}$ is the elastic modulus of the fibers.

ÁMBITO- PREFIJO
GEISER
Nº registro
O00008744e2000024753
CSV
GEISER-aa34-5f08-a669-4b6e-9258-ed2f-d009-e7f3
DIRECCIÓN DE VALIDACIÓN
FECHA Y HORA DEL DOCUMENTO
19/06/2020 12:08:12 Horario peninsular
GEISER-aa34-5f08-a669-4b6e-9258-ed2f-d009-e7f3

The exposure factor for fiber failure in compression reads:

$$f_{E,FF-} = \sqrt{\left(\frac{1}{R^c_\parallel}\left[\hat{\sigma}_{11} - \left(\nu_{\perp\parallel} - \frac{E_\parallel}{E_{\parallel f}}\nu_{\perp\parallel f}m_{\sigma f}\right)\mathscr{P}_2\left(\hat{\sigma}_{22}+\hat{\sigma}_{33}\right)\right]\right)^2 + \kappa\left(\frac{\hat{\sigma}^2_{12}+\hat{\sigma}^2_{13}}{R^2_{\perp\parallel}}\right)}, \tag{3.21}$$

where $R^c_\parallel$ is the compressive longitudinal strength in fiber direction, $R_{\perp\parallel}$ represents the in-plane shear strength, and $m_{\sigma f}$ stands for the so-called magnification factor, which is assumed to take the values 1.1 for CFRP and 1.3 for GFRP [131]. The incorporation of $\mathscr{P}_2$ is to scale the influence of the transverse stress components on the longitudinal stress (lateral contraction) with respect to the state of matrix damage. It is assumed that the contraction in the longitudinal direction due to transverse stress will vanish in a case $\mathscr{P}_2 \to 1$, i.e. matrix rupture parallel to the fibers. In the case of compressive longitudinal stress, reduced compressive longitudinal fracture resistance of the plies is assumed in case of increasing shear stress, see [132–136]. The parameter κ allows controlling the influence of shear stresses on the failure of the fibers under compression. In the case of lateral constraint $\kappa = 0$, because even in case of a crushed matrix the fibers are assumed to be kept inline by the lateral constraint. In case of absent lateral constrains $\kappa \geq 0$, since a crushed matrix will promote fiber kinking and will, therefore, reduce the compressive load capacities in fiber direction [132–136].

With regard to the inter-fiber failure, Puck theory introduced the concept of the so-called fracture plane [124, 131], and hence the inter-fiber failure criterion is based on the identification of the fracture angle Θ_{fp} and fracture plane with the highest exposure factor $F_{E,IFF}$. The determination of the fracture plane is usually performed via the assessment of the most critical stress state in terms of the local components by calculating the value of $F_{E,IFF}$ for all angles Θ within the interval of $-90^\circ \leq \Theta \leq +90^\circ$, using an increment of one degree. The transformation from the local ply setting to the action plane system yields:

$$\begin{bmatrix}\hat{\sigma}_n(\Theta)\\ \hat{\tau}_{nt}(\Theta)\\ \hat{\tau}_{n1}(\Theta)\end{bmatrix} = \begin{bmatrix}\cos^2\Theta & \sin^2\Theta & 2\cos\Theta\sin\Theta & 0 & 0\\ -\cos\Theta\sin\Theta & \cos\Theta\sin\Theta & \cos^2\Theta-\sin^2\Theta & 0 & 0\\ 0 & 0 & 0 & \sin\Theta & \cos\Theta\end{bmatrix}\begin{bmatrix}\hat{\sigma}_{22}\\ \hat{\sigma}_{33}\\ \hat{\sigma}_{23}\\ \hat{\sigma}_{13}\\ \hat{\sigma}_{12}\end{bmatrix}. \tag{3.22}$$

The particular expressions for inter-fiber failure under tensile and compressive loading conditions on the action plane are given by the following, respectively:

$$f_{E,IFF+}(\Theta) = \left[\sqrt{\left[\left(\frac{1}{R^{At}_\perp} - \frac{p^t_{\perp\psi}}{R^A_{\perp\psi}}\right)\hat{\sigma}_n(\Theta)\right]^2 + \left(\frac{\hat{\tau}_{nt}(\Theta)}{R^A_{\perp\perp}}\right)^2 + \left(\frac{\hat{\tau}_{n1}(\Theta)}{R^A_{\parallel\perp}}\right)^2} + \frac{p^t_{\perp\psi}}{R^A_{\perp\psi}}\hat{\sigma}_n(\Theta)\right] \frac{1}{\eta_w} \text{ for } \hat{\sigma}_n(\Theta) \geq 0, \tag{3.23}$$

ÁMBITO- PREFIJO
GEISER
Nº registro
O00008744e2000024753

CSV
GEISER-aa34-5f08-a669-4b6e-9258-ed2f-d009-e7f3
DIRECCIÓN DE VALIDACIÓN

FECHA Y HORA DEL DOCUMENTO
19/06/2020 12:08:12 Horario peninsular

GEISER-aa34-5f08-a669-4b6e-9258-ed2f-d009-e7f3

$$f_{E,IFF-}(\Theta) = \left[\sqrt{\left(\frac{p^{c}_{\perp\psi}}{R^{A}_{\perp\psi}}\hat{\sigma}_n(\Theta)\right)^2 + \left(\frac{\hat{\tau}_{nt}(\Theta)}{R^{A}_{\perp\perp}}\right)^2 + \left(\frac{\hat{\tau}_{n1}(\Theta)}{R^{A}_{\parallel\perp}}\right)^2} + \frac{p^{c}_{\perp\psi}}{R^{A}_{\perp\psi}}\hat{\sigma}_n(\Theta)\right] \quad (3.24)$$

$$\frac{1}{\eta_w} \text{ for } \hat{\sigma}_n(\Theta) < 0.$$

In the previous expressions, η_w accounts for the influence of the exposure factor in fiber direction on the inter-fiber failure due to lateral contraction, as long as no fiber failure occurred [132,134]. Moreover, one can identify $R^{At}_{\perp} = R^{t}_{\perp}$, $R^{A}_{\perp\parallel} = R_{\perp\parallel}$, where $R^{t}_{\perp}$ represents the transverse tensile strength. Also, the fracture strength $R^{A}_{\perp\perp}$ is given by:

$$R^{A}_{\perp\perp} = \frac{R^{c}_{\perp}}{2\left(1+p^{c}_{\perp\perp}\right)}, \quad (3.25)$$

where $R^{c}_{\perp}$ represents the transverse compressive strength of the ply. The definitions of the inclination parameters $p^{t}_{\perp\psi}$ and $p^{c}_{\perp\psi}$ at any angle ψ are given by the following relations, respectively:

$$\frac{p^{t}_{\perp\psi}}{R^{A}_{\perp\psi}} = \frac{p^{t}_{\perp\perp}}{R^{A}_{\perp\perp}}\cos^2\psi + \frac{p^{t}_{\perp\parallel}}{R^{A}_{\perp\parallel}}\sin^2\psi \text{ and } \frac{p^{c}_{\perp\psi}}{R^{A}_{\perp\psi}} = \frac{p^{c}_{\perp\perp}}{R^{A}_{\perp\perp}}\cos^2\psi + \frac{p^{c}\perp\parallel}{R^{A}_{\perp\parallel}}\sin^2\psi, \quad (3.26)$$

with:

$$R^{A}_{\perp\psi} = \left[\left(\frac{\cos\psi}{R^{A}_{\perp\perp}}\right)^2 + \left(\frac{\sin\psi}{R^{A}_{\perp\parallel}}\right)^2\right]. \quad (3.27)$$

The trigonometric terms defined as:

$$\cos^2\psi = \frac{\hat{\tau}^2_{nt}}{\hat{\tau}^2_{nt} + \hat{\tau}^2_{n1}} \text{ and } \sin^2\psi = \frac{\hat{\tau}^2_{n1}}{\hat{\tau}^2_{nt} + \hat{\tau}^2_{n1}}. \quad (3.28)$$

Finally, recommended values of material-dependent inclination parameters $p^{t}_{\perp\perp}$, $p^{c}_{\perp\perp}$, $p^{t}_{\perp\parallel}$, and $p^{c}_{\perp\parallel}$ are reported in Table 3.1 for glass fiber reinforced (GFRP) and carbon fiber reinforced (CFRP) composites.

Table 3.1 Recommended inclination factors for CFRP and GFRP composites.

Material	$p^{t}_{\perp\perp}$	$p^{c}_{\perp\perp}$	$p^{t}_{\perp\parallel}$	$p^{c}_{\perp\parallel}$
GFRP	0.30	0.25	0.20	0.25
CFRP	0.35	0.30	0.25	0.30

3.2.3 Plasticity Formulation for Matrix-Dominated Response

The present section introduces an anisotropic plasticity model for the characterization of matrix-dominated response in long fiber reinforced composites [85–87]. Via standard plasticity arguments, the total strain tensor $\boldsymbol{\varepsilon}$ can be additively decomposed into elastic $\boldsymbol{\varepsilon}^{e}$ and plastic $\boldsymbol{\varepsilon}^{p}$ counterparts:

$$\boldsymbol{\varepsilon} = \boldsymbol{\varepsilon}^{e} + \boldsymbol{\varepsilon}^{p}. \quad (3.29)$$

ÁMBITO- PREFIJO
GEISER
Nº registro
O00008744e2000024753
CSV
GEISER-aa34-5f08-a669-4b6e-9258-ed2f-d009-e7f3
DIRECCIÓN DE VALIDACIÓN
FECHA Y HORA DEL DOCUMENTO
19/06/2020 12:08:12 Horario peninsular
GEISER-aa34-5f08-a669-4b6e-9258-ed2f-d009-e7f3

Recalling the definition of the effective Helmholtz free-energy function $\hat{\Psi}(\boldsymbol{\varepsilon}^e,\mathbf{A})$ in Eq.(3.2) and complying with Truesdell and Noll procedure [23], the following constitutive equation is constructed:

$$\hat{\boldsymbol{\sigma}} := \partial_{\boldsymbol{\varepsilon}^e}\hat{\Psi} = \mathbb{C}^e : \boldsymbol{\varepsilon}^e, \tag{3.30}$$

and the restriction over the internal dissipation due to plasticity $\hat{\mathscr{D}}^p_{\text{int}}$ reads:

$$\hat{\mathscr{D}}^p_{\text{int}} = \hat{\boldsymbol{\sigma}} : \dot{\boldsymbol{\varepsilon}}^p \geq 0. \tag{3.31}$$

Correspondingly, the elastic domain $\mathbb{E}$ can be expressed as:

$$\mathbb{E} = \{(\bar{\varepsilon}^p) \mid f(\hat{\boldsymbol{\sigma}},\mathbf{A},\bar{\varepsilon}^p) \leq 0\}, \tag{3.32}$$

where $\bar{\varepsilon}^p$ is the equivalent plastic strain $\bar{\varepsilon}^p = \sqrt{\frac{1}{2}}\|\boldsymbol{\varepsilon}^p\|$. The particular form of the yield function $\mathscr{F}(\hat{\boldsymbol{\sigma}},\mathbf{A},\bar{\varepsilon}^p)$ is given by:

$$\mathscr{F}(\hat{\boldsymbol{\sigma}},\mathbf{A},\bar{\varepsilon}^p) = \zeta_1 I_1 + \zeta_2 I_2 + \zeta_3 I_3 + \zeta_4 I_3^2 - 1 \leq 0, \tag{3.33}$$

where I_i $(i = 1{,}3)$ represents the stress invariants which its expressions are omitted here for the sake of brevity, see [85, 86] for further details.

In Eq.(3.33), the yielding parameters are identified by: $\zeta_i(\bar{\varepsilon}^p)$ $(i = 1{,}4)$ which represent different loading states and can be characterized via experimental procedures.

The adoption of a pressure-dependent response is retrieved through the use of a non-associative flow rule inline with [85–87]. This plastic response is characterized by an invariant-based pressure-dependent quadratic transversely isotropic plastic potential function $\mathscr{M}(\hat{\boldsymbol{\sigma}},\mathbf{A})$ which is defined as follows:

$$\mathscr{M}(\hat{\boldsymbol{\sigma}},\mathbf{A}) = \varsigma_1 I_1 + \varsigma_2 I_2 + \varsigma_3 I_3^2 - 1, \tag{3.34}$$

where ς_i $(i = 1{,}3)$ denote the plastic potential parameters.

Finally, the maximum energy dissipation principle is exploited for the definition of the evolution equations for the plastic rate of deformation. Such evolution equations are expressed in terms of the internal variables of the model as follows:

$$\dot{\boldsymbol{\varepsilon}}^p = \gamma^p \frac{\partial \mathscr{M}(\hat{\boldsymbol{\sigma}},\mathbf{A})}{\partial \hat{\boldsymbol{\sigma}}}, \tag{3.35}$$

where γ^p is the so-called plastic multiplier.

With these derivations at hand, the Kuhn-Tucker (KT) loading/unloading conditions can be expressed as:

$$\gamma^p \geq 0,\ \mathscr{F}(\hat{\boldsymbol{\sigma}},\mathbf{A},\bar{\varepsilon}^p) \leq 0,\ \text{and}\ \gamma^p \mathscr{F}(\hat{\boldsymbol{\sigma}},\mathbf{A},\bar{\varepsilon}^p) = 0, \tag{3.36}$$

whilst the consistency condition reads:

$$\gamma^p \dot{\mathscr{F}}(\hat{\boldsymbol{\sigma}},\mathbf{A},\bar{\varepsilon}^p) = 0. \tag{3.37}$$

ÁMBITO- PREFIJO
GEISER
Nº registro
O00008744e2000024753
CSV
GEISER-aa34-5f08-a669-4b6e-9258-ed2f-d009-e7f3
DIRECCIÓN DE VALIDACIÓN
FECHA Y HORA DEL DOCUMENTO
19/06/2020 12:08:12 Horario peninsular
GEISER-aa34-5f08-a669-4b6e-9258-ed2f-d009-e7f3

3.3 Variational Formulation and Thermodynamics Aspects

In the sequel, the variational formulation of the present model is derived, see [137] for more comprehensive details. The total energy functional of the body, $\Pi(\mathbf{u},\mathfrak{d}_i)$ at an arbitrary instant t, can be formulated as:

$$\Pi(\mathbf{u},\mathfrak{d}_i) = \Pi_{\text{int}}(\mathbf{u},\mathfrak{d}_i) + \Pi_{\text{ext}}(\mathbf{u}), \tag{3.38}$$

where $\Pi_{\text{int}}(\mathbf{u},\mathfrak{d}_i)$ and $\Pi_{\text{ext}}(\mathbf{u})$ are the internal and external contribution to the energy functional, respectively:

$$\Pi_{\text{int}}(\mathbf{u},\mathfrak{d}_i) = \int_{\mathscr{B}} W(\boldsymbol{\varepsilon},\boldsymbol{\varepsilon}^p,\hat{w}^p,\mathfrak{d}_i,\nabla\mathfrak{d}_i,\mathbf{A})\mathrm{d}\Omega = \Pi_{\text{int},FF}(\mathbf{u},\mathfrak{d}_{FF}) + \Pi_{\text{int},IFF}(\mathbf{u},\mathfrak{d}_{IFF}), \tag{3.39}$$

$$\Pi_{\text{ext}}(\mathbf{u}) = -\int_{\mathscr{B}} \mathbf{f}_v \mathrm{d}\Omega - \int_{\partial\mathscr{B}_t} \bar{\mathbf{t}}\mathrm{d}\partial\Omega, \tag{3.40}$$

where $\mathbf{f}_v$ is the deformation-independent volume-specific loads and:

$$\begin{aligned}\Pi_{\text{int},FF}(\mathbf{u},\mathfrak{d}_{FF}) &= \int_{\mathscr{B}} W_{FF}(\boldsymbol{\varepsilon},\mathfrak{d}_{FF},\nabla\mathfrak{d}_{FF},\mathbf{A})\mathrm{d}\Omega \\ &= \int_{\mathscr{B}} (1-\mathfrak{d}_{FF})^2\hat{\Psi}^e_{FF}(\boldsymbol{\varepsilon},\mathbf{A})\mathrm{d}\Omega + \int_{\mathscr{B}} \mathscr{G}_{c,FF}\left[\frac{1}{2l_{FF}}\mathfrak{d}^2_{FF} + \frac{l_{FF}}{2}|\nabla\mathfrak{d}_{FF}|^2\right]\mathrm{d}\Omega,\end{aligned} \tag{3.41}$$

$$\begin{aligned}\Pi_{\text{int},IFF}(\mathbf{u},\mathfrak{d}_{IFF}) &= \int_{\mathscr{B}} W_{IFF}(\boldsymbol{\varepsilon}-\boldsymbol{\varepsilon}^p,\mathfrak{d}_{IFF},\nabla\mathfrak{d}_{IFF},\mathbf{A})\mathrm{d}\Omega \\ &= \int_{\mathscr{B}} (1-\mathfrak{d}_{IFF})^2\hat{\Psi}^e_{IFF}(\boldsymbol{\varepsilon}-\boldsymbol{\varepsilon}^p,\mathbf{A})\mathrm{d}\Omega + \int_{\mathscr{B}} \Psi^p(\hat{w}^p,\mathfrak{d}_{IFF})\mathrm{d}\Omega \\ &+ \int_{\mathscr{B}} \mathscr{G}_{c,IFF}\left[\frac{1}{2l_{IFF}}\mathfrak{d}^2_{IFF} + \frac{l_{IFF}}{2}|\nabla\mathfrak{d}_{IFF}|^2\right]\mathrm{d}\Omega.\end{aligned} \tag{3.42}$$

Recalling the standard Bubnov-Galerkin method, the three primary fields with:

$$\mathbf{u} \in \mathscr{U}_u := \left\{\mathbf{u} \in H^1(\mathscr{B}) | \nabla\mathbf{u} \in L^2(\mathscr{B});\ \mathbf{u} = \bar{\mathbf{u}} \text{ on } \partial\mathscr{B}_u\right\},$$

$$\mathfrak{d}_{FF} \in \mathscr{U}_{\mathfrak{d}_{FF}} := \left\{\mathfrak{d}_{FF} \in H^1(\mathscr{B}) | \mathfrak{d}_{FF}(\mathbf{x}) \in [0,1],\ \dot{\mathfrak{d}}_{FF} \geq 0,\ \forall\mathbf{x} \in \mathscr{B}\right\},$$

$$\mathfrak{d}_{IFF} \in \mathscr{U}_{\mathfrak{d}_{IFF}} := \left\{\mathfrak{d}_{IFF} \in H^1(\mathscr{B}) | \mathfrak{d}_{IFF}(\mathbf{x}) \in [0,1],\ \dot{\mathfrak{d}}_{IFF} \geq 0,\ \forall\mathbf{x} \in \mathscr{B}\right\},$$

are extended by the corresponding test functions:

$$\delta\mathbf{u} \in \mathscr{V}_u := \left\{\delta\mathbf{u} \in H^1(\mathscr{B}) | \nabla\delta\mathbf{u} \in L^2(\mathscr{B});\ \delta\mathbf{u} = \mathbf{0} \text{ on } \partial\mathscr{B}_u\right\},$$

$$\delta\mathfrak{d}_{FF} \in \mathscr{V}_{\mathfrak{d}_{FF}} := \left\{\delta\mathfrak{d} \in H^1(\mathscr{B}) | \delta\mathfrak{d}_{FF} \geq 0,\ \forall\mathbf{x} \in \mathscr{B}\right\},$$

$$\delta\mathfrak{d}_{IFF} \in \mathscr{V}_{\mathfrak{d}_{IFF}} := \left\{\delta\mathfrak{d} \in H^1(\mathscr{B}) | \delta\mathfrak{d}_{IFF} \geq 0,\ \forall\mathbf{x} \in \mathscr{B}\right\},$$

ÁMBITO- PREFIJO
GEISER
Nº registro
O00008744e2000024753

CSV
GEISER-aa34-5f08-a669-4b6e-9258-ed2f-d009-e7f3
DIRECCIÓN DE VALIDACIÓN

FECHA Y HORA DEL DOCUMENTO
19/06/2020 12:08:12 Horario peninsular

GEISER-aa34-5f08-a669-4b6e-9258-ed2f-d009-e7f3

where H^1 denotes the Sobolev space. There accordingly, the weak form of the coupled displacement-crack phase-field problem is constructed as:

$$\delta\Pi(\mathbf{u},\mathfrak{d}_i,\delta\mathbf{u},\delta\mathfrak{d}_i) = \delta\Pi_{\text{int}}(\mathbf{u},\mathfrak{d}_i,\delta\mathbf{u},\delta\mathfrak{d}_i) + \delta\Pi_{\text{ext}}(\mathbf{u},\delta\mathbf{u}) = 0. \tag{3.43}$$

After simple algebraic manipulations, the strong form of the field equations can be obtained:

$$\text{div}\boldsymbol{\sigma} + \mathbf{f}_v = \mathbf{0} \text{ in } \mathscr{B} \text{ and } \boldsymbol{\sigma}\cdot\mathbf{n} = \bar{\mathbf{t}} \text{ on } \partial\mathscr{B}_t, \tag{3.44}$$

$$2(1-\mathfrak{d}_{FF})\mathfrak{P}_{FF}\mathscr{H}_{FF} = \mathscr{G}_{c,FF}\delta_{\mathfrak{d}_{FF}}\gamma(\mathfrak{d}_{FF},\nabla\mathfrak{d}_{FF}) \text{ in } \mathscr{B} \text{ and } \nabla\mathfrak{d}_{FF}\cdot\mathbf{n} = 0 \text{ on } \partial\mathscr{B}, \tag{3.45}$$

$$2(1-\mathfrak{d}_{IFF})\mathfrak{P}_{IFF}\mathscr{H}_{IFF} = \mathscr{G}_{c,IFF}\delta_{\mathfrak{d}_{IFF}}\gamma(\mathfrak{d}_{IFF},\nabla\mathfrak{d}_{IFF}) \text{ in } \mathscr{B} \text{ and } \nabla\mathfrak{d}_{IFF}\cdot\mathbf{n} = 0 \text{ on } \partial\mathscr{B}. \tag{3.46}$$

In the previous expressions, div[•] is the divergence operator. The Cauchy stress tensor $\boldsymbol{\sigma}$ can be expressed in terms of the effective stress tensor $\hat{\boldsymbol{\sigma}}$ via: $\boldsymbol{\sigma} = (1-\mathfrak{d}_{FF})^2\hat{\boldsymbol{\sigma}}_{FF} + (1-\mathfrak{d}_{IFF})^2\hat{\boldsymbol{\sigma}}_{IFF}$ with $\hat{\boldsymbol{\sigma}}_{FF} = \mathbb{C}^e_{FF} : \boldsymbol{\varepsilon}$ and $\hat{\boldsymbol{\sigma}}_{IFF} = \mathbb{C}^e_{IFF} : \boldsymbol{\varepsilon}^e$.

With respect to the crack driving forces defined in Eqs.(3.45) and (3.46), it is worth mentioning that fiber failure only attains elastic deformation, whereas inter-fiber failure is characterized by the evolution of plastic and elastic strains. Here, $\mathfrak{P}_{FF}$ and $\mathfrak{P}_{IFF}$ are activation flags for the current crack driving forces for fiber and inter-fiber failure, respectively, and are activated if and only if their respective Puck failure criterion has been met. Accordingly, for fiber failure one can define:

$$\mathscr{H}_{FF} = \xi^e_{FF}\left[\langle\frac{\max\limits_{\tau\in[0,t]}\hat{\Psi}^e_{FF}(\tau)}{\hat{\Psi}^e_{\text{init},FF}} - 1\rangle_+\right], \tag{3.47}$$

whereas for inter-fiber failure we adopt the crack driving force proposed in [137]:

$$\mathscr{H}_{IFF} = \xi^e_{IFF}\left[\langle\frac{\max\limits_{\tau\in[0,t]}\hat{\Psi}^e_{IFF}(\tau)}{\hat{\Psi}^e_{\text{init},IFF}} - 1\rangle_+\right] + \xi^p\left[\langle\frac{\hat{\Psi}^p}{\hat{\Psi}^p_{\text{init}}} - 1\rangle_+\right], \tag{3.48}$$

It is worth mentioning that both $\mathscr{H}_{FF}$ and $\mathscr{H}_{IFF}$ ensure the positive evolution of the respective phase-field variables, i.e. $\dot{\mathfrak{d}}_{FF} \geq 0$ and $\dot{\mathfrak{d}}_{IFF} \geq 0$. Moreover, $\hat{\Psi}^e_{FF}$ is the maximum reached effective elastic energy for fiber failure and ξ^e_{FF} is a dimensionless parameter that characterizes the activation of fracture due to the elastic contribution but also governs the post-peak behavior for inter-fiber failure. Similarly, $\hat{\Psi}^e_{IFF}$ is the maximum ever reached effective elastic energy for inter-fiber failure, $\hat{\Psi}^e_{\text{init},IFF}$ is the effective elastic energy for fracture initiation for inter-fiber failure, and ξ^e_{IFF} is a dimensionless parameter associated with the activation of fracture due to the elastic contribution, $\hat{\Psi}^p$ stands for the effective plastic energy, $\hat{\Psi}^p_{\text{init}}$ is the effective plastic energy for fracture initiation, and ξ^p is a parameter that tracking the activation of plastic-induced fracture.

Owing to the regularity of the energetic functions, first-order optimality condition is sufficient to ensure stability and energy balance leading to the following Karush-Kuhn-Tucker (KKT) conditions:

$$\dot{\mathfrak{d}}_{FF} \geq 0 \text{ and } \dot{\mathfrak{d}}_{IFF} \geq 0, \tag{3.49}$$

ÁMBITO- PREFIJO
GEISER
Nº registro
O00008744e2000024753
CSV
GEISER-aa34-5f08-a669-4b6e-9258-ed2f-d009-e7f3
DIRECCIÓN DE VALIDACIÓN
FECHA Y HORA DEL DOCUMENTO
19/06/2020 12:08:12 Horario peninsular
GEISER-aa34-5f08-a669-4b6e-9258-ed2f-d009-e7f3

$$2(1-\mathfrak{d}_{FF})\mathfrak{P}_{FF}\mathscr{H}_{FF}-\mathscr{G}_{c,FF}\delta_{\mathfrak{d}_{FF}}\gamma(\mathfrak{d}_{FF},\nabla\mathfrak{d}_{FF})\leq 0, \tag{3.50}$$

$$2(1-\mathfrak{d}_{IFF})\mathfrak{P}_{IFF}\mathscr{H}_{IFF}-\mathscr{G}_{c,IFF}\delta_{\mathfrak{d}_{IFF}}\gamma(\mathfrak{d}_{IFF},\nabla\mathfrak{d}_{IFF})\leq 0, \tag{3.51}$$

$$\Big[2(1-\mathfrak{d}_{FF})\mathfrak{P}_{FF}\mathscr{H}_{FF}-\mathscr{G}_{c,FF}\delta_{\mathfrak{d}_{FF}}\gamma(\mathfrak{d}_{FF},\nabla\mathfrak{d}_{FF})\Big]\,\dot{\mathfrak{d}}_{FF}=0, \tag{3.52}$$

$$\Big[2(1-\mathfrak{d}_{IFF})\mathfrak{P}_{IFF}\mathscr{H}_{IFF}-\mathscr{G}_{c,IFF}\delta_{\mathfrak{d}_{IFF}}\gamma(\mathfrak{d}_{IFF},\nabla\mathfrak{d}_{IFF})\Big]\,\dot{\mathfrak{d}}_{IFF}=0. \tag{3.53}$$

3.4 Finite Element Implementation

In this section, the finite element implementation of the proposed multi phase-field fracture model for LFRPs is outlined. The specific operations rely on the framework proposed in [91]. Furthermore, as discussed below, in this investigation, a staggered solution scheme is used for the coupled system of equations. Alternative solution procedures as those given in [138, 139] can be also applicable with relatively minor modifications, which is a task beyond the scope of the present paper.

The solution of the proposed elasto-plastic multi phase-field fracture problem is obtained after discretizing the space using the Finite Element Method (FEM). This means, the continuous domain of the body $\mathscr{B}$ is approximated by a discrete domain $\mathscr{B}^h$ that is formed by a finite number of disjoints elements $\mathscr{B}^e$. There accordingly, the infinite-dimensional function spaces $\mathscr{U}$ and $\mathscr{V}$ are approximated by the corresponding finite-dimensional subspaces $\mathscr{U}^h$ and $\mathscr{V}^h$, imposing the same conditions on the boundaries.

The interpolation of the continuous element fields $\mathbf{u}^e$, $\mathfrak{d}^e_{FF}$, and $\mathfrak{d}^e_{IFF}$ is realized via the use of the element-based shape functions:

$$\mathbf{u}^e=\sum_{i=1}^{N_{\text{node}}}\mathbf{N}^u_i\mathbf{u}^e_i,\quad \mathfrak{d}^e_{FF}=\sum_{i=1}^{N_{\text{node}}}N^{\mathfrak{d}}_i\mathfrak{d}^e_{FF,i},\quad \mathfrak{d}^e_{IFF}=\sum_{i=1}^{N_{\text{node}}}N^{\mathfrak{d}}_i\mathfrak{d}^e_{IFF,i}, \tag{3.54}$$

where $\mathbf{N}^u_i$ and $N^{\mathfrak{d}}_i$ are the shape functions associated with node i for the displacement field $\mathbf{u}^e_i$ and the two phase-field values $\mathfrak{d}^e_{FF,i}$, $\mathfrak{d}^e_{IFF,i}$, respectively, for N_{node} in the finite element. The derivatives associated with the fields $\mathbf{u}$, $\mathfrak{d}_{FF}$, and $\mathfrak{d}_{IFF}$ are expressed as follows, respectively:

$$\boldsymbol{\varepsilon}^e=\sum_{i=1}^{N_{\text{node}}}\mathbf{B}^u_i\mathbf{u}^e_i,\quad \nabla\mathfrak{d}^e_{FF}=\sum_{i=1}^{N_{\text{node}}}\mathbf{B}^{\mathfrak{d}}_i\mathfrak{d}^e_{FF,i},\quad \nabla\mathfrak{d}^e_{IFF}=\sum_{i=1}^{N_{\text{node}}}\mathbf{B}^{\mathfrak{d}}_i\mathfrak{d}^e_{IFF,i}, \tag{3.55}$$

where $\mathbf{B}^u_i$ and $\mathbf{B}^{\mathfrak{d}}_i$ are the corresponding spatial derivatives of the shape functions.

Similarly, the test functions and their respective derivatives take the form:

$$\delta\mathbf{u}^e=\sum_{i=1}^{N_{\text{node}}}\mathbf{N}^u_i\delta\mathbf{u}^e_i,\quad \delta\mathfrak{d}^e_{FF}=\sum_{i=1}^{N_{\text{node}}}\mathbf{N}^{\mathfrak{d}}_i\delta\mathfrak{d}^e_{FF,i},\quad \delta\mathfrak{d}^e_{IFF}=\sum_{i=1}^{N_{\text{node}}}\mathbf{N}^{\mathfrak{d}}_i\delta\mathfrak{d}^e_{IFF,i}, \tag{3.56}$$

$$\delta\boldsymbol{\varepsilon}^e=\sum_{i=1}^{N_{\text{node}}}\mathbf{B}^u_i\delta\mathbf{u}^e_i,\quad \nabla\delta\mathfrak{d}^e_{FF}=\sum_{i=1}^{N_{\text{node}}}\mathbf{B}^{\mathfrak{d}}_i\delta\mathfrak{d}^e_{FF,i},\quad \nabla\delta\mathfrak{d}^e_{IFF}=\sum_{i=1}^{N_{\text{node}}}\mathbf{B}^{\mathfrak{d}}_i\delta\mathfrak{d}^e_{IFF,i}. \tag{3.57}$$

ÁMBITO- PREFIJO
GEISER
Nº registro
O00008744e2000024753
CSV
GEISER-aa34-5f08-a669-4b6e-9258-ed2f-d009-e7f3
DIRECCIÓN DE VALIDACIÓN
FECHA Y HORA DEL DOCUMENTO
19/06/2020 12:08:12 Horario peninsular
GEISER-aa34-5f08-a669-4b6e-9258-ed2f-d009-e7f3

The element residual vectors for the displacement and the two phase-fields can be reduced to:

$$\begin{aligned}\mathscr{R}_e^{\mathbf{u}} = &\int_{\mathscr{B}^e} (1-\mathfrak{d}_{FF})^2 (\mathbf{B}^u)^T \hat{\boldsymbol{\sigma}}_{FF} + (1-\mathfrak{d}_{IFF})^2 (\mathbf{B}^u)^T \hat{\boldsymbol{\sigma}}_{IFF} \mathrm{d}\Omega - \int_{\mathscr{B}^e} (\mathbf{N}^u)^T \mathbf{f}_v \mathrm{d}\Omega \\ &- \int_{\partial \mathscr{B}_t^e} (\mathbf{N}^u)^T \bar{\mathbf{t}} \mathrm{d}\partial\Omega,\end{aligned} \tag{3.58}$$

$$\mathscr{R}_e^{\mathfrak{d}_{FF}} = \int_{\mathscr{B}^e} \left[\frac{\mathscr{G}_{c,FF}}{l_{FF}} \mathfrak{d}_{FF} - 2(1-\mathfrak{d}_{FF}) \mathfrak{P}_{FF} \mathscr{H}_{FF} \right] (N^{\mathfrak{d}})^T + \mathscr{G}_{c,FF} l_{FF} (\mathbf{B}^{\mathfrak{d}})^T \nabla \mathfrak{d}_{FF} \mathrm{d}\Omega, \tag{3.59}$$

$$\mathscr{R}_e^{\mathfrak{d}_{IFF}} = \int_{\mathscr{B}^e} \left[\frac{\mathscr{G}_{c,IFF}}{l_{IFF}} \mathfrak{d}_{IFF} - 2(1-\mathfrak{d}_{IFF}) \mathfrak{P}_{IFF} \mathscr{H}_{IFF} \right] (N^{\mathfrak{d}})^T + \mathscr{G}_{c,IFF} l_{IFF} (\mathbf{B}^{\mathfrak{d}})^T \nabla \mathfrak{d}_{IFF} \mathrm{d}\Omega. \tag{3.60}$$

Notice that the system of equations is non-linear due to the presence of plasticity and fracture. Hence, after assembling, one must resort to incremental iterative solvers such as Newton-Raphson (NR). It is clear that the phase-field equations, see Eqs.(3.59) and (3.60), are uncoupled from each other, but coupled with the equilibrium equation, see Eq.(3.58). However, the global system of equations is solved using an alternating minimization scheme to decouple the displacement and the phase-field problem (fixed point minimization algorithm).

The corresponding Newton-Raphson iteration for the global assembled system at step $(n+1)$ can be written as:

$$\begin{bmatrix} \mathbf{u} \\ \mathfrak{d}_{FF} \\ \mathfrak{d}_{IFF} \end{bmatrix}_{n+1} = \begin{bmatrix} \mathbf{u} \\ \mathfrak{d}_{FF} \\ \mathfrak{d}_{IFF} \end{bmatrix}_{n} - \begin{bmatrix} \mathscr{K}^{\mathbf{uu}} & 0 & 0 \\ 0 & \mathscr{K}^{\mathfrak{d}_{FF}\mathfrak{d}_{FF}} & 0 \\ 0 & 0 & \mathscr{K}^{\mathfrak{d}_{IFF}\mathfrak{d}_{IFF}} \end{bmatrix}_{n+1}^{-1} \begin{bmatrix} \mathscr{R}^{u} \\ \mathscr{R}^{\mathfrak{d}_{FF}} \\ \mathscr{R}^{\mathfrak{d}_{IFF}} \end{bmatrix}_{n}, \tag{3.61}$$

where the corresponding element stiffness matrices read:

$$\mathscr{K}_e^{\mathbf{uu}} := \frac{\partial \mathscr{R}_e^{\mathbf{u}}}{\partial \mathbf{u}^e} = \int_{\mathscr{B}^e} (\mathbf{B}^u)^T \mathbb{C}^{ep\mathfrak{d}} \mathbf{B}^u \mathrm{d}\Omega, \tag{3.62}$$

$$\mathscr{K}_e^{\mathfrak{d}_{FF}\mathfrak{d}_{FF}} := \frac{\partial \mathscr{R}_e^{\mathfrak{d}_{FF}}}{\partial \mathfrak{d}_{FF}^e} = \int_{\mathscr{B}^e} \left[\frac{\mathscr{G}_{c,FF}}{l_{FF}} + 2\mathfrak{P}_{FF} \mathscr{H}_{IFF} \right] \mathbf{N}^{\mathfrak{d}} (\mathbf{N}^{\mathfrak{d}})^T + \mathscr{G}_{c,FF} l_{FF} (\mathbf{B}^{\mathfrak{d}})^T \mathbf{B}^{\mathfrak{d}} \mathrm{d}\Omega, \tag{3.63}$$

$$\mathscr{K}_e^{\mathfrak{d}_{IFF}\mathfrak{d}_{IFF}} := \frac{\partial \mathscr{R}_e^{\mathfrak{d}_{IFF}}}{\partial \mathfrak{d}_{IFF}^e} = \int_{\mathscr{B}^e} \left[\frac{\mathscr{G}_{c,IFF}}{l_{IFF}} + 2\mathfrak{P}_{IFF} \mathscr{H}_{IFF} \right] \mathbf{N}^{\mathfrak{d}} (\mathbf{N}^{\mathfrak{d}})^T + \mathscr{G}_{c,IFF} l_{IFF} (\mathbf{B}^{\mathfrak{d}})^T \mathbf{B}^{\mathfrak{d}} \mathrm{d}\Omega, \tag{3.64}$$

and $\mathbb{C}^{ep\mathfrak{d}}$ is the material consistent tangent.

The above system of equations has been implemented in the general-purpose FE package `ABAQUS` to take advantage of the in-built non-linear solvers and automatic time-stepping methods. Hence, a user-defined `UMAT` is written for the solution of equilibrium equations associated with the displacement field whereas `UEL` is utilized for solving the phase-field fracture problem. A three-layer structure (for each ply) is adopted as shown in Figure 3.2, corresponding to the displacement field and the two phase-fields, where each of the layers shares the same nodes but has different

ÁMBITO- PREFIJO
GEISER
Nº registro
O00008744e2000024753
CSV
GEISER-aa34-5f08-a669-4b6e-9258-ed2f-d009-e7f3
DIRECCIÓN DE VALIDACIÓN
FECHA Y HORA DEL DOCUMENTO
19/06/2020 12:08:12 Horario peninsular
GEISER-aa34-5f08-a669-4b6e-9258-ed2f-d009-e7f3

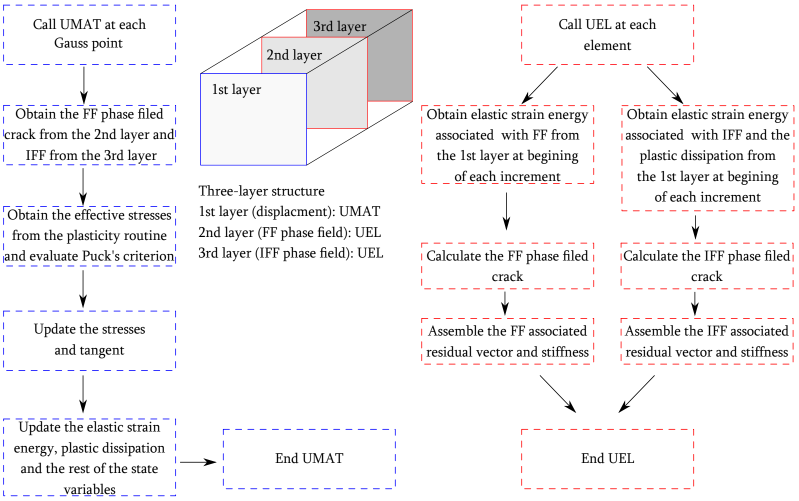
Call UMAT at each Gauss point
Obtain the FF phase filed crack from the 2nd layer and IFF from the 3rd layer
Obtain the effective stresses from the plasticity routine and evaluate Puck's criterion
Update the stresses and tangent
Update the elastic strain energy, plastic dissipation and the rest of the state variables
End UMAT
3rd layer
2nd layer
1st layer
Three-layer structure
1st layer (displacment): UMAT
2nd layer (FF phase field): UEL
3rd layer (IFF phase field): UEL
Call UEL at each element
Obtain elastic strain energy associated with FF from the 1st layer at begining of each increment
Obtain elastic strain energy associated with IFF and the plastic dissipation from the 1st layer at begining of each increment
Calculate the FF phase filed crack
Calculate the IFF phase filed crack
Assemble the FF associated residual vector and stiffness
Assemble the IFF associated residual vector and stiffness
End UEL

Figure 3.2 Three-layer structure of `ABAQUS` subroutine.

stiffness and Degrees of Freedom (DOFs). The elements in the first layer contain three DOFs (two for the 2D case), whereas the second and third layers have one DOF of phase-field $\mathfrak{d}_{FF}$ and $\mathfrak{d}_{IFF}$, respectively. The `UMAT` is called at each Gauss point in the first layer to evaluate the constitutive behavior of the displacement field. To be specific, the anisotropic elasto-plastic model presented in Section 3.2 provides the elastic and plastic strains along with their corresponding effective stresses. Subsequently, at each Gauss point, the stresses are checked against the Puck failure criteria to predict the failure modes and activation flags. Since the degradation of the energy entirely depends on the type of failure (i.e fiber failure or inter-fiber failure) different driving forces are computed accordingly. The `UEL` is called at each element in the second and third layers. Depending on the computed driving force and activation flags, the corresponding phase-field values are computed.

The corresponding layers in the system disseminate through the common block. After each increment, the solution dependent variables are stored as `STATEV` in `UMAT` to post-process the results.

3.5 Representative Applications

In this section, different numerical examples are presented showing the predictive capabilities of the proposed formulation.

3.5.1 Material Parameters

Herein, two different materials are considered, CFRP (IM7/8552) and GFRP (E-Glass/MY750), and the proposed model is calibrated on the experimental data provided in [111, 140, 141] and the references therein given. The elastic material constants of the CFRP and GFRP materials are listed in Table 3.2.

Following the procedure presented in [95], the yield function parameters ζ_i $(i = 1{,}4)$ that characterize the onset of yielding are listed in Table 3.3 for CFRP and GFRP.

The plastic potential function parameters ς_i $(i = 2{,}3)$ are obtained for the CFRP and GFRP for the plastic Poisson's ratios given in Table 3.4.

ÁMBITO- PREFIJO
GEISER
Nº registro
O00008744e2000024753
CSV
GEISER-aa34-5f08-a669-4b6e-9258-ed2f-d009-e7f3
DIRECCIÓN DE VALIDACIÓN
FECHA Y HORA DEL DOCUMENTO
19/06/2020 12:08:12 Horario peninsular
GEISER-aa34-5f08-a669-4b6e-9258-ed2f-d009-e7f3

Table 3.2 CFRP and GFRP: elastic properties..

Material	E_{11} (GPa)	E_{22} (GPa)	G_{12} (GPa)	ν_{12} (minor)	ν_{23}
CFRP	171.42	9.08	5.39	0.0169	0.38
GFRP	45.6	16.2	5.83	0.099	0.4

Table 3.3 CFRP and GFRP: yielding parameters ζ_i at the onset of yielding..

Material	ζ_1	ζ_2	ζ_3	ζ_4
CFRP	0.00262532	0.00179157	-0.0097352	0.00411623
GFRP	0.00338351	0.00230897	-0.0110519	0.00530498

Table 3.4 CFRP and GFRP: plastic Poisson's ratios..

Material	μ^p_{12}	ν^p_{23}
CFRP	1.0	0.38
GFRP	1.0	0.4

Furthermore, for the Puck failure criteria, the strength properties are listed in Table 3.5 for the CFRP and GFRP materials.

Table 3.5 CFRP and GFRP: strength properties..

Material	$R^t_{\parallel}$ (MPa)	$R^c_{\parallel}$ (MPa)	$R^t_{\perp}$ (MPa)	$R^c_{\perp}$ (MPa)	$R_{\parallel\perp}$ (MPa)
CFRP	2323.5	1200.1	62.3	199.8	92.3
GFRP	1280	800	40	145	73.3

In addition, the fracture properties and phase-field parameters are reported in Table 3.6 for CFRP and GFRP.

Table 3.6 CFRP and GFRP: fracture properties and phase-field parameters..

Material	$\mathcal{G}_{c,FF}$ (N/mm)	$\mathcal{G}_{c,IFF}$ (N/mm)	l_{FF} (mm)	l_{IFF} (mm)	$\xi_{e,FF}$ (-)	$\xi_{e,IFF}$ (-)	ξ_p (-)
CFRP	81.5	0.2774	0.273	0.07	50 (assumed)	0.5 (assumed)	0.5 (assumed)
GFRP	64	1.8	0.19	1.9	50 (assumed)	0.5 (assumed)	0.5 (assumed)

3.5.2 Validation of Implementation

Herein, the validity and potential of the proposed formulation are assessed utilizing a single element FE model. The CFRP 3D brick element's side length is set to be 1mm. Four load cases (corresponding to four different failure modes) are considered for which the fiber direction is taken as reference: (i) longitudinal uniaxial tension, (ii) transverse uniaxial tension, (iii) transverse uniaxial compression, and (iv) in-plane shear.

With respect to the loading, in all the four cases, the element is loaded under displacement control with constant increment $\Delta u = 0.0001$mm in order to ensure the stability of the numerical solution.

The numerical results of the first load case (longitudinal uniaxial tension) are depicted in Figure 3.3. In this plot, it can be observed that, throughout the first part of the evolution, i.e.

ÁMBITO- PREFIJO
GEISER
Nº registro
O00008744e2000024753
CSV
GEISER-aa34-5f08-a669-4b6e-9258-ed2f-d009-e7f3
DIRECCIÓN DE VALIDACIÓN
FECHA Y HORA DEL DOCUMENTO
19/06/2020 12:08:12 Horario peninsular
GEISER-aa34-5f08-a669-4b6e-9258-ed2f-d009-e7f3

before the material strength is reached, linear elastic behavior is retrieved. Once the fiber failure onset criterion is satisfied, the fiber failure phase-field crack variable commences evolving.

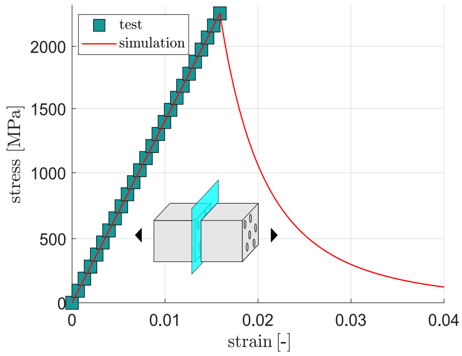

Figure 3.3 Numerical simulations and experimental results: FF Mode.

The results from the second loading case (transverse uniaxial tension) are shown in Figure 3.4.a. Herein, the pre-failure non-linearities are observed due to the assumption of elasto-plastic behavior in a matrix-dominated response. Once the material strength is reached and the Puck inter-fiber failure criterion is met, the inter-fiber phase-field crack begins to evolve. The orientation of the fracture plane is stored as a state-dependent variable. Hence, under uniaxial tensile conditions, the angle of the fracture plane is obtained to be around $\Theta_{fp} = 0^{\circ}$, which is inline with Mode A in Puck's theory. Similarly, for the third load case (transverse uniaxial compression), the Puck inter-fiber failure criterion is violated, see Figure 3.4.b. However, in this case, the angle of the fracture plane is predicted to be around $\Theta_{fp} = 53^{\circ}$ i.e. Mode C according to the Puck theory.

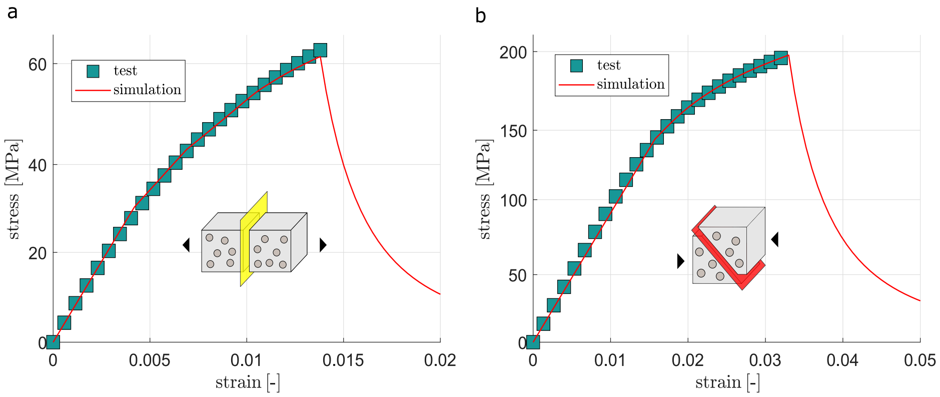

Figure 3.4 Numerical simulations and experimental results: (a) IFF Mode A and (b) IFF Mode C.

In the fourth loading case, the applicability of the proposed model for triggering the failure of the CFRP material under in-plane shear is examined. Similarly, the elasto-plastic model is used to predict the experimentally observed prominent pre-failure non-linearities due to plasticity associated with such load cases, see Figure 3.5.a. In accordance with Puck theory, inter-fiber failure with a fracture plane angle of $\Theta_{fp} = 0^\circ$ is predicted. The simultaneous evolution of the plastic deformations and the cracking process is depicted in Figure 3.5.b.

The ability of the proposed multi phase-field model to predict the different fracture mechanisms observed in long fiber reinforced composites can clearly be noticed. Furthermore, in all the examined loading cases, a very satisfactory agreement between the experimental data (up to failure [111]) and the numerical predictions can be noticed.

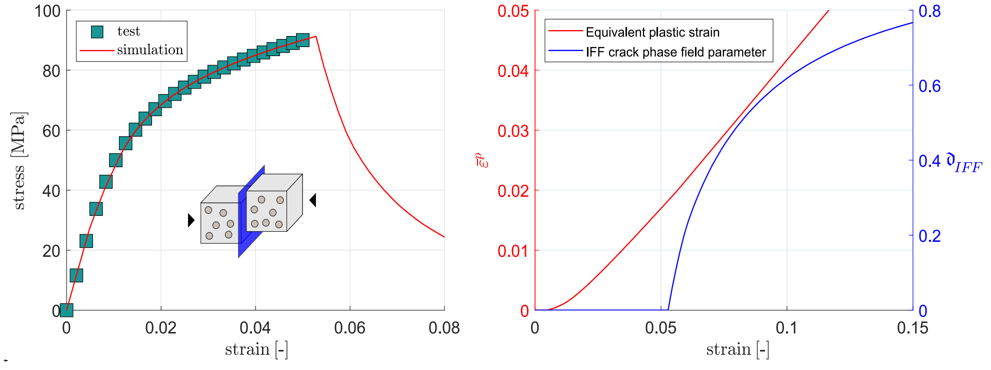

Figure 3.5 Numerical simulations and experimental results of the pure shear case: (a) stress-strain response and (b) simultaneous evolution of the plastic deformations and the inter-fiber cracking process.

3.5.3 Demonstrative Examples

In the preset section, the potential of the proposed formulation to capture the anisotropic fracture behavior of long fiber composites is demonstrated. For this purpose, a FE model that mimics a plate with an initial notch made of GFRP composites is constructed. The plate is partitioned into four regions to allow assigning different fiber orientations to each one. The geometry, partitioning, boundary conditions, and loading are depicted in Figure 3.6. Three different fiber orientation arrangements are considered in the present study, which are listed in Table 3.7.

Table 3.7 GFRP plate with an initial notch: fiber orientation arrangement for the three different cases..

	Region 1	Region 2	Region 3	Region 4
Case 1	0°	0°	0°	0°
Case 2	-45°	-45°	0°	0°
Case 3	0°	0°	-45°	-45°

The domain is discretized employing 251000 4-node quadrilateral plane stress elements. In all the three cases, the plate is loaded under displacement control with constant increment $\Delta u = 0.0001$mm.

The numerical predictions obtained from the three different cases are presented in Figures 3.7-3.9. Inline with previous research [66], matrix-dominated cracking evolution is predicted. Figures 3.7-3.9 depicts the different phases of the cracking evolution whereby significant crack kinks between adjacent layers are obtained stemming from the differences between the corresponding

ÁMBITO- PREFIJO
GEISER
Nº registro
O00008744e2000024753
CSV
GEISER-aa34-5f08-a669-4b6e-9258-ed2f-d009-e7f3
DIRECCIÓN DE VALIDACIÓN
FECHA Y HORA DEL DOCUMENTO
19/06/2020 12:08:12 Horario peninsular
GEISER-aa34-5f08-a669-4b6e-9258-ed2f-d009-e7f3

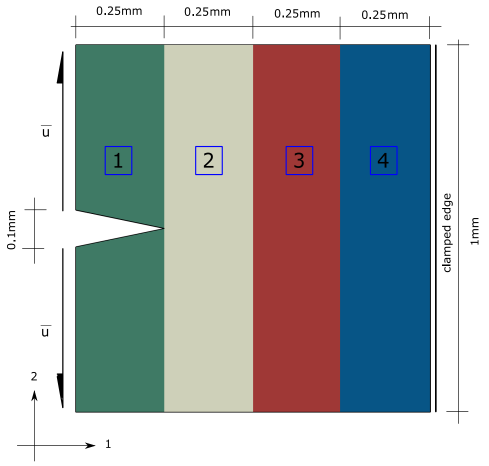

Figure 3.6 GFRP plate with an initial notch: specimen geometry and boundary conditions.

material orientations. Hence, the capability of the proposed implemented model to predict the anisotropic fracture behavior of long fiber reinforced composites can be observed.

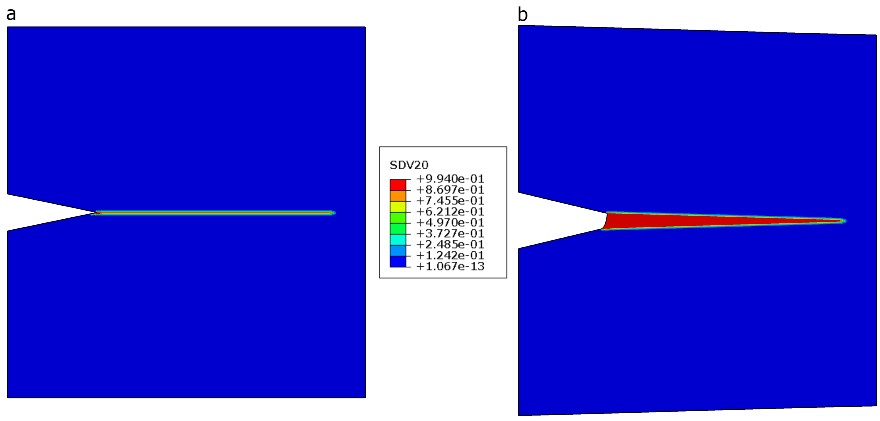

Figure 3.7 Inter-fiber phase-field crack (SDV20) from case 1 of the GFRP plate in: (a) undeformed configuration and (b) deformed configuration.

3.5.4 Open-Hole Tension Problem

The proposed multi phase-field formulation is applied to predict the progressive failure of an open-hole FRPs specimen. The geometric definition of the specimen under consideration is shown in Figure 3.10, replicating the 3mm thick CFRP quasi-isotropic $[90^\circ/0^\circ/\pm 45^\circ]_{3s}$ laminate investigated in [111] employing a CDM model. The specimen is discretized employing 475008 8-node 3D brick elements. Two elements per ply are used. Inline with [111], the following in-situ strengths are incorporated into the model based on the formulation proposed in [142], see Table 3.8. The specimen is loaded under tension until failure via displacement control with constant increment $\Delta u = 0.0001$mm.

ÁMBITO- PREFIJO
GEISER
Nº registro
O00008744e2000024753
CSV
GEISER-aa34-5f08-a669-4b6e-9258-ed2f-d009-e7f3
DIRECCIÓN DE VALIDACIÓN
FECHA Y HORA DEL DOCUMENTO
19/06/2020 12:08:12 Horario peninsular
GEISER-aa34-5f08-a669-4b6e-9258-ed2f-d009-e7f3

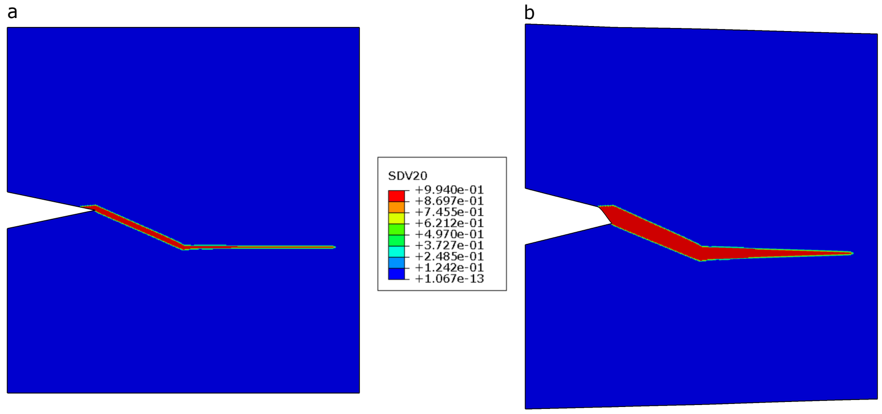

Figure 3.8 Inter-fiber phase-field crack (SDV20) from case 2 of the GFRP plate in: (a) undeformed configuration and (b) deformed configuration.

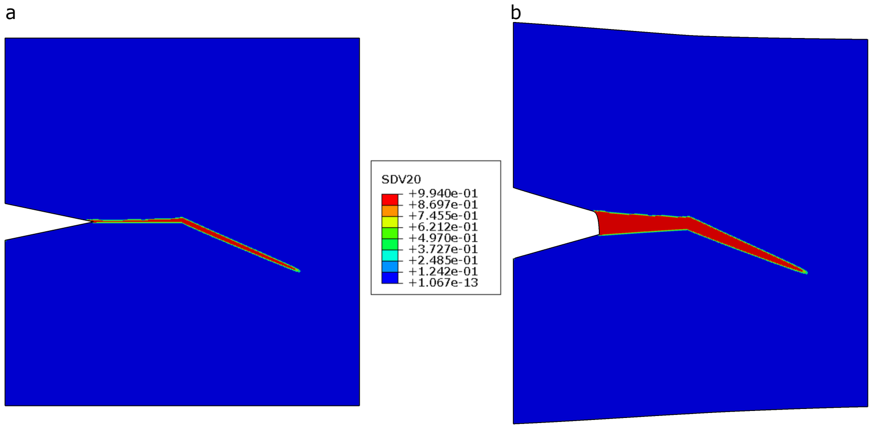

Figure 3.9 Inter-fiber phase-field crack (SDV20) from case 3 of the GFRP plate in: (a) undeformed configuration and (b) deformed configuration.

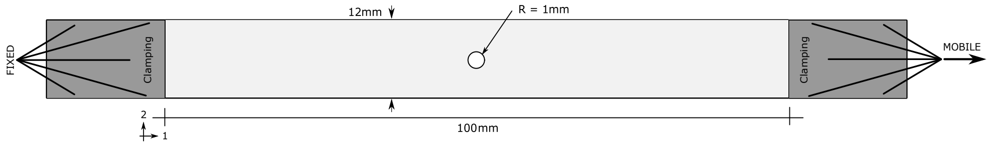

Figure 3.10 open-hole tension problem: specimen geometry and boundary conditions.

The numerical-experimental correlation corresponding to the load-displacement curve is depicted in Figure 3.11. In both cases (numerical and experimental) and before the maximum strength is reached, a bilinear evolution of the curve is observed. Therein, an initial linear evolution stage followed by a quasi-linear evolution due to the initiation and development of damage and failure. Despite the fact that the numerically predicted initial linear stage of the curve matches perfectly the experimental results, in the quasi-linear stage, a stiffer response

ÁMBITO- PREFIJO
GEISER
Nº registro
O00008744e2000024753
CSV
GEISER-aa34-5f08-a669-4b6e-9258-ed2f-d009-e7f3
DIRECCIÓN DE VALIDACIÓN
FECHA Y HORA DEL DOCUMENTO
19/06/2020 12:08:12 Horario peninsular
GEISER-aa34-5f08-a669-4b6e-9258-ed2f-d009-e7f3

Table 3.8 CFRP: in-situ strengths properties.

	$R^t_\perp$ (MPa)	$R_{\parallel\perp}$ (MPa)
Embedded plies	106.2	101.4
Outer plies	130.2	107.0

is predicted. Such discrepancies are attributed to the fact that inter-laminar failures are not considered appropriately in this simulation and hence the interaction between intra-laminar and inter-laminar fracture events. However, a satisfactory agreement between the numerical and the experimental data can be observed.

The inter-fiber and fiber failure patterns at different loading stages (40%, 65%, 85% of the ultimate load, and rupture) are shown in Figures 3.12 and 3.13, respectively. As depicted in Figure 3.12, an X-shaped inter-fiber crack pattern is observed in the 90° ply. With respect to the 0° ply, tensile fiber failure is predicted, see Figure 3.13. Inline with [111], a net section failure mode is predicted in which the cracks are initially concentrated around the hole and subsequently propagate perpendicular to the loading direction.

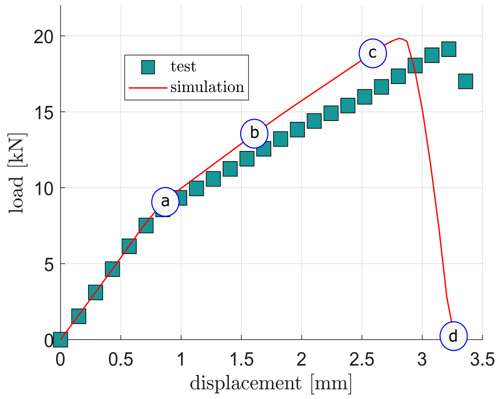

Figure 3.11 Open-hole tension problem: Numerical-experimental correlation corresponding to the load-displacement curve.

3.6 Concluding Remarks

Relying on Puck theory of failure, fracture events in Long Fiber Reinforced Polymers (LFRPs) at ply level can be mainly classified into fiber and inter-fiber (matrix-dominated) cracking. In order to account for such failure mechanisms into the Phase-Field (PF) approach to fracture, a novel multi phase-field model was proposed. Particularly, in the present investigation, a novel model was formulated that is characterized by: (i) the consideration of a single crack-like phase-field variable for each failure mechanism with corresponding fracture energy and length scale and (ii) the employment of an invariant-based pressure-dependent plasticity model for characterizing matrix-failure dominated states.

The proposed formulation was carefully derived via a multi-field variational formalism with the specific incorporation of the multiple dissipative mechanisms within the spirit of the PF method. Special attention was also devoted to the consistent numerical implementation.

ÁMBITO- PREFIJO
GEISER
Nº registro
O00008744e2000024753
CSV
GEISER-aa34-5f08-a669-4b6e-9258-ed2f-d009-e7f3
DIRECCIÓN DE VALIDACIÓN
FECHA Y HORA DEL DOCUMENTO
19/06/2020 12:08:12 Horario peninsular
GEISER-aa34-5f08-a669-4b6e-9258-ed2f-d009-e7f3

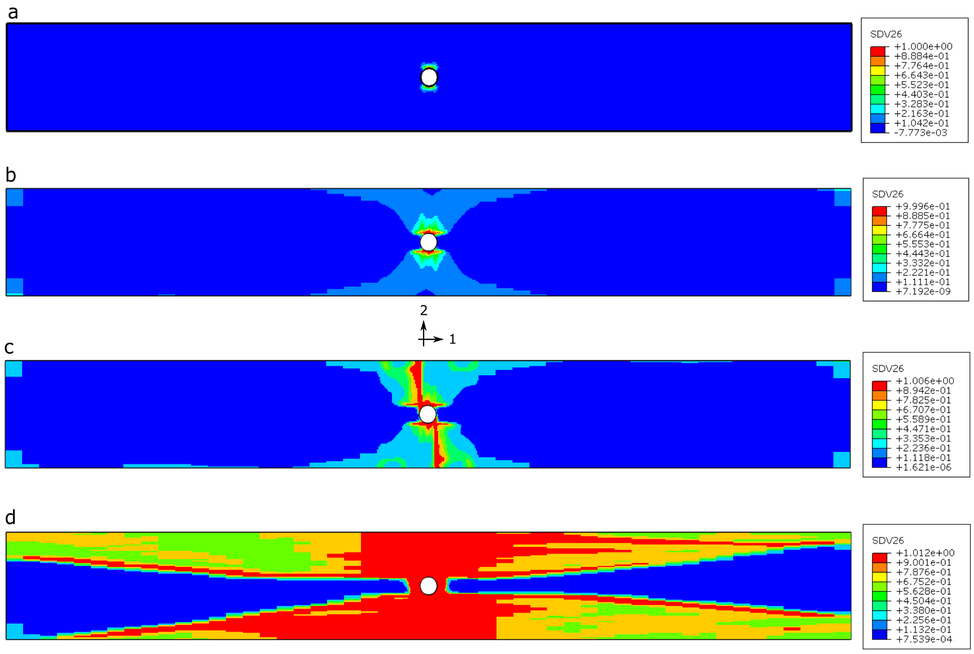

Figure 3.12 Open-hole tension problem: IFF phase-field crack (SDV26) evolution in the outer 90° layer at different loading stages: (a) 60% of the ultimate load, (b) 80% of the ultimate load, (c) 100% of the ultimate load, and (d) rupture.

On the applicability side, several illustrative examples evidenced the reliability of the proposed formulation. Finally, it is worth noting that this work can be conceived as a first attempt whereby phenomenological failure criteria for FRPs are integrated into PF methods.

ÁMBITO- PREFIJO
GEISER
Nº registro
O00008744e2000024753
CSV
GEISER-aa34-5f08-a669-4b6e-9258-ed2f-d009-e7f3
DIRECCIÓN DE VALIDACIÓN
FECHA Y HORA DEL DOCUMENTO
19/06/2020 12:08:12 Horario peninsular
GEISER-aa34-5f08-a669-4b6e-9258-ed2f-d009-e7f3

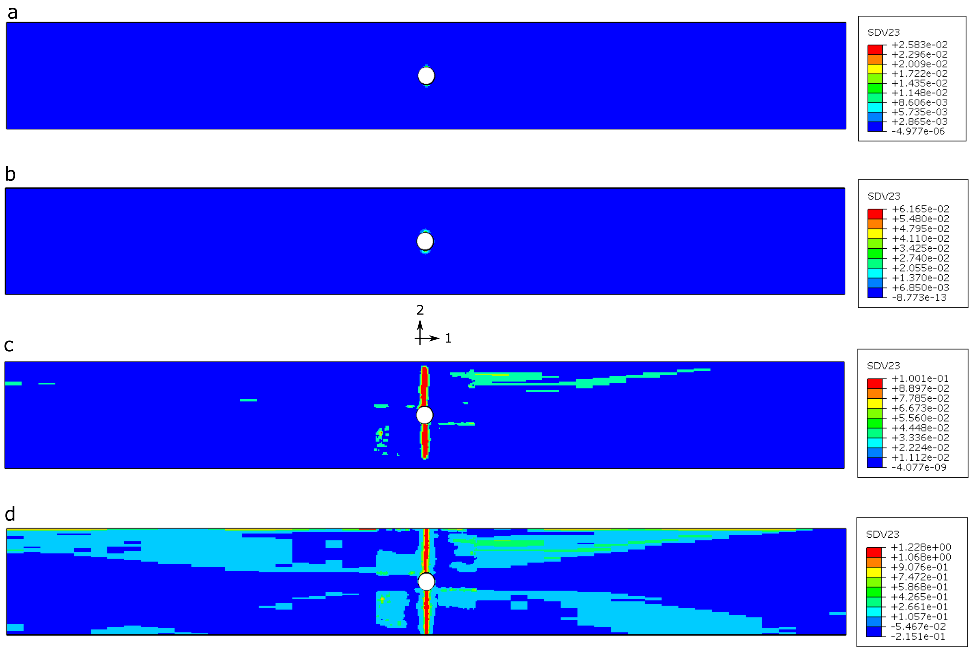

Figure 3.13 Open-hole tension problem: FF phase-field crack (SDV23) evolution in the outer 0° layer at different loading stages: (a) 60% of the ultimate load, (b) 80% of the ultimate load, (c) 100% of the ultimate load, and (d) rupture.

ÁMBITO- PREFIJO
GEISER
Nº registro
O00008744e2000024753
CSV
GEISER-aa34-5f08-a669-4b6e-9258-ed2f-d009-e7f3
DIRECCIÓN DE VALIDACIÓN
FECHA Y HORA DEL DOCUMENTO
19/06/2020 12:08:12 Horario peninsular
GEISER-aa34-5f08-a669-4b6e-9258-ed2f-d009-e7f3

4 FE Modeling and Simulation of Delamination Migration in Multi-Layered Long Fiber Reinforced Polymers

This chapter presents a paper that regards the employment of the newly developed multi phase-field model together with a cohesive zone model into the modeling and simulation of delamination migration in multi-layered long fiber reinforced polymers. The paper is submitted for publication in Composites Part B: Engineering, May 2020.

ÁMBITO- PREFIJO
GEISER
Nº registro
O00008744e2000024753
CSV
GEISER-aa34-5f08-a669-4b6e-9258-ed2f-d009-e7f3
DIRECCIÓN DE VALIDACIÓN
FECHA Y HORA DEL DOCUMENTO
19/06/2020 12:08:12 Horario peninsular
GEISER-aa34-5f08-a669-4b6e-9258-ed2f-d009-e7f3

Abstract. Failure processes in Long Fiber Reinforced Polymers (LFRPs) entail the development and progression of different physical mechanisms and in particular the interaction between inter-laminar and intra-laminar cracking. Reliable modeling of such complex scenarios can be achieved through the development of robust numerical predictive tools that allow for the interaction of both failure modes. In this study, a novel multi Phase-Field (PF) model relying on the Puck theory of failure for intra-laminar failure at ply level is efficiently coupled with a Cohesive Zone Model (CZM) for inter-laminar cracking, in order to simulate delamination migration cracking events in multi-layered FRPs. The current computational method is numerically implemented as a system of non-linear partially coupled equations using the finite element method via user-defined `UMAT` and `UEL` subroutines in `ABAQUS`. The computational tool applied for the prediction of delamination migration in multi-layered LFRPs comprising 44 cross-ply. The reliability of the current approach is examined via the correlation with experimental results, exhibiting numerous kinking events until the collapsing point. Finally, the current study is complemented with additional representative examples with the aim of providing further insight into the potential role of different aspects of the system, including the variation of (i) the ply angle in the migration zone, (ii) the load application point, and (iii) initial crack length.

4.1 Introduction

The widespread use of Fiber Reinforced Polymers FRPs (generally encompassing carbon and glass reinforced polymeric composites, CFRP and GFRP, respectively) due to their high strength to weight ratios has paved their way into many practical applications in different industrial sectors, with special impact in aerospace and aeronautics, and more recently in automotive sector [85, 86], to quote a few of them. In the presence of ever-increasing demands of new technological advancements, load-bearing capabilities and failure modes of these materials are not yet fully understood, posing notable restrictions on their use and leading to the introduction of high safety factors.

Within this context, delamination failure can be conceived as one of the most critical failure mechanisms in multi-layered Long Fiber Reinforced Polymers (LFRPs). Such cracking events are generally associated with low through-thickness stiffness in layered disposals and can emerge from manufacturing defects, the occurrence of post-buckling phenomena [143, 144], among many others. From a modeling standpoint, delamination events in layered composites structures have been analyzed using Linear Elastic Fracture Mechanics (LEFM) enforcing initiation and growth along the ply interface with the use of strain energy-based methods in order to define the corresponding fracture toughness [145, 146]. Delamination can be found in low-velocity impact [147], skin debonding [148], defects from notches [149], among many other practical cases. These phenomena have been extensively investigated based on cohesive-like cracking methods in pre-notched coupon configurations, whereby an ad-hoc inter-laminar failure model can be inserted into the most critical locations of the specimen for triggering such cracking events [50–52, 150]. From a mechanical perspective, delamination can be seen as a result of the coalescence of micro-cracks at the ply-interface, perpendicular to the tensile stress [151–153].

However, for some specific loading cases and configurations, it has been reported that mostly due to the sign of the change of shearing stresses, a pre-existing crack along an interface of the ply can kink out from such location, propagating into the adjacent ply. Matrix-cracking induced by delamination can further progress through the ply thickness and then propagates out at another interface as reported in [151, 154, 155], leading to the so-called delamination migration failure mode. Thus, following the terminologies used in [156], the turning of delamination crack front into one of the adjacent plies is referred to as kinking, whereas, when a crack propagates across the thickness of plies and propagates out in adjacent interface is called migration [157]. The

ÁMBITO- PREFIJO
GEISER
Nº registro
O00008744e2000024753
CSV
GEISER-aa34-5f08-a669-4b6e-9258-ed2f-d009-e7f3
DIRECCIÓN DE VALIDACIÓN
FECHA Y HORA DEL DOCUMENTO
19/06/2020 12:08:12 Horario peninsular
GEISER-aa34-5f08-a669-4b6e-9258-ed2f-d009-e7f3

main causes of such phenomena can be motivated by the analysis of the stress field around the interface crack tip, see the experimental studies conducted in [151, 152, 155, 158].

With regard to the different modeling methods for triggering intra-laminar failure in LFRPs, the use of Continuum Damage Mechanics (CDM)-based methods has been of notable importance, see the phenomenological models proposed in [111, 159] and the references given therein. Notwithstanding, the local versions of CDM models generally suffer from mesh pathological issues that can be remedied using alternative methodologies. Within this context, Phase-Field (PF) methods, originally proposed in [13] and subsequently developed in [14, 43], have become plausible nonlocal modeling alternatives that prevent most of the main limitations of alternative modeling tools for fracture in solids. With strong foundations on Griffith's approach to Fracture Mechanics (FM), PF methods exploit a multi-field variational formalism, whereby fracture is accounted via diffusive representation within a particular region of the domain characterized by the length-scale l. This approach encompasses an energy minimization of the potential energy of the body (split into bulk and fracture counterparts, respectively) resulting in a multi-field Finite Element (FE) formulation, and therefore complex cracking phenomena can be naturally captured due to the implicit consideration of the evolution equation of the corresponding phase-field crack variables. Posterior developments of PF techniques to fracture have been oriented towards the analysis of alternative formulations [56, 57], shells [111], ductile fracture [160, 161], composite materials [65, 66, 121, 123, 137], heterogeneous media [123], hydrogen assisted cracking [61], among many others, and from a numerical point of view striving for different solution strategies [138]. Recently, the authors have proposed the incorporation of phenomenological failure criteria for composite materials widening the range of applicability of PF methods for different composite materials [118].

In this investigation, due to the fact that the delamination migration is mainly a shear dominated failure, two phase-field fracture variables as proposed in [162], each of them accounting for Fiber Failure (FF) and Inter-Fiber Failure (IFF) relying on Puck's failure criteria, are combined with Cohesive Zone Model (CZM) following a bi-linear traction separation law in order to predict the development of such failure events. Consequently, at the intra-ply level, the driving force for each of the failure mechanism within the PF technique, i.e. fiber failure and inter-fiber failure, are exploited independently, and moreover, this fracture model is readily used to capture the kinking and migration events along with delamination. The proposed model is examined against experimental data available in the related literature in order to validate the predictive capabilities of the current simulation technique. In addition to the previous aspects, the current study also encompasses the analysis of the variation of design parameters for which physical solution favors delamination-migration such as load application point, angle of the ply at the interfaces, and initial crack length. Such effects are studied to understand the load-bearing capacity of each of the variations and show the applicability of the proposed model to predict complex failure phenomena.

The chapter is organized as follows. In Section 4.2, the Multi Phase-Field-Cohesive Zone (MPF-CZ) formulation based on the Puck theory of failure is introduced. In Section 4.3, the variational formulation of the model along with the strong form is outlined with a special focus on the particular contribution of each failure mechanism to the system. In Section 4.4, the finite element implementation of the model is derived. The assessment of the proposed framework for its validation is discussed in Section 4.5 in conjunction with a further investigation with respect to the variation of numerous design parameters of the system. Finally, Section 4.6 summarizes the main conclusions of the present study.

ÁMBITO- PREFIJO
GEISER
Nº registro
O00008744e2000024753
CSV
GEISER-aa34-5f08-a669-4b6e-9258-ed2f-d009-e7f3
DIRECCIÓN DE VALIDACIÓN
FECHA Y HORA DEL DOCUMENTO
19/06/2020 12:08:12 Horario peninsular
GEISER-aa34-5f08-a669-4b6e-9258-ed2f-d009-e7f3

4.2 Multi Phase-Field-Cohesive Zone (MPF-CZ) Formulation Based on the Puck Theory of Failure

In this section, the computational framework herein proposed for capturing delamination migration in layered composite structures is outlined. The current method relies on the combination of the multi phase-field formulation for modeling fracture in LFRPs relying on the Puck failure criterion [162] along with the cohesive zone model. Specifically, the principle focus is the construction of numerical formulation of coupled equations encompassing cracks propagation that arises from different physical failure mechanisms.

The point of departure is the consideration of an arbitrary body in the general n_{dim} Euclidean space, occupying the placement $\mathscr{B} \in \mathbb{R}^{n_{\text{dim}}}$, with its external boundary $\partial\mathscr{B} \in \mathbb{R}^{n_{\text{dim}}-1}$, see Figure 4.1. For any material point, the position vector is denoted by $\mathbf{x} \in \mathscr{B}$. The displacement field is identified by the vector $\mathbf{u} : \mathscr{B} \to \mathbb{R}^{n_{\text{dim}}}$, with infinitesimal stain tensor $\boldsymbol{\varepsilon} := \nabla^{\text{sym}}\mathbf{u}$ for $\boldsymbol{\varepsilon} : \mathscr{B} \to \mathbb{R}^{n_{\text{dim}} \times n_{\text{dim}}}$. The displacement boundary conditions are prescribed as $\mathbf{u} = \overline{\mathbf{u}}$ on $\partial\mathscr{B}_u$ and traction conditions are given by $\overline{\mathbf{t}} = \boldsymbol{\sigma} \cdot \mathbf{n}$ on $\partial\mathscr{B}_t$ such that, kinematic and static boundary conditions satisfy: $\overline{\partial\mathscr{B}_t \cup \partial\mathscr{B}_u} = \partial\mathscr{B}$ and $\partial\mathscr{B}_t \cap \partial\mathscr{B}_u = \emptyset$, where $\mathbf{n}$ is outward normal vector and $\boldsymbol{\sigma}$ is the Cauchy stress tensor.

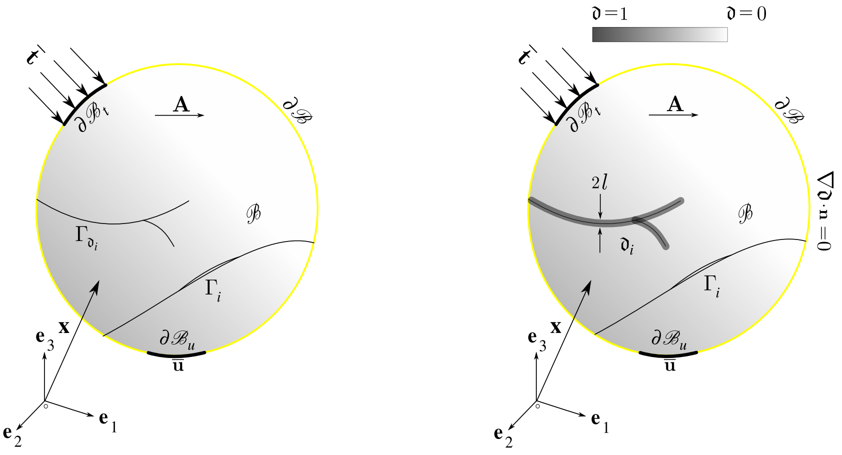

Figure 4.1 Body under consideration: (a) sharp crack representation and (b) regularized crack topology.

In addition to the previous definitions, let Γ be a crack set incorporating interface cracks Γ_i arising from the cohesive zone and cracks in the bulk $\Gamma_{\mathfrak{d}_i}$ from the multi phase-field such that, $\Gamma_i \cup \Gamma_{\mathfrak{d}_i} = \Gamma$ and $\Gamma_i \cap \Gamma_{\mathfrak{d}_i} = \emptyset$ for each discrete $t \in [0,T]$ with $\Gamma_t \subseteq \Gamma_{t+1}$. The displacement jumps along the interface as the relative displacement between two homogeneous points at the flanks are denoted by $\mathfrak{g} = \mathbf{u}_i^+ - \mathbf{u}_i^-$, representing the difference between kinematic field along the interface Γ_i^+ and Γ_i^- inline with [58, 163]. On the other hand, $\Gamma_{\mathfrak{d}_i}$ is defined as the set of discontinuous points $\mathbf{x}$, where $\mathbf{u}$ has one sided approximate limits $\mathbf{u}_{\mathfrak{d}}^+ \neq \mathbf{u}_{\mathfrak{d}}^-$ with respect to a suitable direction $\mathfrak{v}_u$ normal to $\Gamma_{\mathfrak{d}_i}$ inline with [164, 165].

To account for multiple energies in the system, the total free energy functional describing the mechanics of body $\mathscr{B}$ is given as the sum total of internal and external energies acting on the

ÁMBITO- PREFIJO
GEISER
Nº registro
O00008744e2000024753
CSV
GEISER-aa34-5f08-a669-4b6e-9258-ed2f-d009-e7f3
DIRECCIÓN DE VALIDACIÓN
FECHA Y HORA DEL DOCUMENTO
19/06/2020 12:08:12 Horario peninsular
GEISER-aa34-5f08-a669-4b6e-9258-ed2f-d009-e7f3

system as follows, respectively:

$$\Pi(\mathbf{u},\Gamma) = \Pi_{\text{int}}(\mathbf{u},\Gamma) + \Pi_{\text{ext}}(\mathbf{u}). \tag{4.1}$$

In classical CDM, the total internal energy is a state function of strain tensor $\boldsymbol{\varepsilon}$ and internal damage like variable $\mathfrak{d}$ [118, 162]. The consistent generalization of the isotropic damage formulation for the consideration of different failure mechanisms can be postulated by the additive decomposition of total internal energy into multiple contributions, in which each of them is associated with a certain failure mechanism. In such a postulation, a scalar damage variable $\mathfrak{d}_i$ $(i = 1,...,n)$ is associated with each one of the n failure mechanisms, such that $\mathfrak{d}_i = 0$ for intact material state and $\mathfrak{d}_i = 1$ for fully broken state and so that $\mathfrak{d}_i \in [0,1]$ for each $i = 1,...,n$. Moreover, to account for non-local damage evolution, the respective gradients $\nabla\mathfrak{d}_i$ are incorporated in the formulation. This additive decomposition postulation for intra-laminar failure was successfully applied in [159] and later extended to incorporate failure criteria such as Puck failure theory so as to distinguish between the fiber and matrix-dominated damage mechanisms in LFRPs [111, 162]. However, the consideration of dissipative energies stemming from debonding along the interface Γ_i, and crack propagation in the bulk $\Gamma_{\mathfrak{d}_i}$ is still a matter of investigation. The prediction of such crack topology becomes increasingly complex due to branching and coalescence phenomenons, as well as the interaction with diffusive cracks which may induce the debonding process along the existing interface Γ_i. One possibility to achieve this is by employing a phase-field model incorporating multiple diffusive crack fields within the bulk and interface elements relying on cohesive zone methodologies at a prescribed interface inline with [58]. Hence, the total internal energy is now an amalgamation of (i) total elastic energy constituting from bulk (fiber and inter-fiber) energy, (ii) surface energy (crack energy) stemming from bulk (fiber and inter-fiber) failure, and (iii) cohesive interface energy obeying a bi-linear traction-separation law:

$$\Pi_{\text{int}}(\mathbf{u},\Gamma) = \Pi_{\text{int},b}(\mathbf{u},\Gamma_{\mathfrak{d}_i}) + \Pi_{\text{int},c}(\Gamma_i), \tag{4.2}$$

where $\Pi_{\text{int},b}(\mathbf{u},\Gamma_{\mathfrak{d}_i})$ is the internal energy stemming from the bulk (fiber and inter-fiber) and $\Pi_{\text{int},c}(\Gamma_i)$ is the dissipative energy associated with cohesive debonding which are addressed in detail in the sequel. The bulk associated energy $\Pi_{\text{int},b}(\mathbf{u},\Gamma_{\mathfrak{d}_i})$ is further decomposed into:

$$\Pi_{\text{int},b}(\mathbf{u},\Gamma_{\mathfrak{d}_i}) = \Pi_{\text{int},FF}(\mathbf{u},\Gamma_{\mathfrak{d}_{IFF}}) + \Pi_{\text{int},IFF}(\mathbf{u},\Gamma_{\mathfrak{d}_{IFF}}), \tag{4.3}$$

where $\Pi_{\text{int},FF}(\mathbf{u},\Gamma_{\mathfrak{d}_{FF}})$ and $\Pi_{\text{int},IFF}(\mathbf{u},\Gamma_{\mathfrak{d}_{IFF}})$ correspond to the energies associated with fiber and inter-fiber, respectively.

With such decomposition at hand, the scheme herein used recalls that the dissipated energy arising from each of the individual failure mechanisms only affects their corresponding counterparts in the elasticity tensor, and therefore precluding the coupling between fiber and inter-fiber failures and each of these failures with respect to the cohesive debonding. Note that, due to this preclusion of interaction between the energies, the elastic energy is strongly coupled with the surface energies stemming from fiber, inter-fiber, and cohesive debonding, whereas surface energies among themselves are only weakly coupled.

In the impending events, the effective Helmholtz free-energy function $\hat{\Psi}$ renders:

$$\hat{\Psi}(\boldsymbol{\varepsilon},\mathbf{A}) = \frac{1}{2}\boldsymbol{\varepsilon} : \mathbb{C}^e : \boldsymbol{\varepsilon}, \tag{4.4}$$

where $\mathbb{C}^e$ is the elastic constitutive tensor defined as:

$$\mathbb{C}^e := \partial_{\boldsymbol{\varepsilon}\boldsymbol{\varepsilon}}\hat{\Psi} = \lambda\mathbf{1}\otimes\mathbf{1} + 2\mu_T\mathbb{I} + \alpha(\mathbf{1}\otimes\mathbf{A} + \mathbf{A}\otimes\mathbf{1}) + 2(\mu_L - \mu_T)\mathbb{I}_A + \beta\mathbf{A}\otimes\mathbf{A}, \tag{4.5}$$

ÁMBITO- PREFIJO
GEISER
Nº registro
O00008744e2000024753

CSV
GEISER-aa34-5f08-a669-4b6e-9258-ed2f-d009-e7f3
DIRECCIÓN DE VALIDACIÓN

FECHA Y HORA DEL DOCUMENTO
19/06/2020 12:08:12 Horario peninsular

GEISER-aa34-5f08-a669-4b6e-9258-ed2f-d009-e7f3

where $\mathbb{I}_{A,ijkl} = A_{im}\mathbb{I}_{jmkl} + A_{jm}\mathbb{I}_{mikl}$ represents the fourth-order identity matrix, and λ, α, β, μ_T and μ_L are the elastic constants taking the form:

$$\lambda = E_{22}\left(\nu_{23} + \nu_{31}\nu_{13}\right)/\mathfrak{D}, \tag{4.6}$$

$$\alpha = E_{22}\left[\nu_{31}\left(1 + \nu_{32} - \nu_{13}\right) - \nu_{32}\right]/\mathfrak{D}, \tag{4.7}$$

$$\beta = E_{11}\left(1 - \nu_{32}\nu_{23}\right)/\mathfrak{D} - E_{22}\left[1 - \nu_{21}\left(\nu_{12} + 2(1 + \nu_{23})\right)\right]/\mathfrak{D} - 4G_{12}, \tag{4.8}$$

$$\mu_L = G_{12} \text{ and } \mu_T = G_{23}, \tag{4.9}$$

with $\mathfrak{D} = 1 - \nu_{32}^2 - 2\nu_{13}\nu_{31} - 2\nu_{32}\nu_{13}\nu_{31}$. The material direction is denoted by $\mathbf{a}$ and $\mathbf{A} = \mathbf{a} \otimes \mathbf{a}$ is the so-called structural tensor.

Here, 1-direction corresponds to the fiber orientation, 2-direction is transverse in-plane orientation with respect to the fiber direction, and 3-direction stands for transverse out-of-plane orientation.

4.2.1 Bulk Energies

In the light of previous developments, the total energy of the fiber can be established as the sum total of the elastic energy and fracture energy associated with the fiber:

$$\begin{aligned}\Pi_{\text{int},FF}(\mathbf{u},\Gamma_{\mathfrak{d}_{FF}}) \approx \Pi_{\text{int},FF}(\mathbf{u},\mathfrak{d}_{FF}) = &\int_{\mathscr{B}}(1-\mathfrak{d}_{FF})^2\hat{\Psi}_{FF}(\boldsymbol{\varepsilon},\mathbf{A})\mathrm{d}\Omega \\ &+ \int_{\mathscr{B}} \mathscr{G}_{c,FF}\left[\frac{1}{2l_{FF}}\mathfrak{d}_{FF}^2 + \frac{l_{FF}}{2}|\nabla\mathfrak{d}_{FF}|^2\right]\mathrm{d}\Omega,\end{aligned} \tag{4.10}$$

where $\hat{\Psi}_{FF}$ is the elastic contribution associated with the fiber: $\hat{\Psi}_{FF} = \frac{1}{2}\boldsymbol{\varepsilon} : \mathbb{C}_{FF}^e : \boldsymbol{\varepsilon}$, where:

$$\mathbb{C}_{FF}^e = \begin{bmatrix} \mathbb{C}_{11}^e & 0 & 0 & 0 & 0 & 0 \\ 0 & 0 & 0 & 0 & 0 & 0 \\ 0 & 0 & 0 & 0 & 0 & 0 \\ 0 & 0 & 0 & 0 & 0 & 0 \\ 0 & 0 & 0 & 0 & 0 & 0 \\ 0 & 0 & 0 & 0 & 0 & 0 \end{bmatrix}, \tag{4.11}$$

and $\mathscr{G}_{c,FF}$ is the fracture energy, and l_{FF} is the material characteristic length associated with fiber failure. This characteristic length is is related to the apparent material strength [93] as:

$$l_{FF} = \frac{27}{256}\frac{E_{11}\mathscr{G}_{c,FF}}{\sigma_{s,FF}^2}, \tag{4.12}$$

where $\sigma_{s,FF}$ is the apparent material strength associated with fiber failure.

Similarly, the inter-fiber contribution to the total internal energy can be expressed as:

$$\begin{aligned}\Pi_{\text{int},IFF}(\mathbf{u},\Gamma_{\mathfrak{d}_{FF}}) \approx \Pi_{\text{int},IFF}(\mathbf{u},\mathfrak{d}_{IFF}) = &\int_{\mathscr{B}}(1-\mathfrak{d}_{IFF})^2\hat{\Psi}_{IFF}(\boldsymbol{\varepsilon},\mathbf{A})\mathrm{d}\Omega \\ &+ \int_{\mathscr{B}} \mathscr{G}_{c,IFF}\left[\frac{1}{2l_{IFF}}\mathfrak{d}_{IFF}^2 + \frac{l_{IFF}}{2}|\nabla\mathfrak{d}_{IFF}|^2\right]\mathrm{d}\Omega,\end{aligned} \tag{4.13}$$

where $\hat{\Psi}_{IFF} = \frac{1}{2}\boldsymbol{\varepsilon} : \mathbb{C}^e_{IFF} : \boldsymbol{\varepsilon}$ is the elastic contribution associated with the inter-fiber failure, and:

$$\mathbb{C}^e_{IFF} = \begin{bmatrix} 0 & \mathbb{C}^e_{12} & \mathbb{C}^e_{13} & 0 & 0 & 0 \\ \mathbb{C}^e_{21} & \mathbb{C}^e_{22} & \mathbb{C}^e_{23} & 0 & 0 & 0 \\ \mathbb{C}^e_{31} & \mathbb{C}^e_{32} & \mathbb{C}^e_{33} & 0 & 0 & 0 \\ 0 & 0 & 0 & \mathbb{C}^e_{44} & 0 & 0 \\ 0 & 0 & 0 & 0 & \mathbb{C}^e_{55} & 0 \\ 0 & 0 & 0 & 0 & 0 & \mathbb{C}^e_{66} \end{bmatrix}, \tag{4.14}$$

where $\mathscr{G}_{c,IFF}$ and l_{IFF} are the fracture energy and corresponding length scale associated with inter-fiber failure, respectively. Similarly, the length scale parameter is estimated for the apparent material strength $\sigma_{s,IFF}$ of inter-fiber failure as:

$$l_{IFF} = \frac{27}{256}\frac{E_{22}\mathscr{G}_{c,IFF}}{\sigma^2_{s,IFF}}. \tag{4.15}$$

Note that with these definitions at hand, the damaged constitutive matrix renders:

$$\mathbb{C}(\mathfrak{d}_{FF}, \mathfrak{d}_{IFF}) = (1-\mathfrak{d}_{FF})^2\mathbb{C}^e_{FF} + (1-\mathfrak{d}_{IFF})^2\mathbb{C}^e_{IFF}, \tag{4.16}$$

$$\mathbb{C}(\mathfrak{d}_{FF}, \mathfrak{d}_{IFF}) = \begin{bmatrix} \mathscr{P}_1\mathbb{C}^e_{11} & \mathscr{P}_2\mathbb{C}^e_{12} & \mathscr{P}_2\mathbb{C}^e_{13} & 0 & 0 & 0 \\ \mathscr{P}_2\mathbb{C}^e_{21} & \mathscr{P}_2\mathbb{C}^e_{22} & \mathscr{P}_2\mathbb{C}^e_{23} & 0 & 0 & 0 \\ \mathscr{P}_2\mathbb{C}^e_{31} & \mathscr{P}_2\mathbb{C}^e_{32} & \mathscr{P}_2\mathbb{C}^e_{33} & 0 & 0 & 0 \\ 0 & 0 & 0 & \mathscr{P}_{12}\mathbb{C}^e_{44} & 0 & 0 \\ 0 & 0 & 0 & 0 & \mathscr{P}_{12}\mathbb{C}^e_{55} & 0 \\ 0 & 0 & 0 & 0 & 0 & \mathscr{P}_2\mathbb{C}^e_{66} \end{bmatrix}, \tag{4.17}$$

where $\mathscr{P}_1 = (1-\mathfrak{d}_{FF})^2$, $\mathscr{P}_2 = (1-\mathfrak{d}_{IFF})^2$, and $\mathscr{P}_{12} = \min(\mathscr{P}_1, \mathscr{P}_2)$.

4.2.2 Interface Energies

The energy stemming from the interface is governed by a bi-linear traction separation law which constitutes of a linear elastic stage characterized by an initial stiffness of K_n, K_{t1} and K_{t2} corresponding to the normal and shear components, respectively, followed by a linear softening as in Figure 4.2. The irreversibility is accounted by introducing a damage variable $\mathfrak{d}_c$ depending on the relative kinematic critical normal and tangential openings, $\mathfrak{g}^f_n$ and $\mathfrak{g}^f_{t_j}$ (j=1 for 2D and j=1,2 for 3D), respectively [50, 51].

The corresponding interface laws governing the normal and tangential tractions $\boldsymbol{\sigma}_n$ and $\boldsymbol{\tau}_{t_j}$, respectively, take the form:

$$\boldsymbol{\sigma}_n = \begin{cases} k_n\mathfrak{g}_n & \text{if } \mathfrak{g}_n \leq \mathfrak{g}^0_n \\ (1-\mathfrak{d}_c)k_n\mathfrak{g}_n & \text{if } \mathfrak{g}^0_n < \mathfrak{g}_n < \mathfrak{g}^f_n \\ 0 & \text{Otherwise} \end{cases}, \tag{4.18}$$

$$\boldsymbol{\tau}_{t_j} = \begin{cases} k_{t_j}\mathfrak{g}_{t_j} & \text{if } \mathfrak{g}_{t_j} \leq \mathfrak{g}^0_{t_j} \\ (1-\mathfrak{d}_c)k_{t_j}\mathfrak{g}_{t_j} & \text{if } \mathfrak{g}^0_{t_j} < \mathfrak{g}_{t_j} < \mathfrak{g}^f_{t_j} \\ 0 & \text{Otherwise} \end{cases}, \tag{4.19}$$

ÁMBITO- PREFIJO
GEISER
Nº registro
O00008744e2000024753
CSV
GEISER-aa34-5f08-a669-4b6e-9258-ed2f-d009-e7f3
DIRECCIÓN DE VALIDACIÓN
FECHA Y HORA DEL DOCUMENTO
19/06/2020 12:08:12 Horario peninsular
GEISER-aa34-5f08-a669-4b6e-9258-ed2f-d009-e7f3

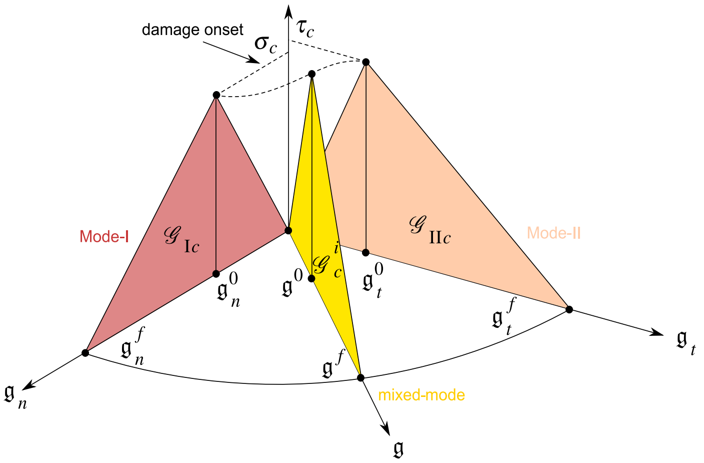

Figure 4.2 Schematic representation of the bi-linear cohesive zone model traction-separation law for mixed-mode.

for each $j = 1{,}2$ to account for the tangential traction, whereas $\mathfrak{g}_n$ and $\mathfrak{g}_{t_j}$ are the relative normal and tangential displacements, respectively. The mixed-mode fracture energy of the interface reads:

$$\mathscr{G}_c^i = \mathscr{G}_{\mathrm{I}c} + (\mathscr{G}_{\mathrm{II}c} - \mathscr{G}_{\mathrm{I}c}) \left(\frac{\mathscr{G}_{\mathrm{II}} + \mathscr{G}_{\mathrm{III}}}{\mathscr{G}_{\mathrm{I}} + \mathscr{G}_{\mathrm{II}} + \mathscr{G}_{\mathrm{III}}} \right)^{\eta}, \tag{4.20}$$

where $\mathscr{G}_{\mathrm{I}c}$, $\mathscr{G}_{\mathrm{II}c}$, and $\mathscr{G}_{\mathrm{III}c}$ represent the corresponding fracture energy associated with normal (Mode I) and shear (Mode II and III), respectively, and computed as the area under the traction separation curve, η identifies an experimental fitting parameter elucidating the effects of fracture mode mixities [144]. Finally, $\mathscr{G}_{\mathrm{I}}$, $\mathscr{G}_{\mathrm{II}}$, and $\mathscr{G}_{\mathrm{III}}$ are energy release rates associated with Mode I, Mode II, and III, respectively. Based on the energy considerations, the evolution of the damage variable $\mathfrak{d}_c$ is estimated based on the effective displacement $\mathfrak{g}_m = \sqrt{\langle \mathfrak{g}_n \rangle^2 + \mathfrak{g}_{t_1}^2 + \mathfrak{g}_{t_2}^2}$, as:

$$\mathfrak{d}_c = \frac{\mathfrak{g}_m^f (\mathfrak{g}_m^{\max} - \mathfrak{g}_m^0)}{\mathfrak{g}_m^{\max} (\mathfrak{g}_m^f - \mathfrak{g}_m^0)}, \tag{4.21}$$

where $\mathfrak{g}_m^0$ and $\mathfrak{g}_m^f$ are the effective displacements at failure initiation and at complete failure, respectively, $\mathfrak{g}_m^{\max}$ refers to the maximum value of effective displacement during loading history. Finally, with this at hand, the corresponding total energy generated by the cohesive interface takes the form:

$$\Pi_{\mathrm{int},c}(\Gamma_i) \approx \Pi_{\mathrm{int},c}(\mathfrak{d}_c) = \int_{\Gamma_i} \mathscr{G}_c^i(\mathfrak{g}, \mathfrak{d}_c)\,\mathrm{d}\mathscr{S}. \tag{4.22}$$

4.2.3 Fundamentals of Puck Failure Criterion

Damage evolution in the bulk relies on the Puck theory of failure [124] whose corresponding failure criterion accounts for the independent assessment of fiber and inter-fiber failure surfaces. For the fiber failure, with usual notations, that is $\parallel$ (subscript 1), $\perp$ (subscript 2 and subscript 3) representing fiber direction, normal to the fiber direction in-plane and, normal to the fiber direction out-of-plane, respectively, for the ply co-ordinates in a local setting $0 - \mathbf{e}_1 - \mathbf{e}_2 - \mathbf{e}_3$.

ÁMBITO- PREFIJO
GEISER
Nº registro
O00008744e2000024753
CSV
GEISER-aa34-5f08-a669-4b6e-9258-ed2f-d009-e7f3
DIRECCIÓN DE VALIDACIÓN
FECHA Y HORA DEL DOCUMENTO
19/06/2020 12:08:12 Horario peninsular
GEISER-aa34-5f08-a669-4b6e-9258-ed2f-d009-e7f3

According to the Puck theory, fiber failure is triggered based on energetic considerations that, the exposure factor (denoted $f_{E,FF+}$ for tensile loading and $f_{E,FF-}$ for compressive loading) reaches the value 1:

$$f_{E,FF+} = \frac{1}{R^t_{\parallel}}\left[\sigma_{11} - \left(\nu_{\perp\parallel} - \frac{E_{\parallel}}{E_{\parallel f}}\nu_{\perp\parallel f}\right)(\sigma_{22}+\sigma_{33})\mathscr{P}_2\right], \tag{4.23}$$

$$f_{E,FF-} = \sqrt{\left(\frac{1}{R^c_{\parallel}}\left[\sigma_{11} - \left(\nu_{\perp\parallel} - \frac{E_{\parallel}}{E_{\parallel f}}\nu_{\perp\parallel f}m_{\sigma f}\right)\mathscr{P}_2(\sigma_{22}+\sigma_{33})\right]\right)^2 + \kappa\left(\frac{\sigma_{12}^2+\sigma_{13}^2}{R^2_{\perp\parallel}}\right)}, \tag{4.24}$$

where $R^t_{\parallel}$ stands for the tensile longitudinal strength in fiber direction. $\nu_{\perp\parallel}$ and $\nu_{\perp\parallel f}$ identify the major Poisson's ratios of the ply and the fibers, respectively, and $E_{\parallel f}$ is the elastic modulus of the fibers. Moreover, $R^c_{\parallel}$ is the compressive longitudinal strength in fiber direction, $R_{\perp\parallel}$ represents the in-plane shear strength, and $m_{\sigma f}$ stands for the so-called magnification factor, which is assumed to take the values 1.1 for CFRP and 1.3 for GFRP [131]. The incorporation of $\mathscr{P}_2$ is to scale the influence of the transverse stress components on the longitudinal stress (lateral contraction) with respect to the state of matrix damage. It is assumed that the contraction in the longitudinal direction due to transverse stress will vanish in a case $\mathscr{P}_2 \to 1$, i.e. matrix rupture parallel to the fibers. In the case of compressive longitudinal stress, reduced compressive longitudinal fracture resistance of the plies is assumed in case of increasing shear stress, see [132–136]. The parameter κ allows controlling the influence of shear stresses on the failure of the fibers under compression. In the case of lateral constraint $\kappa = 0$, because even in case of a crushed matrix the fibers are assumed to be kept inline by the lateral constraint. In case of absent lateral constrains $\kappa \geq 0$, since a crushed matrix will promote fiber kinking and will, therefore, reduce the compressive load capacities in fiber direction [132–136].

Puck theory also distinguishes the inter-fiber failure by introducing the so-called action plane [124, 131], which corresponds to identifying the potential fracture plane derived from the maximum stress states. The determination of the fracture plane is usually performed via the assessment of the most critical stress state in terms of the local components by calculating the value of $F_{E,IFF}$ for all angles Θ within the interval of $-90^\circ \leq \Theta \leq +90^\circ$, using an increment of one degree. The transformation from the local ply setting to the action plane system yields:

$$\begin{bmatrix} \sigma_n(\Theta) \\ \tau_{nt}(\Theta) \\ \tau_{n1}(\Theta) \end{bmatrix} = \begin{bmatrix} \cos^2\Theta & \sin^2\Theta & 2\cos\Theta\sin\Theta & 0 & 0 \\ -\cos\Theta\sin\Theta & \cos\Theta\sin\Theta & \cos^2\Theta - \sin^2\Theta & 0 & 0 \\ 0 & 0 & 0 & \sin\Theta & \cos\Theta \end{bmatrix} \begin{bmatrix} \sigma_{22} \\ \sigma_{33} \\ \sigma_{23} \\ \sigma_{13} \\ \sigma_{12} \end{bmatrix}. \tag{4.25}$$

ÁMBITO- PREFIJO
GEISER
Nº registro
O00008744e2000024753
CSV
GEISER-aa34-5f08-a669-4b6e-9258-ed2f-d009-e7f3
DIRECCIÓN DE VALIDACIÓN
FECHA Y HORA DEL DOCUMENTO
19/06/2020 12:08:12 Horario peninsular
GEISER-aa34-5f08-a669-4b6e-9258-ed2f-d009-e7f3

In particular, the expression for inter-fiber failure under tensile and compressive loading conditions on the action plane takes the form:

$$f_{E,IFF+}(\Theta) = \left[\sqrt{\left[\left(\frac{1}{R^{At}_{\perp}} - \frac{p^{t}_{\perp\psi}}{R^{A}_{\perp\psi}} \right) \sigma_n(\Theta) \right]^2 + \left(\frac{\tau_{nt}(\Theta)}{R^{A}_{\perp\perp}} \right)^2 + \left(\frac{\tau_{n1}(\Theta)}{R^{A}_{\parallel\perp}} \right)^2} + \frac{p^{t}_{\perp\psi}}{R^{A}_{\perp\psi}} \sigma_n(\Theta) \right] \frac{1}{\eta_w} \text{ for } \sigma_n(\Theta) \geq 0, \tag{4.26}$$

$$f_{E,IFF-}(\Theta) = \left[\sqrt{\left(\frac{p^{c}_{\perp\psi}}{R^{A}_{\perp\psi}} \sigma_n(\Theta) \right)^2 + \left(\frac{\tau_{nt}(\Theta)}{R^{A}_{\perp\perp}} \right)^2 + \left(\frac{\tau_{n1}(\Theta)}{R^{A}_{\parallel\perp}} \right)^2} + \frac{p^{c}_{\perp\psi}}{R^{A}_{\perp\psi}} \sigma_n(\Theta) \right] \frac{1}{\eta_w} \text{ for } \sigma_n(\Theta) < 0. \tag{4.27}$$

In the previous expressions, η_w accounts for the influence of the exposure factor in fiber direction on the inter-fiber failure due to lateral contraction, as long as no fiber failure occurred [132, 134]. Moreover, one can identify $R^{At}_{\perp} = R^{t}_{\perp}$, $R^{A}_{\perp\parallel} = R_{\perp\parallel}$, where $R^{t}_{\perp}$ represents the transverse tensile strength. Also, the fracture strength $R^{A}_{\perp\perp}$ is given by:

$$R^{A}_{\perp\perp} = \frac{R^{c}_{\perp}}{2\left(1 + p^{c}_{\perp\perp}\right)}, \tag{4.28}$$

where $R^{c}_{\perp}$ represents the transverse compressive strength of the ply. The definitions of the inclination parameters $p^{t}_{\perp\psi}$ and $p^{c}_{\perp\psi}$ at any angle ψ are given by the following relations, respectively:

$$\frac{p^{t}_{\perp\psi}}{R^{A}_{\perp\psi}} = \frac{p^{t}_{\perp\perp}}{R^{A}_{\perp\perp}} \cos^2\psi + \frac{p^{t}_{\perp\parallel}}{R^{A}_{\perp\parallel}} \sin^2\psi \text{ and } \frac{p^{c}_{\perp\psi}}{R^{A}_{\perp\psi}} = \frac{p^{c}_{\perp\perp}}{R^{A}_{\perp\perp}} \cos^2\psi + \frac{p^{c}\perp\parallel}{R^{A}_{\perp\parallel}} \sin^2\psi, \tag{4.29}$$

with:

$$R^{A}_{\perp\psi} = \left[\left(\frac{\cos\psi}{R^{A}_{\perp\perp}} \right)^2 + \left(\frac{\sin\psi}{R^{A}_{\perp\parallel}} \right)^2 \right]. \tag{4.30}$$

The trigonometric terms defined as:

$$\cos^2\psi = \frac{\tau^2_{nt}}{\tau^2_{nt} + \tau^2_{n1}} \text{ and } \sin^2\psi = \frac{\tau^2_{n1}}{\tau^2_{nt} + \tau^2_{n1}}. \tag{4.31}$$

Finally, recommended values of material-dependent inclination parameters $p^{t}_{\perp\perp}$, $p^{c}_{\perp\perp}$, $p^{t}_{\perp\parallel}$, and $p^{c}_{\perp\parallel}$ are reported in Table 4.1 for glass fiber reinforced (GFRP) and carbon fiber reinforced (CFRP) composites.

Due to the modelling assumptions herein made, the proposed model requires the following fracture energy values: (i) $\mathscr{G}_{c,FF}$ fiber fracture energy, (ii) $\mathscr{G}_{c,IFF}$ matrix-dominated fracture energy, and (iii) $\mathscr{G}_{c}$ inter-laminar fracture energy. These properties can be determined via experimental procedures, see [142, 166–168] and the references therein.

ÁMBITO- PREFIJO
GEISER
Nº registro
O00008744e2000024753
CSV
GEISER-aa34-5f08-a669-4b6e-9258-ed2f-d009-e7f3
DIRECCIÓN DE VALIDACIÓN
FECHA Y HORA DEL DOCUMENTO
19/06/2020 12:08:12 Horario peninsular
GEISER-aa34-5f08-a669-4b6e-9258-ed2f-d009-e7f3

Table 4.1 Recommended inclination factors for CFRP and GFRP composites.

Material	$p^t_{\perp\perp}$	$p^c_{\perp\perp}$	$p^t_{\perp\parallel}$	$p^c_{\perp\parallel}$
GFRP	0.30	0.25	0.20	0.25
CFRP	0.35	0.30	0.25	0.30

4.3 Variational Formulation and Strong Forms

Relying on the considerations given in Section 4.2, the total energy functional of the solid body $\mathscr{B}$, along with the cracks Γ_i and $\Gamma_{\mathfrak{d}_i}$ at any arbitrary instance $t \in [0,T]$ takes the form:

$$\Pi(\mathbf{u},\Gamma) \approx \Pi(\mathbf{u},\mathfrak{d}_i,\mathfrak{d}_c) = \Pi_{\text{int}}(\mathbf{u},\mathfrak{d}_i,\mathfrak{d}_c) + \Pi_{\text{ext}}(\mathbf{u}), \tag{4.32}$$

where the internal and external contribution to the energy functional $\Pi(\mathbf{u},\mathfrak{d}_i,\mathfrak{d}_c)$ read, respectively:

$$\begin{aligned}
\Pi_{\text{int}}(\mathbf{u},\mathfrak{d}_i,\mathfrak{d}_c) = &\int_{\mathscr{B}} (1-\mathfrak{d}_{FF})^2\hat{\Psi}_{FF}(\boldsymbol{\varepsilon},\mathbf{A}) + (1-\mathfrak{d}_{IFF})^2\hat{\Psi}_{IFF}(\boldsymbol{\varepsilon},\mathbf{A})\mathrm{d}\Omega \\
&+ \int_{\mathscr{B}} \mathscr{G}_{c,FF}\left[\frac{1}{2l_{FF}}\mathfrak{d}^2_{FF} + \frac{l_{FF}}{2}|\nabla\mathfrak{d}_{FF}|^2\right] + \mathscr{G}_{c,IFF}\left[\frac{1}{2l_{IFF}}\mathfrak{d}^2_{IFF} + \frac{l_{IFF}}{2}|\nabla\mathfrak{d}_{IFF}|^2\right]\mathrm{d}\Omega \\
&+ \int_{\Gamma_i} \mathscr{G}^i_c(\mathfrak{g},\mathfrak{d}_c)\mathrm{d}\mathscr{S},
\end{aligned} \tag{4.33}$$

$$\Pi_{\text{ext}}(\mathbf{u}) = -\int_{\mathscr{B}} \mathbf{f}_v \mathrm{d}\Omega - \int_{\partial\mathscr{B}_t} \bar{\mathbf{t}}\mathrm{d}\partial\Omega, \tag{4.34}$$

where $\mathbf{f}_v$ is the deformation-independent volume-specific loads.

Following the standard Bubnov-Galerkin method, the four primary fields with:

$$\mathbf{u} \in \mathscr{U}_u := \left\{\mathbf{u} \in H^1(\mathscr{B}) | \nabla\mathbf{u} \in L^2(\mathscr{B});\ \mathbf{u} = \bar{\mathbf{u}} \text{ on } \partial\mathscr{B}_u\right\},$$

$$\mathfrak{d}_{FF} \in \mathscr{U}_{\mathfrak{d}_{FF}} := \left\{\mathfrak{d}_{FF} \in H^1(\mathscr{B}) | \mathfrak{d}_{FF}(\mathbf{x}) \in [0,1],\ \dot{\mathfrak{d}}_{FF} \geq 0,\ \forall\mathbf{x} \in \mathscr{B}\right\},$$

$$\mathfrak{d}_{IFF} \in \mathscr{U}_{\mathfrak{d}_{IFF}} := \left\{\mathfrak{d}_{IFF} \in H^1(\mathscr{B}) | \mathfrak{d}_{IFF}(\mathbf{x}) \in [0,1],\ \dot{\mathfrak{d}}_{IFF} \geq 0,\ \forall\mathbf{x} \in \mathscr{B}\right\},$$

$$\mathfrak{d}_c \in \mathscr{U}_{\mathfrak{d}_c} := \left\{\mathfrak{d}_c \in H^1(\mathscr{B}) | \mathfrak{d}_c(\mathbf{x}) \in [0,1],\ \dot{\mathfrak{d}}_c \geq 0,\ \forall\mathbf{x} \in \Gamma_i\right\},$$

are extended by the corresponding test functions:

$$\delta\mathbf{u} \in \mathscr{V}_u := \left\{\delta\mathbf{u} \in H^1(\mathscr{B}) | \nabla\delta\mathbf{u} \in L^2(\mathscr{B});\ \delta\mathbf{u} = \mathbf{0} \text{ on } \partial\mathscr{B}_u\right\},$$

$$\delta\mathfrak{d}_{FF} \in \mathscr{V}_{\mathfrak{d}_{FF}} := \left\{\delta\mathfrak{d} \in H^1(\mathscr{B}) | \delta\mathfrak{d}_{FF} \geq 0, \forall\mathbf{x} \in \mathscr{B}\right\},$$

$$\delta\mathfrak{d}_{IFF} \in \mathscr{V}_{\mathfrak{d}_{IFF}} := \left\{\delta\mathfrak{d} \in H^1(\mathscr{B}) | \delta\mathfrak{d}_{IFF} \geq 0, \forall\mathbf{x} \in \mathscr{B}\right\},$$

$$\delta\mathfrak{d}_c \in \mathscr{V}_{\mathfrak{d}_c} := \left\{\delta\mathfrak{d} \in H^1(\mathscr{B}) | \delta\mathfrak{d}_c \geq 0, \forall\mathbf{x} \in \Gamma_i\right\},$$

ÁMBITO- PREFIJO
GEISER
Nº registro
O00008744e2000024753
CSV
GEISER-aa34-5f08-a669-4b6e-9258-ed2f-d009-e7f3
DIRECCIÓN DE VALIDACIÓN
FECHA Y HORA DEL DOCUMENTO
19/06/2020 12:08:12 Horario peninsular
GEISER-aa34-5f08-a669-4b6e-9258-ed2f-d009-e7f3

where H^1 denotes the Sobolev space. There accordingly, the weak form of the coupled displacement-crack phase-field-cohesive zone problem is constructed as:

$$\delta\Pi(\mathbf{u},\mathfrak{d}_i,\mathfrak{d}_c,\delta\mathbf{u},\delta\mathfrak{d}_i,\delta\mathfrak{d}_c) = \delta\Pi_{\text{int}}(\mathbf{u},\mathfrak{d}_i,\mathfrak{d}_c,\delta\mathbf{u},\delta\mathfrak{d}_i,\delta\mathfrak{d}_c) + \delta\Pi_{\text{ext}}(\mathbf{u},\delta\mathbf{u}) = 0. \tag{4.35}$$

Moreover, after simplifications, the strong form of the field equations can be reduced to the following:

$$\mathrm{div}\boldsymbol{\sigma} + \mathbf{f}_v = \mathbf{0} \text{ in } \mathscr{B} \text{ and } \boldsymbol{\sigma}\cdot\mathbf{n} = \bar{\mathbf{t}} \text{ on } \partial\mathscr{B}_t, \tag{4.36}$$

$$2(1-\mathfrak{d}_{FF})\mathfrak{P}_{FF}\mathscr{H}_{FF} = \mathscr{G}_{c,FF}\,\delta_{\mathfrak{d}_{FF}}\gamma(\mathfrak{d}_{FF},\nabla\mathfrak{d}_{FF}) \text{ in } \mathscr{B} \text{ and } \nabla\mathfrak{d}_{FF}\cdot\mathbf{n} = 0 \text{ on } \partial\mathscr{B}, \tag{4.37}$$

$$2(1-\mathfrak{d}_{IFF})\mathfrak{P}_{IFF}\mathscr{H}_{IFF} = \mathscr{G}_{c,IFF}\,\delta_{\mathfrak{d}_{IFF}}\gamma(\mathfrak{d}_{IFF},\nabla\mathfrak{d}_{IFF}) \text{ in } \mathscr{B} \text{ and } \nabla\mathfrak{d}_{IFF}\cdot\mathbf{n} = 0 \text{ on } \partial\mathscr{B}, \tag{4.38}$$

$$\mathrm{div}_{\mathfrak{g}}\left[\boldsymbol{\sigma}_n(\mathfrak{d}_c) + \tau_n(\mathfrak{d}_c)\right] = 0 \quad \text{in } \Gamma_i, \tag{4.39}$$

where in the previous expressions div[•] represents the divergence operator and γ is the so-called crack density functional. The terms $\mathscr{H}_{FF}$ and $\mathscr{H}_{IFF}$ are the crack driving forces related to fiber and inter-fiber failure, respectively. Herein, $\mathfrak{P}_{FF}$ and $\mathfrak{P}_{IFF}$ are activation flags for the current crack driving forces for fiber and inter-fiber failure, respectively, and are activated if and only if their respective Puck failure criterion has been met. In accordance with the Pucks failure criteria, the crack driving force of each $j = FF,IFF$ are given by:

$$\mathscr{H}_j = \xi_j \left[\left\langle \frac{\max\limits_{\tau\in[0,t]} \hat{\Psi}_j(\tau)}{\hat{\Psi}_{\text{init},j}} - 1 \right\rangle_+ \right], \tag{4.40}$$

where ξ_j is a dimensionless parameter that characterizes the damage activation and post peak behaviors. $\hat{\Psi}_{\text{init},j}$ is the effective elastic energy for damage initiation in each of $j = FF,IFF$.

The unilateral stationary condition of the total internal energy functional implies that $\delta\Pi_{\text{int}} = 0$ for all $(\delta\mathbf{u},\delta\mathfrak{d}_{FF},\delta\mathfrak{d}_{IFF},\delta\mathfrak{g}) > 0$ and $\delta\Pi_{\text{int}} > 0$ for $(\delta\mathbf{u},\delta\mathfrak{d}_{FF},\delta\mathfrak{d}_{IFF},\delta\mathfrak{g}) = 0$ along with the irriversibility and boundedness of $\mathfrak{d}_{FF}$, $\mathfrak{d}_{IFF}$, and $\mathfrak{d}_c$ leads to the first-order optimality (KKT) conditions for the quasi-static evolution [14, 47].

It is worth noting that the irreversible character of the phase-fields and cohesive zone can be reduced to $\mathscr{S}$, this is fulfilled by the history variable embedded by the history variable Eq.(4.40). The boundedness of the phase-field variables $\mathfrak{d}_{FF}$ and $\mathfrak{d}_{IFF} \in [0,1]$ is ensured due to the choice of degradation function $(1-\mathfrak{d}_j)^2$ as in [43]. Also, it is important to note that, we have assumed $\nabla\mathfrak{d}_j = 0$ due to the compactness property and $\delta\mathbf{u} = 0$ on $\partial\mathscr{B}_t$ and $\delta\mathfrak{d}_j = 0$ on $\partial\mathscr{B}$, from the variational form which are reflected in the choice of approximate spaces of test functions, see [164, 165].

4.4 Finite Element Implementation

In this section, details of the finite element implementation of the proposed model are outlined. A staggered solution scheme is used to solve the system of coupled Partial Differential Equations

ÁMBITO- PREFIJO
GEISER
Nº registro
O00008744e2000024753
CSV
GEISER-aa34-5f08-a669-4b6e-9258-ed2f-d009-e7f3
DIRECCIÓN DE VALIDACIÓN
FECHA Y HORA DEL DOCUMENTO
19/06/2020 12:08:12 Horario peninsular
GEISER-aa34-5f08-a669-4b6e-9258-ed2f-d009-e7f3

(PDEs) using an alternating minimization scheme [15].

The solution of the proposed displacement multi phase-field-cohesive zone fracture problem is obtained after discretizing the space using the Finite Element Method (FEM). Hence, the continuous domain of the body $\mathscr{B}$ is approximated by a discrete domain $\mathscr{B}^h$ that is formed by a finite number of disjoints elements $\mathscr{B}^e$. There accordingly, the infinite-dimensional function spaces $\mathscr{U}$ and $\mathscr{V}$ are approximated by the corresponding finite-dimensional subspaces $\mathscr{U}^h$ and $\mathscr{V}^h$, imposing the same conditions on the boundaries.

At each element level, in the isoparamtric space settings, the triplet of field variables $\{\mathbf{u}^e, \mathfrak{d}^e_{FF}, \mathfrak{d}^e_{IFF}\}$ as well as their variations $\{\delta\mathbf{u}^e, \delta\mathfrak{d}^e_{FF}, \delta\mathfrak{d}^e_{IFF}\}$ are approximated using linear first-order Lagrangian triplet of shape functions $\left\{\mathbf{N}^u_i, \mathbf{N}^{\mathfrak{d}}_i, \mathbf{N}^{\mathfrak{d}}_i\right\}$ at i^{th} node of each element satisfying partition of unity, as follows:

$$\mathbf{u}^e = \sum_{i=1}^{\mathbf{N}_{\text{node}}} \mathbf{N}^u_i \mathbf{u}^e_i, \quad \mathfrak{d}^e_j = \sum_{i=1}^{\mathbf{N}_{\text{node}}} \mathbf{N}^{\mathfrak{d}}_i \mathfrak{d}^e_{j,i} \tag{4.41}$$

$$\delta\mathbf{u}^e = \sum_{i=1}^{\mathbf{N}_{\text{node}}} \mathbf{N}^u_i \delta\mathbf{u}^e_i, \quad \delta\mathfrak{d}^e_j = \sum_{i=1}^{\mathbf{N}_{\text{node}}} \mathbf{N}^{\mathfrak{d}}_i \delta\mathfrak{d}^e_{j,i} \quad \text{for each } j = FF, IFF. \tag{4.42}$$

The triplet of spatial derivatives $\{\nabla\mathbf{u}^e, \nabla\mathfrak{d}^e_{FF}, \nabla\mathfrak{d}^e_{IFF}\}$ are approximated using the gradients of the shape functions $\left\{\mathbf{B}^u_i, \mathbf{B}^{\mathfrak{d}}_i, \mathbf{B}^{\mathfrak{d}}_i\right\}$ at i^{th} node of each element following:

$$\boldsymbol{\varepsilon}^e = \sum_{i=1}^{\mathbf{N}_{\text{node}}} \mathbf{B}^u_i \mathbf{u}^e_i, \quad \nabla\mathfrak{d}^e_j = \sum_{i=1}^{\mathbf{N}_{\text{node}}} \mathbf{B}^{\mathfrak{d}}_i \mathfrak{d}^e_{j,i},$$

$$\delta\boldsymbol{\varepsilon}^e = \sum_{i=1}^{\mathbf{N}_{\text{node}}} \mathbf{B}^u_i \delta\mathbf{u}^e_i, \quad \nabla\delta\mathfrak{d}^e_j = \sum_{i=1}^{\mathbf{N}_{\text{node}}} \mathbf{B}^{\mathfrak{d}}_i \delta\mathfrak{d}^e_{j,i}, \quad \text{for each } j = FF, IFF.$$

Complying with the formulation of interface cohesive element, the displacement jump vector $\mathfrak{g}$ is represented in terms of local frames across the interface Γ_i [58]. Hence, the jump $\mathfrak{g}$ and its variation $\delta\mathfrak{g}$ is approximated using the kinematic jump-displacement operator $\mathbf{B}^{\mathfrak{g}} = R\mathbf{N}^{\mathfrak{g}}L$ as:

$$\mathfrak{g}^e = \mathbf{B}^{\mathfrak{g}}\mathbf{u}^e L, \quad \delta\mathfrak{g}^e = \mathbf{B}^{\mathfrak{g}}\delta\mathbf{u}^e L, \tag{4.43}$$

where L is the difference between the displacement of the upper and lower interface points and R is a rotation matrix that converts integration points from global to the local frame, and $\mathbf{N}_{\mathfrak{g}}$ represents the standard cohesive shape function, see [51].

The discrete elemental residual vectors for the quadruplet $\{\mathbf{u}^e, \mathfrak{d}^e_{FF}, \mathfrak{d}^e_{IFF}, \mathfrak{g}^e\}$ can be reduced to the following system of equations:

$$\begin{aligned}\mathscr{R}^{\mathbf{u}}_e = &\int_{\mathscr{B}^e} (1-\mathfrak{d}_{FF})^2 (\mathbf{B}^u)^T \boldsymbol{\sigma}_{FF} + (1-\mathfrak{d}_{IFF})^2 (\mathbf{B}^u)^T \boldsymbol{\sigma}_{IFF} \mathrm{d}\Omega - \int_{\mathscr{B}^e} (\mathbf{N}^u)^T \mathbf{f}_v \mathrm{d}\Omega \\ &- \int_{\partial\mathscr{B}^e_t} (\mathbf{N}^u)^T \bar{\mathbf{t}} \mathrm{d}\partial\Omega + \mathscr{R}^{\mathfrak{g}}_e,\end{aligned} \tag{4.44}$$

$$\mathscr{R}^{\mathfrak{d}_{FF}}_e = \int_{\mathscr{B}^e} \left[\frac{\mathscr{G}_{c,FF}}{l_{FF}} \mathfrak{d}_{FF} - 2(1-\mathfrak{d}_{FF})\mathfrak{P}_{FF}\mathscr{H}_{FF}\right] (N^{\mathfrak{d}})^T + \mathscr{G}_{c,FF} l_{FF} (\mathbf{B}^{\mathfrak{d}})^T \nabla\mathfrak{d}_{FF} \mathrm{d}\Omega, \tag{4.45}$$

ÁMBITO- PREFIJO
GEISER
Nº registro
O00008744e2000024753

CSV
GEISER-aa34-5f08-a669-4b6e-9258-ed2f-d009-e7f3
DIRECCIÓN DE VALIDACIÓN

FECHA Y HORA DEL DOCUMENTO
19/06/2020 12:08:12 Horario peninsular

GEISER-aa34-5f08-a669-4b6e-9258-ed2f-d009-e7f3

$$\mathscr{R}_e^{\mathfrak{d}_{IFF}} = \int_{\mathscr{B}^e} \left[\frac{\mathscr{G}_{c,IFF}}{l_{IFF}} \mathfrak{d}_{IFF} - 2(1-\mathfrak{d}_{IFF}) \mathfrak{P}_{IFF} \mathscr{H}_{IFF} \right] (N^{\mathfrak{d}})^T + \mathscr{G}_{c,IFF} l_{IFF} (\mathbf{B}^{\mathfrak{d}})^T \nabla \mathfrak{d}_{IFF} \mathrm{d}\Omega. \tag{4.46}$$

where,

$$\mathscr{R}_e^{\mathfrak{g}} = \int_{\Gamma_i^e} (\mathbf{B}^{\mathfrak{g}})^T \tau(\mathfrak{g},\mathfrak{d}_c) \mathrm{d}\mathscr{S}, \tag{4.47}$$

is the residual vector associated with the cohesive interface. It is clear that the displacement field $\mathbf{u}$ is strongly coupled with the phase-fields $\mathfrak{d}_{FF}$, $\mathfrak{d}_{IFF}$, and the displacement the jump $\mathfrak{g}$. Whereas, the phase-fields are among themselves and with the jump $\mathfrak{g}$ are decoupled which are evident from Eqs.(4.37)-(4.39) and from the assumption that $\Gamma_i \cap \Gamma_{\mathfrak{d}_t} = \emptyset$. Due to the existence of multiple phase-field and interface, the system of equations describing the fracture is non-linear. Hence, an iterative Newton-Raphson solver is used until the convergence in the sense of cauchy sequence $[(\mathbf{u}_n^{t+1} - \mathbf{u}_n^t)]$ is reached. Here, $\mathbf{u}_n^t$ is the t^{th} iteration at n^{th} step. The corresponding Newton-Raphson iteration to estimate $(n+1)$ time step tales the form:

$$\begin{bmatrix} \mathbf{u} \\ \mathfrak{d}_{FF} \\ \mathfrak{d}_{IFF} \end{bmatrix}_{n+1} = \begin{bmatrix} \mathbf{u} \\ \mathfrak{d}_{FF} \\ \mathfrak{d}_{IFF} \end{bmatrix}_{n} - \begin{bmatrix} \mathscr{K}^{\mathbf{uu}} + \mathscr{K}^{\mathfrak{gg}} & 0 & 0 \\ 0 & \mathscr{K}^{\mathfrak{d}_{FF}\mathfrak{d}_{FF}} & 0 \\ 0 & 0 & \mathscr{K}^{\mathfrak{d}_{IFF}\mathfrak{d}_{IFF}} \end{bmatrix}_{n+1}^{-1} \begin{bmatrix} \mathscr{R}^{u} \\ \mathscr{R}^{\mathfrak{d}_{FF}} \\ \mathscr{R}^{\mathfrak{d}_{IFF}} \end{bmatrix}_{n}, \tag{4.48}$$

where the corresponding element stiffness matrices read:

$$\mathscr{K}_e^{\mathbf{uu}} := \frac{\partial \mathscr{R}_e^{\mathbf{u}}}{\partial \mathbf{u}^e} = \int_{\mathscr{B}^e} (\mathbf{B}^u)^T \mathbb{C}^{ep\mathfrak{d}} \mathbf{B}^u \mathrm{d}\Omega, \tag{4.49}$$

$$\mathscr{K}_e^{\mathfrak{gg}} := \frac{\partial \mathscr{R}_e^{\mathfrak{g}}}{\partial \mathbf{u}^e} = \int_{\Gamma_i^e} (\mathbf{B}^{\mathfrak{g}})^T \partial_{\mathfrak{g}} \tau \mathbf{B}^{\mathfrak{g}} \mathrm{d}\mathscr{S},$$

$$\mathscr{K}_e^{\mathfrak{d}_{FF}\mathfrak{d}_{FF}} := \frac{\partial \mathscr{R}_e^{\mathfrak{d}_{FF}}}{\partial \mathfrak{d}_{FF}^e} = \int_{\mathscr{B}^e} \left[\frac{\mathscr{G}_{c,FF}}{l_{FF}} + 2\mathfrak{P}_{FF} \mathscr{H}_{IFF} \right] \mathbf{N}^{\mathfrak{d}} (\mathbf{N}^{\mathfrak{d}})^T + \mathscr{G}_{c,FF} l_{FF} (\mathbf{B}^{\mathfrak{d}})^T \mathbf{B}^{\mathfrak{d}} \mathrm{d}\Omega, \tag{4.50}$$

$$\mathscr{K}_e^{\mathfrak{d}_{IFF}\mathfrak{d}_{IFF}} := \frac{\partial \mathscr{R}_e^{\mathfrak{d}_{IFF}}}{\partial \mathfrak{d}_{IFF}^e} = \int_{\mathscr{B}^e} \left[\frac{\mathscr{G}_{c,IFF}}{l_{IFF}} + 2\mathfrak{P}_{IFF} \mathscr{H}_{IFF} \right] \mathbf{N}^{\mathfrak{d}} (\mathbf{N}^{\mathfrak{d}})^T + \mathscr{G}_{c,IFF} l_{IFF} (\mathbf{B}^{\mathfrak{d}})^T \mathbf{B}^{\mathfrak{d}} \mathrm{d}\Omega, \tag{4.51}$$

and $\mathbb{C}^{ep\mathfrak{d}}$ is the material consistent tangent.

The previous non-linear system of equations is implemented in the finite element software `ABAQUS`. For this purpose, a user-defined `UMAT` is written for the solution of equilibrium equations associated with the displacement field whereas `UEL` is utilized for solving the fracture associated problem.

4.5 Representative Examples

In this section, a comprehensive numerical analysis is presented to validate the model against experimental results in order to draw a qualitative assessment of delamination migration. In

ÁMBITO- PREFIJO
GEISER
Nº registro
O00008744e2000024753
CSV
GEISER-aa34-5f08-a669-4b6e-9258-ed2f-d009-e7f3
DIRECCIÓN DE VALIDACIÓN
FECHA Y HORA DEL DOCUMENTO
19/06/2020 12:08:12 Horario peninsular
GEISER-aa34-5f08-a669-4b6e-9258-ed2f-d009-e7f3

the sequel, a holistic sensitivity analysis is carried out by means of the variation of the loading application point, ply angle, and initial pre-crack length.

4.5.1 Description of the Numerical Model: General Aspects

Figure 4.3 depicts the baseline configuration under investigation herein. The corresponding numerical model consists of 44 cross-ply IM7/8552 laminates with the layup sequence $[90^\circ_4/0^\circ_3/(90^\circ/0^\circ)_{2s}/0^\circ_3/CL/90^\circ_4/CL/0^\circ/0^\circ/(90^\circ/0^\circ)_{2s}/0^\circ/0^\circ/90^\circ_3/0^\circ/90^\circ]$, where CL refers to a cohesive layer. Each ply has a thickness of 0.125mm. Compared with the experimental sequence as in [151], a PTFE (Polytetrafluoroethylene) layer is replaced by a cohesive layer and in addition, another cohesive layer is added at the interface between the 90°_4 and 0° sequence in order to account for delamination migration.

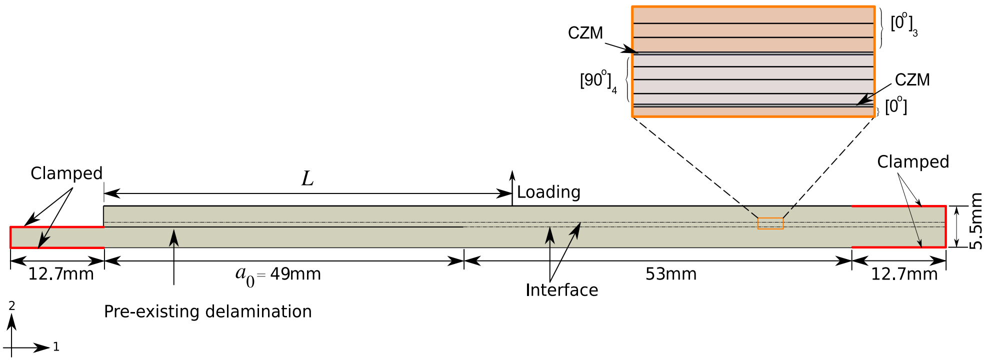

Figure 4.3 Schematic representation of the delamination migration model.

It is evident from the experimental results reported in [152] that, when shear stresses in the model change sign, migration/kinking occurs and the crack propagates to the 90°_4 layers facilitating the inter-fiber failure. Due to the smooth initiation and propagation (stemming from the infinite supports) of phase-field approximations, and quasi-static load conditions, only a qualitative assessment of the delamination migration has been presented in this study.

For each of the numerical simulations conducted in the sequel, a 2D analysis is carried with an out-of-plane thickness of 8.37mm. Hence, the domain is discretized through employing 960000 4-node quadrilateral plane stress elements with an average element size of 0.04mm, such that each layer of the cross-ply contains at least 4 elements across its thickness.

The material properties of IM7/8552 ply are shown in Table 4.2 consistent with the experimental results in [151]. The fracture energy and length scale parameters associated with the two phase-fields are shown in Table 4.3. The properties of the cohesive layer in accordance with [169] are listed in Table 4.4.

Table 4.2 IM7/8552: elastic properties.

E_{11} (GPa)	E_{22} (GPa)	G_{12} (GPa)	ν_{12} (minor)	ν_{23}
161.0	11.38	5.17	0.03	0.43

ÁMBITO- PREFIJO
GEISER
Nº registro
O00008744e2000024753
CSV
GEISER-aa34-5f08-a669-4b6e-9258-ed2f-d009-e7f3
DIRECCIÓN DE VALIDACIÓN
FECHA Y HORA DEL DOCUMENTO
19/06/2020 12:08:12 Horario peninsular
GEISER-aa34-5f08-a669-4b6e-9258-ed2f-d009-e7f3

Table 4.3 IM7/8552: intra-laminar fracture properties and phase-field parameters.

$\mathscr{G}_{c,FF}$ (N/mm)	$\mathscr{G}_{c,IFF}$ (N/mm)	l_{FF} (mm)	l_{IFF} (mm)
50.0	0.65	0.05	0.05

Table 4.4 Cohesive layer properties.

Nominal stress (MPa)	Nominal stress in shear (MPa)	Nominal fracture energy (N/mm)	Fracture energy in shear (N/mm)	Power (BK law)
15	15	0.5	0.65	2.17

4.5.2 Numerical-Experimental Validation

The global failure response for the specimen under consideration is investigated for the load case $L = a_0 = 49$mm. The numerical-experimental correlation corresponding to the load-displacement curve is given in Figure 4.4. As shown in this figure, the failure response can fairly be divided into three main zones (i) delamination of the cohesive zone, (ii) kinking followed by migration, and (iii) delamination of the top cohesive zone. Overall, a satisfactory agreement between the numerical and the experimental data can be observed.

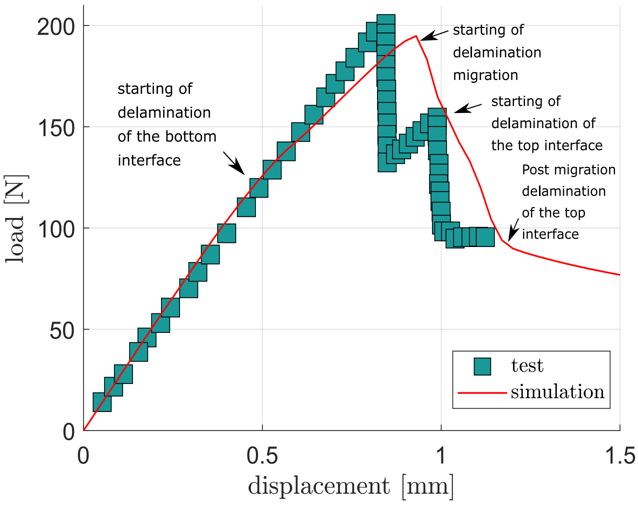

Figure 4.4 Numerical-experimental correlation corresponding to the load-displacement curve for $L = a_0$=49mm.

As was previously discussed, based on postulations made in [151, 152] and the corresponding thorough discussion, delamination migration occurs due to a change of sign in the shear stress components. Negative shearing stresses promote delamination growth at the $0^\circ/90^\circ$ interface, and positive shearing stresses promote migration/kinking into 90° plies. The kinking happens at multiple sites across the specimen. Due to the diffusive nature of the bulk cracks, the shearing stress change can easily be noticed by the initiation of the inter-fiber phase-field as depicted in Figure 4.5. Notice that, due to the negative sign at the beginning, delamination propagates until a certain point until shearing stresses are positive. Meanwhile, inter-fiber failure is already initiated,

ÁMBITO- PREFIJO
GEISER
Nº registro
O00008744e2000024753
CSV
GEISER-aa34-5f08-a669-4b6e-9258-ed2f-d009-e7f3
DIRECCIÓN DE VALIDACIÓN
FECHA Y HORA DEL DOCUMENTO
19/06/2020 12:08:12 Horario peninsular
GEISER-aa34-5f08-a669-4b6e-9258-ed2f-d009-e7f3

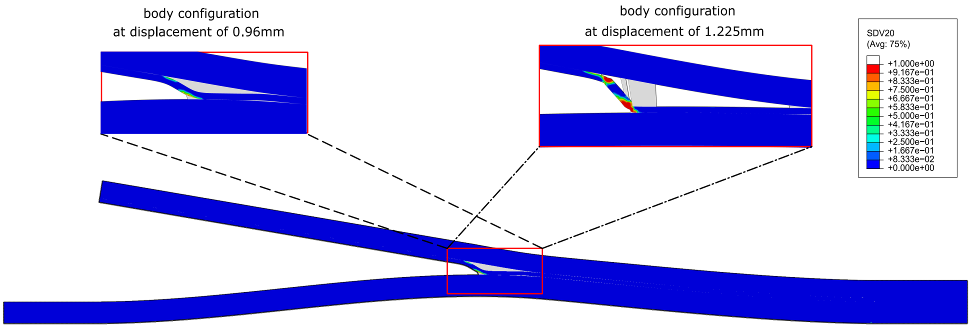

Figure 4.5 Inter-fiber crack field (SDV20) for $L = a_0$=49mm.

but from the opposite direction, i.e 90°/0° interface, but is not nucleated. Whereas, when the shear stresses become positive in the adjacent increments, the migration starts developing, with a crack front now migrating into the 90°/0° interface.

For a phenomenology of embodiment, in the cohesive layers, once the failure criterion is met, the cohesive layer starts delaminating. Similarly, when the Puck criterion is violated, the inter-fiber failure phase-field is activated due to shearing stresses in the model. As long as the $\mathfrak{P}_{IFF}$ is active, the inter-fiber failure phase-field crack $\mathfrak{d}_{IFF}$ grows and migrates into the 90° plies until the 90°/0° interface. Simultaneously, the top cohesive layer at the 90°/0° interface starts to delaminate. When the migration crack front crosses the 90°/0° interface, the crack front is again propagating due to the negative shear stress leading to the delamination of the top cohesive layer. Here onward, crack propagation is dominated by the residual stresses in the model as in Figure 4.4.

4.5.3 Sensitivity Analysis: Role of Different Parameters

This section aims at providing a further understanding with regard to the potential role of different design parameters that can favor delamination-migration events.

4.5.3.1 Effect of Position of Loading Application

The first aspect under analysis concerns the variation of load application point along the specimen. This parameter in the experimental setting might have a strong influence on the activation of migration phenomena by simply inducing a different local stress field at critical locations. Moreover, from a global standpoint, this can have notable effects on the load-displacement curve as the shear stresses acting on the specimen are significantly different from one another. Keeping $a_0 = 49$mm, the variation of load L for $L = 0.7a_0$, $0.8a_0$, $0.9a_0$, $1.0a_0$, and $1.1a_0$ are plotted in Fig. 4.6.

Based on the current results, it can be observed that for $a_0 > L$, all the cases exhibit delamination prior to migration and show a sudden drop in the load-carrying capacity when migration starts, see Figure 4.7. Whereas, for $a_0 < L$, the shearing stress sign is favorable for migration at the beginning, and hence there is smooth migration, with delamination spreading over the whole experiment, see Figure 4.7 which is consistent with [152]. It is also to notice that after delamination migration is finished, for all the load variations, the residual stiffness for delamination converges to a single value.

4.5.3.2 Effect of the Variation of Ply Angle

The second aspect understudy has an inherent local effect since it focused on the investigation of the delamination migration at $0^\circ/\Theta_4^\circ$ interface. For this purpose, the original stacking sequence

ÁMBITO- PREFIJO
GEISER
Nº registro
O00008744e2000024753
CSV
GEISER-aa34-5f08-a669-4b6e-9258-ed2f-d009-e7f3
DIRECCIÓN DE VALIDACIÓN
FECHA Y HORA DEL DOCUMENTO
19/06/2020 12:08:12 Horario peninsular
GEISER-aa34-5f08-a669-4b6e-9258-ed2f-d009-e7f3

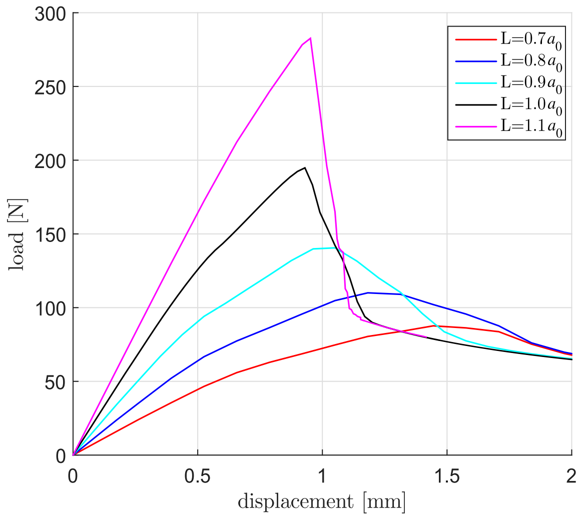

Figure 4.6 Variation of load across the specimen for $a_0 = 49$mm.

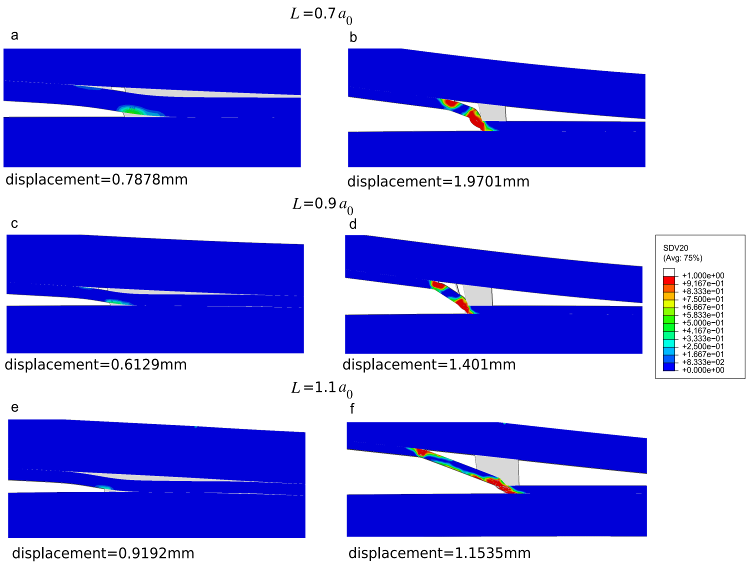
L=0.7a_0
a
b
displacement=0.7878mm
displacement=1.9701mm
L=0.9a_0
c
d
displacement=0.6129mm
displacement=1.401mm
SDV20
(Avg: 75%)
+1.000e+00
+9.167e−01
+8.333e−01
+7.500e−01
+6.667e−01
+5.833e−01
+5.000e−01
+4.167e−01
+3.333e−01
+2.500e−01
+1.667e−01
+8.333e−02
+0.000e+00
L=1.1a_0
e
f
displacement=0.9192mm
displacement=1.1535mm

Figure 4.7 Inter-fiber crack field (SDV20) from 3 cases at $L = 0.7a_0$, $L = 0.9a_0$, and $L = 1.1a_0$.

is replaced by a new layup sequence near the cohesive zones as $0^\circ_3/CL/\Theta^\circ_4/CL/0^\circ/0^\circ$. The fiber orientation, Θ° of 30°, 45°, and 60° is studied along with 90°, and the results are shown in Figure 4.8.

From this graph, it can be seen that the global pre-peak response is almost unaltered by the variation of the local orientation of the adjacent layers to the $0^\circ/\Theta^\circ_4$ interface. However, this aspect has a notable influence on the post-peak response, delaying the delamination initiation and the subsequent delamination event of the top interface, according to the description given in Figure 4.5, but however, the cracking migration is predicted to occur at almost the same loading

ÁMBITO- PREFIJO
GEISER
Nº registro
O00008744e2000024753
CSV
GEISER-aa34-5f08-a669-4b6e-9258-ed2f-d009-e7f3
DIRECCIÓN DE VALIDACIÓN
FECHA Y HORA DEL DOCUMENTO
19/06/2020 12:08:12 Horario peninsular
GEISER-aa34-5f08-a669-4b6e-9258-ed2f-d009-e7f3

level (along the post-peak evolution).

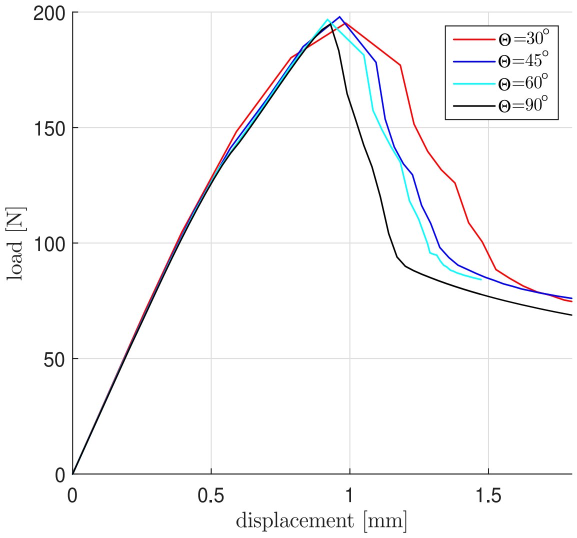

Figure 4.8 Variation of angle across the specimen for $L = a_0 = 49$mm.

4.5.3.3 Effect of the Variation of Initial Crack Length

The last effect under consideration corresponds to the initial crack length. Focusing on very specific cases, we vary initial crack size from $a_0 = 49$mm to $a_0 = 55$mm.

The global load-displacement evolution curves for such cases are shown in Figure 4.9. According to these data, it can be stated that a simple variation of the initial crack length has a very remarkable role in the specimen response. Thus, observing the pre-peak evolution, before any inelastic process commences, the larger the initial crack length is set, the higher the maximum load is achieved. Moreover, concerning the post-peak evolution, it is observable that while the shorter initial crack-length case evidences similar evolution with respect with those previously described, i.e. with the occurrence of delamination events and the posterior cracking migration to the adjacent layer, the response of $a_0 = 55$mm (and $a_0 > 55$mm) exhibited a completely different evolution with no evidence of cracking migration, see Figure 4.9, and 4.10 where the matrix-failure maps for both configurations are depicted. These differences in the response are directly associated with the discrepancies in the local stress state at the crack tips at the interface and at the intermediate layer. This is again inline with previous studies, showing the robustness and reliability of the proposed modeling framework.

4.6 Concluding Remarks

A consistent Multi Phase-Field-Cohesive Zone (MPF-CZ) model relying on Puck theory of failure was proposed for matrix-dominated cracking in the presence of interfaces. The failure mechanisms due to fiber failure, inter-fiber failure, and interface debonding are all accommodated in the model by considering multi phase-fields, each characterized by their failure mechanism with corresponding fracture energy and internal length scale, plus a cohesive zone model.

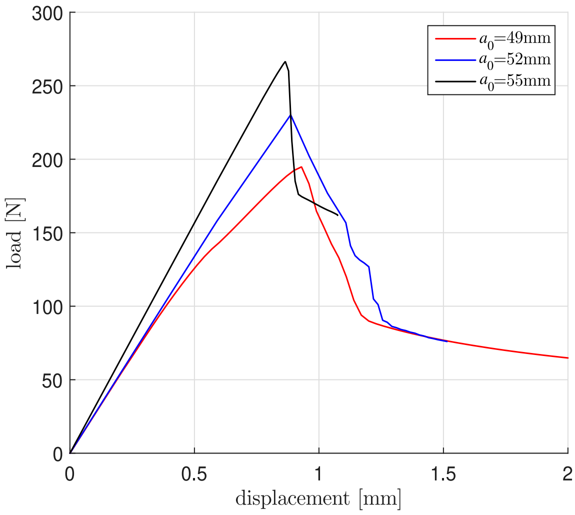

Figure 4.9 Variation of initial crack length across the specimen for $L = a_0$.

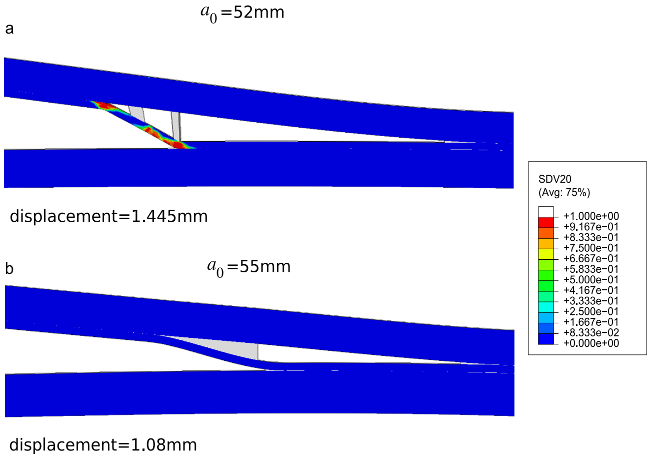
a
a_0=52mm
displacement=1.445mm
b
a_0=55mm
displacement=1.08mm
SDV20
(Avg: 75%)
+1.000e+00
+9.167e-01
+8.333e-01
+7.500e-01
+6.667e-01
+5.833e-01
+5.000e-01
+4.167e-01
+3.333e-01
+2.500e-01
+1.667e-01
+8.333e-02
+0.000e+00

Figure 4.10 Inter-fiber crack field (SDV20) for initial crack length $a_0 = 52$mm and $a_0 = 55$mm with $L = 1.0a_0$.

The computational framework was carefully derived via multi-field variational formulation with multiple dissipative mechanisms within the spirit of Phase-Field (PF) and Cohesive Zone (CZ) models such that thermodynamics consistency is preserved.

The model was applied to the study of delamination migration in multi-layered Long Fiber Reinforced Polymers (LFRPs) to illustrate the capabilities of the model. The variation of the design parameters, such as the load application point, the angle between the plies, and the initial crack length was presented to assess the sensitivity of the model response.

ÁMBITO- PREFIJO
GEISER
Nº registro
O00008744e2000024753
CSV
GEISER-aa34-5f08-a669-4b6e-9258-ed2f-d009-e7f3
DIRECCIÓN DE VALIDACIÓN
FECHA Y HORA DEL DOCUMENTO
19/06/2020 12:08:12 Horario peninsular
GEISER-aa34-5f08-a669-4b6e-9258-ed2f-d009-e7f3

5 Summary and Outlook

5.1 Summary and conclusions

The research presented in this dissertation deals with the comprehensive development of the numerical treatment of fracture events in different types of Fiber Reinforced Polymers (FRPS) within the framework of the Phase-Field (PF) approach to fracture. In particular, the attention is mainly focused on two types of composites materials, Short Fiber Reinforced Polymers (SFRPs) and Long Fiber Reinforced Polymers (LFRPs), which are extensively employed in different industrial sectors, such as aerospace and aeronautics and automobile applications, among others.

The current developments aimed at providing further insight into the different failure events that can arise in composites materials aforementioned and would contribute to the establishment of new paradigms in the design processes of the corresponding parts, leading to significant reductions of the currently used safety factors. Moreover, from the environmental perspective, this would result in optimized structural components inducing notable reductions in payload, fuel consumption, and energy demands for the manufacturing processes.

The results and discussions throughout the present text show that the primary goals of the present research have been successfully achieved.

The first part of the dissertation was devoted to the development of a new numerical method for the simulation of the failure response of short fiber reinforced polymers. This new formation exploited the fundamental concepts of the phase-field approach to fracture but incorporated the corresponding attributes for SFRPs. In particular, within the context of macro-scale phenomenological models, the use of the invariant-based theory for accounting for the anisotropic character of SFRPs has been employed. This theory has exhibited strong potential for capturing the macroscopic behavior of such materials but enabling the representation of complex mechanical responses. In order to accommodate the use of the PF method, the baseline formulation of this method was rigorously extended to the elaso-plastic fracture response. Moreover, an additional novel ingredient of the present research was the employment of a non-associative elasto-plastic formulation which enables capturing more realistic plastic deformations. The corresponding governing equations for ductile fracture modeling of SFRPs lead to a multi-field formulation, whose corresponding discrete system of equations was solved via a staggered solution-scheme utilizing the commercial FE code `ABAQUS`. To do so, the proposed model was implemented via user-defined capabilities, combining the use of user-defined elements and materials.

To conclude, the proposed coupled elasto-plastic phase-field model can successfully capture anisotropic ductile fracture in SFRPs with more realistic plastic deformations.

ÁMBITO- PREFIJO
GEISER
Nº registro
O00008744e2000024753
CSV
GEISER-aa34-5f08-a669-4b6e-9258-ed2f-d009-e7f3
DIRECCIÓN DE VALIDACIÓN
FECHA Y HORA DEL DOCUMENTO
19/06/2020 12:08:12 Horario peninsular
GEISER-aa34-5f08-a669-4b6e-9258-ed2f-d009-e7f3

The second research topic in this thesis comprised the analysis of failure response of long fiber reinforced polymers from a numerical perspective using a novel multi phase-field modeling approach. In view of the limitation of standard damage models for LFRPs, the main motivation striving for this new development was the new attributes offered by the PF approach to fracture, i.e. reduced mesh-dependence and robust account for fracture. In line with the model for SFRPs, a macro-scale representation was assumed. In this concern, the developed formulation represented a remarkable advancement in the current State of the Art on the topic. The point of departure was again the variational formulation of the PF approach to fracture. However, in order to differentiate the potential occurrence of damage mechanisms in LFRPs from different signatures, i.e. fiber and matrix-dominated cracking events, the standard PF formulation was further enhanced with the consideration of two different crack-like phase-field variables which are associated to both failure mechanisms.

For the consistent activation of both failure types, without any loss of generality, the so-called Puck's failure theory was recalled. The selection of such failure criterion for LFRPs has been adopted as a consequence of its reliability in different World Wide Failure Exercises (WWFEs) on composites materials. Notwithstanding, it is remarkable that the current formulation can accommodate any other failure criterion with simple and minor modifications of the code.

With respect to the specific modifications of PF models for bulk failure, the distinction between two different failure mechanisms encompassed the consideration of two different crack-like phase-field variables, with the corresponding phenomenological stress-based criterion for damage activation, as well the respective values for the fracture toughness and length scale. It is worth mentioning that this resulted in a novel FE design with a physically-sound fracture criterion, but increasing the number of the required material parameters for the damage activation, i.e not only those required for the PF method but also the set that is inserted into the Puck failure surfaces. This might lead to difficulties for the experimental characterization of such parameters however this is an aspect already present in most of the local continuum damage models for LFRPs.

From the computational side, the inclusion of an additional phase-field variable incurred in the modifications of the baseline FE implementation for the PF approach, adding an extra degree of freedom per node. Note also that the abrupt fiber failure might lead to difficulties in achieving equilibrium solutions in the corresponding numerical procedure.

To conclude, the developed multi phase-field model can successfully predict the physically observed inter-laminar (fiber and inter-fiber) fracture events in LFRPs.

Though the current Puck-based multi phase-field approach to fracture is oriented towards modeling intra-laminar failure in LFRPs, the last part of the present thesis dealt with the combination of the PF method for bulk fracture with interface-like crack methods (in particular cohesive modeling) for inter-laminar events. For this purpose, the standard variational formulation has been further equipped by means of the specific decomposition of the dissipative part of the governing functional, making the discrimination between intra- and inter-laminar fracture. This approximation has been already proposed in the related literature, but in this research, the coupling with the multi phase-field approach to fracture was performed. Moreover, the main application under an analysis of such a coupled cracking method regarded a situation of high practical interest, as is the case of the delamination migration phenomena in multi-layered LFRPs. From a more theoretical and numerical standpoint, it is worth mentioning that the implicit competition between the onset and progress of both dissipative phenomena led to different numerical difficulties due to the staggered solution scheme herewith employed, which were overcome by the careful examination of the different available solving capabilities.

To conclude, the proposed coupled multi phase-field cohesive zone strategy can successfully predict delamination migration phenomena in multi-layered LFRPs.

5.2 Future developments

Stemming from the theoretical developments and the corresponding numerical treatment of the models herewith proposed, several research areas are identified for potential improvement and enhancement.

At present, prospective investigations concerning failure responses of SFRPs would require the conduction of careful experimental campaigns. The main target of such experimental studies is motivated for the achievement of a more comprehensive understanding of fracturing response of such materials under different loading cases and rates.

Focusing on the numerical developments, continuing the research of this thesis, the proposed model for SFRPs can be revisited using the feedback from the experimental campaigns mentioned above. However, further developments are required for capturing large deformation effects and thermo-mechanical fractures in both, SFRPs and LFRPs. An area of high interest will also encompass the prediction of damage and fracture events due to fatigue loading conditions. Such novel theoretical and computational formulations are being under development. However, these developments will again necessitate the conduction of experimental tests for complementing purposes. Another ongoing research related to LFRPs regards the application of the proposed formulation for modeling fracture events in large composite structures such as the case of stiffened panels, specimens with stress concentrators, among many other cases.

With respect to the future directions of research, an interesting topic would be the extension of the proposed elasto-plastic PF fracture modeling for other materials. This can be the case of porous materials, geomaterials, among many others. Finally, a very interesting direction for both types of composite materials herewith investigated will be the use of multi-scale modeling approaches to further the understanding of the micro-macro transition of cracking events, as well as the corresponding investigation of size-effects in composites.

ÁMBITO- PREFIJO	CSV	FECHA Y HORA DEL DOCUMENTO
GEISER	**GEISER-aa34-5f08-a669-4b6e-9258-ed2f-d009-e7f3**	**19/06/2020 12:08:12 Horario peninsular**
Nº registro	DIRECCIÓN DE VALIDACIÓN	
O00008744e2000024753	**https://sede.administracionespublicas.gob.es/valida**	

GEISER-aa34-5f08-a669-4b6e-9258-ed2f-d009-e7f3

List of Figures

1.1 Damage and fracture mechanisms in loaded FRPs: (a) failure mechanisms in SFRPs at micro-scale and (b) failure mechanisms in LFRPs meso-scale 3
1.2 Fracture modes: (a) Mode-I (opening mode), (b) Mode-II (shearing mode), and Mode-III (tearing mode) 10
1.3 Phase-field method for diffusive crack modelling in solids: (a) sharp crack representation and (b) regularized crack topology 12

2.1 One-dimensional problem: (a) sharp crack representation at $x = 0$ and (b) regularized crack topology at $x = 0$, depending on the length scale l 21
2.2 Phase-field method for diffusive crack modelling for anisotropic materials: (a) sharp crack representation and (b) regularized crack topology 22
2.3 Schematic representation of the transversely isotropic yield function (left) and plastic potential (right) in the stress invariant space. 27
2.4 Numerical simulations vs experimental results: (a) longitudinal uniaxial tension, (b) transverse uniaxial tension, (c) longitudinal uniaxial compression, and (d) transverse uniaxial compression 32
2.5 Simultaneous evolution of the plastic deformations and the cracking process: the case of longitudinal uniaxial tension 32
2.6 Dog-bone specimen of PA6GF60: specimen definition, FE discretization, and boundary conditions 33
2.7 Dog-bone specimen of PA6GF60 under uniaxial tension: (a), (b), and (c) phase-field parameter (SDV22) evolution at different loading stages and (d) experimental-numerical correlation 33
2.8 Single-edge notched specimen of PA6GF30: specimen definition, FE discretization, and boundary conditions 34
2.9 Ductile fracture of the single-edge notched specimen of PA6GF30: phase-field parameter (SDV22) evolution at different loading stages 35
2.10 Ductile fracture of the single-edge notched specimen of PA6GF30: equivalent plastic strain (SDV13) 36

3.1 Puck failure theory: Illustration of the different inter-fiber failure (IFF) modes according to the 3D Puck criterion [131] 44
3.2 Three-layer structure of `ABAQUS` subroutine 52

ÁMBITO- PREFIJO
GEISER
Nº registro
O00008744e2000024753
CSV
GEISER-aa34-5f08-a669-4b6e-9258-ed2f-d009-e7f3
DIRECCIÓN DE VALIDACIÓN
FECHA Y HORA DEL DOCUMENTO
19/06/2020 12:08:12 Horario peninsular
GEISER-aa34-5f08-a669-4b6e-9258-ed2f-d009-e7f3

3.3 Numerical simulations and experimental results: FF Mode 54
3.4 Numerical simulations and experimental results: (a) IFF Mode A and (b) IFF Mode C 54
3.5 Numerical simulations and experimental results of the pure shear case: (a) stress-strain response and (b) simultaneous evolution of the plastic deformations and the inter-fiber cracking process 55
3.6 GFRP plate with an initial notch: specimen geometry and boundary conditions 56
3.7 Inter-fiber phase-field crack (SDV20) from case 1 of the GFRP plate in: (a) undeformed configuration and (b) deformed configuration 56
3.8 Inter-fiber phase-field crack (SDV20) from case 2 of the GFRP plate in: (a) undeformed configuration and (b) deformed configuration 57
3.9 Inter-fiber phase-field crack (SDV20) from case 3 of the GFRP plate in: (a) undeformed configuration and (b) deformed configuration 57
3.10 open-hole tension problem: specimen geometry and boundary conditions 57
3.11 Open-hole tension problem: Numerical-experimental correlation corresponding to the load-displacement curve 58
3.12 Open-hole tension problem: IFF phase-field crack (SDV26) evolution in the outer 90° layer at different loading stages: (a) 60% of the ultimate load, (b) 80% of the ultimate load, (c) 100% of the ultimate load, and (d) rupture 59
3.13 Open-hole tension problem: FF phase-field crack (SDV23) evolution in the outer 0° layer at different loading stages: (a) 60% of the ultimate load, (b) 80% of the ultimate load, (c) 100% of the ultimate load, and (d) rupture 60

4.1 Body under consideration: (a) sharp crack representation and (b) regularized crack topology 65
4.2 Schematic representation of the bi-linear cohesive zone model traction-separation law for mixed-mode 69
4.3 Schematic representation of the delamination migration model 76
4.4 Numerical-experimental correlation corresponding to the load-displacement curve for $L = a_0$=49mm 77
4.5 Inter-fiber crack field (SDV20) for $L = a_0$=49mm 78
4.6 Variation of load across the specimen for $a_0 = 49$mm 79
4.7 Inter-fiber crack field (SDV20) from 3 cases at $L = 0.7a_0$, $L = 0.9a_0$, and $L = 1.1a_0$ 79
4.8 Variation of angle across the specimen for $L = a_0 = 49$mm 80
4.9 Variation of initial crack length across the specimen for $L = a_0$ 81
4.10 Inter-fiber crack field (SDV20) for initial crack length $a_0 = 52$mm and $a_0 = 55$mm with $L = 1.0a_0$ 81

ÁMBITO- PREFIJO
GEISER
Nº registro
O00008744e2000024753

CSV
GEISER-aa34-5f08-a669-4b6e-9258-ed2f-d009-e7f3
DIRECCIÓN DE VALIDACIÓN

FECHA Y HORA DEL DOCUMENTO
19/06/2020 12:08:12 Horario peninsular

GEISER-aa34-5f08-a669-4b6e-9258-ed2f-d009-e7f3

List of Tables

2.1 PA6GF30 (1mm in thickness): elastic properties 30
2.2 PA6GF60 (1mm in thickness): elastic properties 30
2.3 PA6GF30 (1mm in thickness): yielding parameters ζ_i at the onset of yielding 30
2.4 PA6GF60 (1mm in thickness): yielding parameters ζ_i at the onset of yielding 30
2.5 PA6GF30 (1mm in thickness): Plastic Poisson's ratios 30
2.6 PA6GF60 (1mm in thickness): plastic Poisson's ratios 30
2.7 PA6GF30 (1mm in thickness): failure parameters ξ_i at the onset of failure 30
2.8 PA6GF60 (1mm in thickness): failure parameters ξ_i at the onset of failure 31
2.9 PA6GF30 (1mm in thickness): fracture properties and phase filed parameters 31
2.10 PA6GF60 (1mm in thickness): fracture properties and phase filed parameters 31

3.1 Recommended inclination factors for CFRP and GFRP composites 46
3.2 CFRP and GFRP: elastic properties. 53
3.3 CFRP and GFRP: yielding parameters ζ_i at the onset of yielding. 53
3.4 CFRP and GFRP: plastic Poisson's ratios. 53
3.5 CFRP and GFRP: strength properties. 53
3.6 CFRP and GFRP: fracture properties and phase-field parameters. 53
3.7 GFRP plate with an initial notch: fiber orientation arrangement for the three different cases. 55
3.8 CFRP: in-situ strengths properties 58

4.1 Recommended inclination factors for CFRP and GFRP composites 72
4.2 IM7/8552: elastic properties 76
4.3 IM7/8552: intra-laminar fracture properties and phase-field parameters 77
4.4 Cohesive layer properties 77

ÁMBITO- PREFIJO
GEISER
Nº registro
O00008744e2000024753

CSV
GEISER-aa34-5f08-a669-4b6e-9258-ed2f-d009-e7f3
DIRECCIÓN DE VALIDACIÓN

FECHA Y HORA DEL DOCUMENTO
19/06/2020 12:08:12 Horario peninsular

GEISER-aa34-5f08-a669-4b6e-9258-ed2f-d009-e7f3

Bibliography

[1] M. Zoghi. *The International Handbook Of FRP Composites In Civil Engineering*. CRC Press, 2013.

[2] *Composite Materials Handbook*. SAE International, 2017.

[3] G.A. Maugin. Internal variables and dissipative structures. *Journal of Non-Equilibrium Thermodynamics*, 15:173 – 192, 1990.

[4] G.A. Maugin and W. Muschik. Thermodynamics with internal variables part i. general concepts. *Journal of Non-Equilibrium Thermodynamics*, 19:217 – 249, 1994.

[5] G.A. Maugin and W. Muschik. Thermodynamics with internal variables part II. applications. *Journal of Non-Equilibrium Thermodynamics*, 19:250 – 289, 1994.

[6] H. Frémond. *Non-Smooth Thermomechanics*. Springer, 2001.

[7] T. Belytschko and T. Black. Elastic crack growth in finite elements with minimal remeshing. *International Journal for Numerical Methods in Engineering*, 45:601 – 620, 1999.

[8] G.N. Wells and L.J. Sluys. A new method for modelling cohesive cracks using finite elements. *International Journal for Numerical Methods in Engineering*, 50:2667 – 2682, 2001.

[9] J.C. Simo, J. Oliver, and F. Armero. An analysis of strong discontinuities induced by strain-softening in rate-independent inelastic solids. *Computational Mechanics*, 12:277 – 296, 1993.

[10] J. Mosler and G. Meschke. 3d modelling of strong discontinuities in elastoplastic solids: fixed and rotating localization formulations. *International Journal for Numerical Methods in Engineering*, 57:1553 – 1576, 2003.

[11] J.Y. Wu, V.P. Nguyen, C.T. Nguyen, D. Sutula, S. Sinaie, and S. Bordas. Phase field modelling of fracture. *Advances in Applied Mechanics*, 53, 2019.

[12] L. Ambrosio and V.M. Tortorelli. Approximation of functionals depending on jumps by elliptic functionals via γ-convergence. *Communications on Pure and Applied Mathematics*, 43:999 – 1036, 1990.

ÁMBITO- PREFIJO
GEISER
Nº registro
O00008744e2000024753

CSV
GEISER-aa34-5f08-a669-4b6e-9258-ed2f-d009-e7f3
DIRECCIÓN DE VALIDACIÓN

FECHA Y HORA DEL DOCUMENTO
19/06/2020 12:08:12 Horario peninsular

GEISER-aa34-5f08-a669-4b6e-9258-ed2f-d009-e7f3

[13] G.A. Francfort and J.J. Marigo. Revisiting brittle fracture as an energy minimization problem. *Journal of the Mechanics and Physics of Solids*, 46:1319 – 1342, 1998.

[14] B. Bourdin, G.A. Francfort, and J.J. Marigo. Numerical experiments in revisited brittle fracture. *Journal of the Mechanics and Physics of Solids*, 48:797 – 826, 2000.

[15] B. Bourdin, G.A. Francfort, and J.J. Marigo. The variational approach to fracture. *Journal of Elasticity*, 91:5 – 148, 2008.

[16] E.J. Barbero. *Introduction to composite materials design*. CRC Press, 2017.

[17] J. Schöpfer. *Spritzgussbauteile aus kurzfaserverstärkten Kunststoffen: Methoden der Charakterisierung und Modellierung zur nichtlinearen Simulation von statischen und crashrelevanten Lastfällen*. Doctoral degree, dissertation thesis, Institut für Verbundwerkstoffe, Technische Universität Kaiserslautern, 2011.

[18] J. Stevenson. *Innovations in Polymer Processing: Moulding*. Hanser, 1996.

[19] P.P. Camanho. *Application of Numerical Methods to the Strength Prediction of Mechanically Fastened Joints in Composite Laminates*. Doctoral degree, dissertation thesis, Imperial College London, 1999.

[20] F. Meraghni and M.L. Benzeggah. Micromechanical modelling of matrix degradation in randomly oriented discontinuous-fibre composites. *Composites Science and Technology*, 55:171 – 186, 1995.

[21] S.T. Pinho. *Modelling failure of laminated composites using physically-based failure models*. Doctoral degree, dissertation thesis, Imperial College London, 2005.

[22] G. Meschke. Lecture notes in finite element methods in linear structural mechanics, 2016.

[23] C. Truesdell, W. Noll, and S. Antman. *The Non-Linear Field Theories of Mechanics*. Springer Science+Business Media, 2004.

[24] A.A. Griffith. The phenomena of rupture and flow in solids. *Philosophical Transactions of the Royal Society of Londres*, 221:163 – 198, 1920.

[25] G.R. Irwin. Analysis of stresses and strains near the end of a crack traversing a plate. *Journal of Applied Mechanics*, 24:361 – 364, 1957.

[26] G. Barenblatt. The mathematical theory of equilibrium of cracks in brittle fracture. *Advances in Applied Fracture*, 7:155 – 129, 1962.

[27] D. Leguillon. Strength or toughness? a criterion for crack onset at a notch. *European Journal of Mechanics - A/Solids*, 21:61 – 72, 1962.

[28] A. Carpinteri, P. Cornetti, N. Pugno, A. Sapora, and D. Taylor. Generalized fracture toughness for specimens with re-entrant corners: Experiments vs. theoretical predictions. *Structural Engineering and Mechanics*, 32:609 – 620, 2009.

[29] M. Ortiz, Y. Leroy, and A. Needleman. A finite element method for localized failure analysis. *Computer Methods in Applied Mechanics and Engineering*, 61:189 – 214, 1987.

[30] L.M. Kachanov. Time of the rupture process under creep conditions. *Izvestiya Akademii Nauk Sssr*, 8:26 – 31, 1958.

ÁMBITO- PREFIJO	CSV	FECHA Y HORA DEL DOCUMENTO
GEISER	**GEISER-aa34-5f08-a669-4b6e-9258-ed2f-d009-e7f3**	**19/06/2020 12:08:12 Horario peninsular**
Nº registro	DIRECCIÓN DE VALIDACIÓN	
O00008744e2000024753	**https://sede.administracionespublicas.gob.es/valida**	

GEISER-aa34-5f08-a669-4b6e-9258-ed2f-d009-e7f3

[31] P.P. Camanho, P. Maimí, and C.G. Dávila. Prediction of size effects in notched laminates using continuum damage mechanics. *Composites Science and Technology*, 67:2715 – 2727, 2007.

[32] A. Quintanas-Corominas. *Towards a High-Performance Computing Finite Element Simulation Framework for Virtual Testing of Composite Structures*. Doctoral degree, dissertation thesis, Universitat de Girona, 2019.

[33] M. Jirasek and Z.P. Bazant. *Inelastic Analysis of Structures*. John Wiley and Sons, 2001.

[34] I.S. Aranson, V.A. Kalatsky, and V.M. Vinokur. Continuum field description of crack propagation. *Physical Review Letters*, 85:118 – 121, 2000.

[35] C. Miehe and L.M. Schänzel. Phase field modeling of fracture in rubbery polymers. part i: Finite elasticity coupled with brittle failure. *Journal of the Mechanics and Physics of Solids*, 65:93 – 113, 2014.

[36] C. Hesch and K. Weinberg. Thermodynamically consistent algorithms for a finite-deformation phase-field approach to fracture. *International Journal for Numerical Methods in Engineering*, 99:906 – 924, 2014.

[37] M. Ambati, R. Kruse, and L. De Lorenzis. A phase-field model for ductile fracture at finite strains and its experimental verification. *Computational Mechanics*, 57:149 – 167, 2016.

[38] O. Gültekin, H. Dal, and G. A. Holzapfel. A phase-field approach to model fracture of arterial walls: Theory and finite element analysis. *Computer Methods in Applied Mechanics and Engineering*, 312:542 – 566, 2016.

[39] S. Teichtmeister, D. Kienle, F. Aldakheel, and M. Keip. Phase field modeling of fracture in anisotropic brittle solids. *International Journal of Non-Linear Mechanics*, 97:1 – 21, 2017.

[40] B. Li and C. Maurini. Crack kinking in a variational phase-field model of brittle fracture with strongly anisotropic surface energy. *Journal of the Mechanics and Physics of Solids*, 125:502 – 522, 2019.

[41] B. Bourdin, G.A. Francfort, and J.J. Marigo. *Innovations in Polymer Processing: Moulding*. Springer, Berlin, 2008.

[42] H. Amor, J.J. Marigo, and C. Maurini. Regularized formulation of the variational brittle fracture with unilateral contact: numerical experiments. *Journal of the Mechanics and Physics of Solids*, 57:1209 – 1229, 2009.

[43] C. Miehe, M. Hofacker, and F. Welschinger. A phase field model for rate-independent crack propagation: Robust algorithmic implementation based on operator splits. *Computer Methods in Applied Mechanics and Engineering*, 199:2765 – 2778, 2010.

[44] E. Tanné, T. Li, B. Bourdin, J.J. Marigo, and C. Maurini. Crack nucleation in variational phase-field models of brittle fracture. *Journal of the Mechanics and Physics of Solids*, 110:80 – 99, 2018.

ÁMBITO- PREFIJO	CSV	FECHA Y HORA DEL DOCUMENTO
GEISER	**GEISER-aa34-5f08-a669-4b6e-9258-ed2f-d009-e7f3**	**19/06/2020 12:08:12 Horario peninsular**
Nº registro	DIRECCIÓN DE VALIDACIÓN	
O00008744e2000024753	**https://sede.administracionespublicas.gob.es/valida**	

GEISER-aa34-5f08-a669-4b6e-9258-ed2f-d009-e7f3

[45] C. Miehe, L.M. Schänzel, and H. Ulmer. Phase field modeling of fracture in multi-physics problems. part i. balance of crack surface and failure criteria for brittle crack propagation in thermo-elastic solids. *Computer Methods in Applied Mechanics and Engineering*, 294:449 – 485, 2015.

[46] C. Miehe, M. Hofacker, L.M. Schaenzel, and F. Aldakheel. Phase field modeling of fracture in multi-physics problems. part II. coupled brittle-to-ductile failure criteria and crack propagation in thermo-elastic-plastic solids. *Computer Methods in Applied Mechanics and Engineering*, 294:486 – 522, 2015.

[47] M.J. Borden, T.J.R. Hughes, C.M. Landis, and C.V. Verhoosel. A higher-order phase-field model for brittle fracture: Formulation and analysis within the isogeometric analysis framework. *Computer Methods in Applied Mechanics and Engineering*, 273:100 – 118, 2014.

[48] M. Ortiz and A. Pandolfi. Finite-deformation irreversible cohesive elements for three-dimensional crack-propagation analysis. *International Journal for Numerical Methods in Engineering*, 44(9):1267 – 1282, 1999.

[49] M. Paggi and J. Reinoso. An anisotropic large displacement cohesive zone model for fibrillar and crazing interfaces. *International Journal of Solids and Structures*, 69:106–120, 2015.

[50] A. Turon, P.P. Camanho, J. Costa, and C.G. Dávila. A damage model for the simulation of delamination in advanced composites under variable-mode loading. *Mechanics of Materials*, 38:1072 – 1089, 2006.

[51] A. Turon, C.G. Dávila, P.P. Camanho, and J. Costa. An engineering solution for mesh size effects in the simulation of delamination using cohesive zone models. *Engineering Fracture Mechanics*, 74:1665 – 1682, 2007.

[52] J. Reinoso, M. Paggi, and A. Blázquez. A nonlinear finite thickness cohesive interface element for modeling delamination in fibre-reinforced composite laminates. *Composites Part B: Engineering*, pages 116 – 128, 2017.

[53] N. Moës, J. Dolbow, and T. Belytschko. A finite element method for crack growth without remeshing. *International journal for numerical methods in engineering*, 46:131–150, 1999.

[54] C. Linder and F. Armero. Finite elements with embedded strong discontinuities for the modeling of failure in solids. *International Journal for Numerical Methods in Engineering*, 72:1391–1433, 2007.

[55] C. Miehe, F. Welschinger, and M. Hofacker. Thermodynamically consistent phase-field models of fracture: Variational principles and multi-field fe implementations. *International Journal for Numerical Methods in Engineering*, 83:1273–1311, 2010.

[56] J.Y. Wu. A unified phase-field theory for the mechanics of damage and quasi-brittle failure. *Journal of the Mechanics and Physics of Solids*, 103:72 – 99, 2017.

[57] J.Y. Wu and V.P. Nguyen. A length scale insensitive phase-field damage model for brittle fracture. *Journal of the Mechanics and Physics of Solids*, 119:20 – 42, 2018.

ÁMBITO- PREFIJO	CSV	FECHA Y HORA DEL DOCUMENTO
GEISER	**GEISER-aa34-5f08-a669-4b6e-9258-ed2f-d009-e7f3**	**19/06/2020 12:08:12 Horario peninsular**
Nº registro	DIRECCIÓN DE VALIDACIÓN	
O00008744e2000024753	**https://sede.administracionespublicas.gob.es/valida**	

GEISER-aa34-5f08-a669-4b6e-9258-ed2f-d009-e7f3

[58] M. Paggi and J. Reinoso. Revisiting the problem of a crack impinging on an interface: a modeling framework for the interaction between the phase field approach for brittle fracture and the interface cohesive zone model. *Computer Methods in Applied Mechanics and Engineering*, 321:145 – 172, 2017.

[59] V. Carollo, J. Reinoso, and M. Paggi. Modeling complex crack paths in ceramic laminates: a novel variational framework combining the phase field method of fracture and the cohesive zone model. *Journal of the European Ceramic Society*, 38:2994 – 3003, 2018.

[60] M Ambati, T Gerasimov, and L De Lorenzis. Phase-field modeling of ductile fracture. *Computational Mechanics*, 55:1017–1040, 2015.

[61] E. Martínez-Pañeda, A. Golahmar, and C.F. Niordson. A phase field formulation for hydrogen assisted cracking. *Computer Methods in Applied Mechanics and Engineering*, 342:742 – 761, 2018.

[62] Z.A. Wilson and C.M. Landis. Phase-field modeling of hydraulic fracture. *Journal of the Mechanics and Physics of Solids*, 96:264 – 290, 2016.

[63] D. Kienle, F. Aldakheel, and M.A. Keip. A finite-strain phase-field approach to ductile failure of frictional materials. *International Journal of Solids and Structures*, 172-173:147 – 162, 2019.

[64] O. Gültekin, H. Dal, and G.A. Holzapfel. Numerical aspects of anisotropic failure in soft biological tissues favor energy-based criteria: A rate-dependent anisotropic crack phase-field model. *Computer Methods in Applied Mechanics and Engineering*, 331:23 – 52, 2018.

[65] J. Bleyer and R. Alessi. Phase-field modeling of anisotropic brittle fracture including several damage mechanisms. *Computer Methods in Applied Mechanics and Engineering*, 336:213 – 236, 2018.

[66] A. Quintanas-Corominas, J. Reinoso, E. Casoni, A. Turon, and J.A. Mayugo. A phase field approach to simulate intralaminar and translaminar fracture in long fiber composite materials. *Composite Structures*, 220:899 – 911, 2019.

[67] N. Sato, T. Kurauchi, S. Sato, and O. Kamigaito. Microfailure behaviour of randomly dispersed short fibre reinforced thermoplastic composites obtained by direct sem observation. *Journal of Materials Science*, 26:3891 – 3898, 1991.

[68] S.Y. Fu and B. Lauke. The elastic modulus of misaligned short-fiber-reinforced polymers. *Composites Science and Technology*, 58:389–400, 1998.

[69] A.A. Gusev, P.J. Hine, and I.M. Ward. Fiber packing and elasticity properties of a transversely random unidirectional glass/epoxy composite. *Composites Science and Technology*, 60:553 – 545, 2000.

[70] M.F. Arif, F. Meraghni, Y. Chemisky, N. Despringre, and G. Robert. In situ damage mechanisms investigation of pa66/gf30 composite effect of relative humidity. *Composites Part B: Engineering*, 58:487–495, 2014.

[71] M.F. Arif, N. Saintier, F. Meraghni, J. Fitoussi, Y. Chemisky, and G. Robert. Multiscale fatigue damage characterization in short glass fiber reinforced polyamide-66. *Composites Part B: Engineering*, 61:55 – 65, 2014.

ÁMBITO- PREFIJO
GEISER
Nº registro
O00008744e2000024753

CSV
GEISER-aa34-5f08-a669-4b6e-9258-ed2f-d009-e7f3
DIRECCIÓN DE VALIDACIÓN

FECHA Y HORA DEL DOCUMENTO
19/06/2020 12:08:12 Horario peninsular

GEISER-aa34-5f08-a669-4b6e-9258-ed2f-d009-e7f3

[72] F.T. Ibanez and S. Cicero. Fracture assessment of notched short glass fibre reinforced polyamide 6: An approach from failure assessment diagrams and the theory of critical distances. *Composites Part B: Engineering*, 111:124 – 133, 2017.

[73] J.J. Horst and J.L. Spoormaker. Mechanisms of fatigue in short glass ber reinforced polyamide 6. *Polymer Engineering & Science*, 36:2718 – 2726, 1996.

[74] A. Launay, M.H. Maitournam, Y. Marco, I. Raoult, and F. Szmytk. Cyclic behaviour of short glass fibre reinforced polyamide: Experimental study and constitutive equations. *International Journal of Plasticity*, 27:1267–1293, 2011.

[75] B. Mouhmid, A. Imad, N. Benseddiq, S. Benmedakhene, and A. Maazouz. A study of the mechanical behaviour of a glass fibre reinforced polyamide 6,6: experimental investigation. *Polymer Testing*, 25:544–552, 2006.

[76] E. Belmonte, M. De Monte, C. Hoffmann, and M. Quaresimin. Damage initiation and evolution in short fiber reinforced polyamide under fatigue loading: Influence of fiber volume fraction. *Composites Part B: Engineering*, 113:331–341, 2017.

[77] M. De Monte, E. Moosbrugger, and M. Quaresimin. Influence of temperature and thickness on the off-axis behaviour of short glass fibre reinforced polyamide 6.6 - quasi-static loading. *Composites Part A: Applied Science and Manufacturing*, 41:859–871, 2010.

[78] S.G. Advani and R. Talreja. A continuum approach to determination of elastic properties of short fibre composites. *Mechanics of Composite Materials*, 29:171–183, 1993.

[79] P. Lazzarin, G. Molina, L. Molinari, and M. Quaresimin. Numerical simulation of smc component moulding. *Key Engineering Materials*, 144:191–202, 1998.

[80] J. Spahn, H. Andra, M . Kabel, and R. Muller. A multiscale approach for modeling progressive damage of composite materials using fast fourier transforms. *Computer Methods in Applied Mechanics and Engineering*, 268:871–883, 2014.

[81] J. Spahn. *An Efficient Multiscale Method for Modeling Progressive Damage in Composite Materials*. Doctoral degree, dissertation thesis, Technischen Universität Kaiserslautern, 2015.

[82] P. Kanoute, D.P. Boso, J.L. Chaboche, and B.A. Schrefler. Multiscale methods for composites: A review. *Archives of Computational Methods in Engineering*, 16:31–75, 2009.

[83] M. Vogler, F.X.C. Andrade, J. Schöpfer, S. Kolling, and R. Rolfes. A novel transversely-isotropic 3d elastic-viscoplastic constitutive law for modeling fiber matrix composites. In *8th European LS-DYNA users conference, Strasbourg, France*, May 2011.

[84] M. Vogler, R. Rolfes, and P.P. Camanho. Modeling the inelastic deformation and fracture of polymer composites-part i: plasticity model. *Mechanics of Materials*, 59:50 – 64, 2013.

[85] A. Dean, S. Sahraee, J. Reinoso, and R. Rolfes. Finite deformation model for short fibre reinforced composites: Application to hybrid metal-composite clinching joints. *Composite Structures*, 150:162 – 171, 2016.

[86] A. Dean, J. Reinoso, S. Sahraee, and R. Rolfes. An invariant-based anisotropic material model for short fiber-reinforced thermoplastics: Coupled thermo-plastic formulation. *Composites Part A: Applied Science and Manufacturing*, 90:186 – 199, 2016.

ÁMBITO- PREFIJO
GEISER
Nº registro
O00008744e2000024753

CSV
GEISER-aa34-5f08-a669-4b6e-9258-ed2f-d009-e7f3
DIRECCIÓN DE VALIDACIÓN

FECHA Y HORA DEL DOCUMENTO
19/06/2020 12:08:12 Horario peninsular

GEISER-aa34-5f08-a669-4b6e-9258-ed2f-d009-e7f3

[87] A. Dean, S. Sahraee, J. Reinoso, and R. Rolfes. A new invariant-based thermo-plastic model for finite deformation analysis of short fibre reinforced composites: Development and numerical aspects. *Composites Part B: Engineering*, 125:241 – 258, 2017.

[88] A. Dean. *Material Modeling of Short Fiber Reinforced Polymeric Composites: Theory, Numerical Aspects, and Application*. Doctoral degree, dissertation thesis, Leibniz Universität Hannover, 2017.

[89] A. Dean, N. Grbic, R. Rolfes, and A. Behrens. Macro-mechanical modeling and experimental validation of anisotropic, pressure- and temperature-dependent behavior of short fiber composites. *Composite Structures*, 211:630 – 643, 2019.

[90] M.J. Borden, T.J.R. Hughes, C.M. Landis, A. Anvari, and I.J. Lee. A phase-field formulation for fracture in ductile materials: Finite deformation balance law derivation, plastic degradation, and stress triaxiality effects. *Computer Methods in Applied Mechanics and Engineering*, 312:130 – 166, 2016.

[91] J. Fang, C. Wu, J. Li, Q. Liu, C. Wu, G. Sun, and Q. Li. Phase field fracture in elasto-plastic solids: Variational formulation for multi-surface plasticity and effects of plastic yield surfaces and hardening. *International Journal of Mechanical Sciences*, 156:382 – 396, 2019.

[92] J. Fang, C. Wu, T. Rabczuk, C. Wu, C. Ma, G. Sun, and Q. Li. Phase field fracture in elasto-plastic solids: Abaqus implementation and case studies. *Theoretical and Applied Fracture Mechanics*, 103:102252, 2019.

[93] E. Tanné, T. Li, B. Bourdin, J.J. Marigo, and C. Maurini. Crack nucleation in variational phase-field models of brittle fracture. *Journal of the Mechanics and Physics of Solids*, 110:80 – 99, 2018.

[94] A.J.M. Spencer. *Continuum Theory of the Mechanics of Fibre-Reinforced Composites*. Springer Science+Business Media, 1984.

[95] A. Dean, N. Safdar, and R. Rolfes. A co-rotational based anisotropic elasto-plastic model for geometrically non-linear analysis of fibre reinforced polymer composites: Formulation and finite element implementation. *Materials*, 12:1816, 2019.

[96] M. Vogler. *Anisotropic Material Models for Fiber Reinforced Polymers*. Doctoral degree, dissertation thesis, Leibniz Universität Hannover, 2015.

[97] M. Vogler, G. Ernst, and R. Rolfes. Invariant based transversely-isotropic material and failure model for fiber-reinforced polymers. *Computers, Materials and Continua*, 16:25 – 49, 2010.

[98] R. Rolfes, M. Vogler, S. Czichon, and G. Ernst. Exploiting the structural reserve of textile composite structures by progressive failure analysis using a new orthotropic failure criterion. *Computers & Structures*, 89:1214 – 1223, 2011.

[99] G. Ernst, M. Vogler, C. Hühne, and R. Rolfes. Multiscale progressive failure analysis of textile composites. *Composites Science and Technology*, 70:61 – 72, 2010.

[100] A. Dean and R. Rolfes. Fe modeling and simulation framework for the forming of hybrid metal-composites clinching joints. *Thin-Walled Structures*, 133:134 – 140, 2018.

[101] B. Lauke. Fracture toughness of short-fibre reinforced thermoplastics. *Composites Science and Technology*, 26:37 – 57, 1986.

[102] M. Ortiz and A. Pandolfi. Finite deformation irreversible cohesive elements for three-dimensional crack-propagation analysis. *International Journal for Numerical Methods in Engineering*, 44:1267–1282, 1999.

[103] A. Ortega, P. Maimí, E.V. González, and D. Trias. Characterization of the translaminar fracture cohesive law. *Composites Part A: Applied Science and Manufacturing*, 91:501 – 509, 2016.

[104] P.P. Camanho, C.G. Davila, and M.F. de Moura. Numerical simulation of mixed-mode progressive delamination in composite materials. *Journal of Composite Materials*, 37:1415 – 1438, 2003.

[105] L. Távara, J. Reinoso, A. Blázquez, and V. Mantič. On the 3D extension of failure models for adhesive joints under mixed-mode fracture conditions: LEBIM and CZM. *Theoretical and Applied Fracture Mechanics*, 100:362 – 376, 2019.

[106] P. Ladevèze and E. Le Dantec. Damage modelling of the elementary ply for laminated composites. *Composites Science and Technology*, 43:257 – 267, 1992.

[107] A. Quintanas-Corominas, P. Maimí, E. Casoni, A. Turon, J.A. Mayugo, G. Guillamet, and M. Vázquez. A 3D transversally isotropic constitutive model for advanced composites implemented in a high performance computing code. *European Journal of Mechanics - A/Solids*, 71:278 – 291, 2018.

[108] P. Maimí, P.P. Camanho, J.A. Mayugo, and A. Turon. Matrix cracking and delamination in laminated composites. Part I: Ply constitutive law, first ply failure and onset of delamination. *Mechanics of Materials*, 43:169 – 185, 2011.

[109] P. Maimí, P.P. Camanho, J.A. Mayugo, and C.G. Dávila. A continuum damage model for composite laminates: Part II – Computational implementation and validation. *Mechanics of Materials*, 39:909 – 919, 2007.

[110] F.P. Van der Meer and L.J. Sluys. Continuum models for the analysis of progressive failure in composite laminates. *Journal of Composite Materials*, 43:2131 – 2156, 2009.

[111] J. Reinoso, G. Catalanotti, A. Blázquez, P. Areias, P.P. Camanho, and F. París. A consistent anisotropic damage model for laminated fiber-reinforced composites using the 3d-version of the puck failure criterion. *International Journal of Solids and Structures*, pages 37 – 53, 2017.

[112] P. Farrell and C. Maurini. Linear and nonlinear solvers for variational phase-field models of brittle fracture. *International Journal for Numerical Methods in Engineering*, 109:648–667, 201.

[113] A. Mesgarnejad, B. Bourdin, and M.M. Khonsari. Validation simulations for the variational approach to fracture. *Computer Methods in Applied Mechanics and Engineering*, 290:420 – 437, 2015.

[114] R. Alessi, J.J. Marigo, C. Maurini, and S. Vidoli. Coupling damage and plasticity for a phase-field regularisation of brittle, cohesive and ductile fracture: One-dimensional examples. *International Journal of Mechanical Sciences*, 149:559 – 576, 2018.

[115] V. Carollo, J. Reinoso, and M. Paggi. A 3D finite strain model for intralayer and interlayer crack simulation coupling the phase field approach and cohesive zone model. *Composite Structures*, 182:636 – 651, 2017.

[116] J.D. Clayton and J. Knap. hase field modeling and simulation of coupled fracture and twinning in single crystals and polycrystals. *Computer Methods in Applied Mechanics and Engineering*, 312:447 – 467, 2016.

[117] A. Shahba and S. Ghosh. Coupled phase field finite element model for crack propagation in elastic polycrystalline microstructures. *International Journal of Fracture*, 219:31–64, 2019.

[118] A. Dean, N. Grbic, R. Rolfes, and B-A. Behrens. Macro-mechanical modeling and experimental validation of anisotropic, pressure- and temperature-dependent behavior of short fiber composites. *Composite Structures*, 211:630–643, 2019.

[119] O. Gültekin, H. Dal, and G.A. Holzapfel. A phase-field approach to model fracture of arterial walls: Theory and finite element analysis. *Computer Methods in Applied Mechanics and Engineering*, 312:542 – 566, 2016.

[120] J. Reinoso, A. Arteiro, M. Paggi, and P.P. Camanho. Strength prediction of notched thin ply laminates using finite fracture mechanics and the phase field approach. *Composites Science and Technology*, 150:205 – 216, 2017.

[121] R. Alessi and F. Freddi. Phase-field modelling of failure in hybrid laminates. *Composite Structures*, 181:9 – 25, 2017.

[122] M. Paggi, M. Corrado, and J. Reinoso. Fracture of solar-grade anisotropic polycrystalline silicon: A combined phase field–cohesive zone model approach. *Computer Methods in Applied Mechanics and Engineering*, 330:123 – 148, 2018.

[123] T. Guillen-Hernandez, I. García, J. Reinoso, and M. Paggi. A micromechanical analysis of inter-fiber failure in long reinforced composites based on the phase field approach of fracture combined with the cohesive zone model. *International Journal of Fracture*, 220:181–203, 2019.

[124] A. Puck and H. Schürmann. Failure analysis of frp laminates by means of physically based phenomenological models. *Composites Science and Technology*, 62:1633 – 1662, 2002.

[125] M. Eftekhari and A. Fatemi. Tensile behaviour of thermoplastic composites including temperature, moisture, and hygrothermal effects. *Polymer Testing*, 51:151–164, 2016.

[126] I.N. Vladimirov and S. Reese. Production simulation by means of a structure tensor based framework of anisotropic plasticity. *Proceedings in Applied Mathematics and Mechanics*, 12:823–826, 2012.

[127] P. Papadopoulos and J. Lu. On the formulation and numerical solution of problems in anisotropic finite plasticity. *Computer Methods in Applied Mechanics and Engineering*, 190:4889–4910, 2001.

[128] A. Dean, S. Sahraee, K. Ozenc, J. Reinoso, R. Rolfes, and M. Kaliske. A thermodynamically consistent framework to couple damage and plasticity microplane-based formulations for fracture modeling: development and algorithmic treatment. *International Journal of Fracture*, 203:115–134, 2016.

[129] W. Wagner and C. Balzani. Prediction of the postbuckling response of composite airframe panels including ply failure. *Engineering Fracture Mechanics*, 77:3648 – 3657, 2010.

[130] J-Y. Wu, T. Mandal, and V.P. Nguyen. A phase-field regularized cohesive zone model for hydrogen assisted cracking. *Computer Methods in Applied Mechanics and Engineering*, 358:112614, 2019.

[131] M. Deuschle and B.H. Kröplin. Finite element implementation of puck's failure theory for fibre-reinforced composites under three-dimensional stress. *Journal of Composite Materials*, 46:2485–2513, 2012.

[132] H. Schürmann. *Konstruieren Mit Faser-Kunststoff-Verbunden*. Springer Berlin Heidelberg, 2007.

[133] M. Mannigel. *Einfluss von Schubspannungen auf das Faserbruchgeschehen in kohlenstofffaserverstärkten Kunststoffen (CFK)*. Doctoral degree, dissertation thesis, Institut für Kunststoffverarbeitung (IKV), RWTH Aachen, 2007.

[134] M. Knops. *Analysis of Failure in Fiber Polymer Laminates*. Springer Berlin Heidelberg, 2008.

[135] M. Bishara, R. Rolfes, and O. Allix. Revealing complex aspects of compressive failure of polymer composites – part I: Fiber kinking at microscale. *Composite Structures*, 169:105–115, 2017.

[136] M. Bishara, M. Vogler, and R. Rolfes. Revealing complex aspects of compressive failure of polymer composites – part II: Failure interactions in multidirectional laminates and validation. *Composite Structures*, 169:116–128, 2017.

[137] A. Dean, J. Reinoso, N.K. Jha, E. Mahdi, and R. Rolfes. A phase field approach for ductile fracture of short fibre reinforced composites. *Theoretical and Applied Fracture Mechanics*, 106:102495, 2020.

[138] P.K. Kristensen and E. Martínez-Pañeda. Phase field fracture modelling using quasi-newton methods and a new adaptive step scheme. *Theoretical and Applied Fracture Mechanics*, page 102446, 2019.

[139] J-Y. Wu and Y. Huang. Comprehensive implementations of phase-field damage models in abaqus. *Theoretical and Applied Fracture Mechanics*, 106:102440, 2020.

[140] A.S. Kaddour and M. Hinton. Input data for test cases used in benchmarking triaxial failure theories of composites. *Journal of Composite Materials*, 46:2295–2312, 2012.

[141] C. Gerendt, A. Dean, T. Mahrhol, and R. Rolfes. On the progressive failure simulation and experimental validation of fiber metal laminate bolted joints. *Composite Structures*, 229:111368, 2019.

[142] P.P. Camanho, C.G. Dávila, S. Pinho, L. Iannucci, and P. Robinson. Prediction of in situ strengths and matrix cracking in composites under transverse tension and in-plane shear. *Composites Part A: Applied Science and Manufacturing*, 37:165–176, 2006.

[143] J. Reinoso, A. Blázquez, F. París, J. Cañas, and J.C. Meléndez. Postbuckling behaviour of a pressurized stiffened composite panel – part I: Experimental study. *Composite Structures*, 94:1533 – 1543, 2012.

[144] J. Reinoso, A. Blázquez, A. Estefani, F. París, and J. Cañas. A composite runout specimen subjected to tension–compression loading conditions: Experimental and global–local finite element analysis. *Composite Structures*, 101:274 – 289, 2013.

[145] J. Andersons and M. König. Dependence of fracture toughness of composite laminates on interface ply orientations and delamination growth direction. *Composites Science and Technology*, 64:2139 – 2152, 2004.

[146] P. Robinson and D.Q. Song. A modified dcb specimen for mode i testing of multidirectional laminates. *Journal of Composite Materials*, 26:1554–1577, 1992.

[147] D. Hull and Y.B. Shi. Damage mechanism characterization in composite damage tolerance investigations. *Composite Structures*, 23:99 – 120, 1993.

[148] R. Krueger, M.K. Cvitkovich, T.K. O'Brien, and P.J. Minguet. Testing and analysis of composite skin/stringer debonding under multi-axial loading. *Journal of Composite Materials*, 34:1263–1300, 2000.

[149] S.R. Hallett, B.G. Green, W.G. Jiang, and M.R. Wisnom. An experimental and numerical investigation into the damage mechanisms in notched composites. *Composites Part A: Applied Science and Manufacturing*, 40:613 – 624, 2009.

[150] A. Turon, P.P. Camanho, J. Costa, and J. Renart. Accurate simulation of delamination growth under mixed-mode loading using cohesive elements: Definition of interlaminar strengths and elastic stiffness. *Composite Structures*, 92:1857 – 1864, 2010.

[151] J.G. Ratcliffe, M.W. Czabaj, and T.K. Obrien. A test for characterizing delamination migration in carbon/epoxy tape laminates. 2012.

[152] M.F. Pernice, N.V. De Carvalho, J.G. Ratcliffe, and S.R. Hallett. Experimental study on delamination migration in composite laminates. *Composites Part A: Applied Science and Manufacturing*, 73:20–34, 2015.

[153] D. Purslow. Matrix fractography of fibre-reinforced epoxy composites. *Composites*, 17:289 – 303, 1986.

[154] E.S. Greenhalgh, C. Rogers, and P. Robinson. Fractographic observations on delamination growth and the subsequent migration through the laminate. *Composites Science and Technology*, 69:2345 – 2351, 2009.

[155] M.F. Pernice, J. Ratcliffe, N. De Carvalho, and S. Hallett. Investigating delamination migration in multidirectional tape laminates. 06 2014.

[156] M-Y. He and J.W. Hutchinson. Kinking of a crack out of an interface. *Journal of Applied Mechanics*, 56:270–278, 1989.

[157] L.F. Varandas, A. Arteiro, G. Catalanotti, and B.G. Falzon. Micromechanical analysis of interlaminar crack propagation between angled plies in mode I tests. *Composite Structures*, 220:827 – 841, 2019.

[158] C. Canturri, E.S. Greenhalgh, S.T. Pinho, and J. Ankersen. Delamination growth directionality and the subsequent migration processes – the key to damage tolerant design. *Composites Part A: Applied Science and Manufacturing*, 54:79 – 87, 2013.

[159] P. Maimí, P.P. Camanho, J.A. Mayugo, and C.G. Dávila. A continuum damage model for composite laminates: Part I - Constitutive model. *Mechanics of materials*, 39:897–908, 2007.

[160] M. Dittmann, F. Aldakheel, J. Schulte, P. Wriggers, and C. Hesch. Variational phase-field formulation of non-linear ductile fracture. *Computer Methods in Applied Mechanics and Engineering*, 342:71 – 94, 2018.

[161] C. Miehe, D. Kienle, F. Aldakheel, and S. Teichtmeister. Phase field modeling of fracture in porous plasticity: A variational gradient-extended eulerian framework for the macroscopic analysis of ductile failure. *Computer Methods in Applied Mechanics and Engineering*, 312:3 – 50, 2016.

[162] A. Dean, P. Kumar, J. Reinoso, C. Gerendt, M. Paggi, E. Mahdi, and R. Rolfes. A multi phase-field fracture model for long fibre reinforced composites based on the puck theory of failure. *Composite Structures*, -:112446, 2020.

[163] A. Quintanas-Corominas, A. Turon, J. Reinoso, E. Casoni, M. Paggi, and J.A. Mayugo. A phase field approach enhanced with a cohesive zone model for modeling delamination induced by matrix cracking. *Computer Methods in Applied Mechanics and Engineering*, 358:112618, 2020.

[164] A. Chambolle. An approximation result for special functions with bounded deformation. *Journal de Mathématiques Pures et Appliquées*, 83:929 – 954, 2004.

[165] L. Ambrosio and A. Braides. Energies in sbv and variational models in fracture mechanics, 1997.

[166] G. Catalanotti, J. Xavier, and P.P. Camanho. Measurement of the compressive crack resistance curve of composites using the size effect law. *Composites Part A: Applied Science and Manufacturing*, 56:300 – 307, 2014.

[167] A. Arteiro, G. Catalanotti, A.R. Melro, P. Linde, and P.P. Camanho. Micro-mechanical analysis of the effect of ply thickness on the transverse compressive strength of polymer composites. *Composites Part A: Applied Science and Manufacturing*, 79:127 – 137, 2015.

[168] G. Catalanotti and J. Xavier. Measurement of the mode II intralaminar fracture toughness and r-curve of polymer composites using a modified iosipescu specimen and the size effect law. *Engineering Fracture Mechanics*, 138:202 – 214, 2015.

[169] X. Li and J. Chen. A highly efficient prediction of delamination migration in laminated composites using the extended cohesive damage model. *Composite Structures*, 160:712–721, 2017.